Design and Implementation of Chipless RFID-Based Monitoring Sensor System for Coated Metallic Structures' Integrity

by

SAMEIR DEIF

A thesis submitted in partial fulfillment of the requirements for the degree of

Doctor of Philosophy

in

ELECTROMAGNETICS AND MICROWAVES

Department of Electrical and Computer Engineering
University of Alberta

Abstract

This thesis work presents structural health monitoring (SHM) techniques for coated-metallic structures based on Chipless Radio Frequency Identification (RFID) technology. The structures of interest for this study include pipelines for crude oil transportation and storage tanks (or terminals). The main features of the system are real-time monitoring, low cost, reliability, and the ability for mass-production.

First, an initial prototype sensor has a readout coil and an LC resonator on the passive tag with an interdigitated capacitor producing an entirely passive Chipless RFID system for pipeline integrity. Water ingress and coating delamination are reliably detected through monitoring the sensor's resonant frequency to achieve early corrosion prediction. The tag is built on a flexible substrate for wrapping around the pipe and representing the pipe coating. The sensor is conformal, battery-free, and low cost, which makes it suitable for pipeline monitoring in harsh environments.

Furthermore, a fully passive, wireless, Chipless RFID-based solution for out-of-sight pipeline monitoring is presented. The system is a combination of a tag ID, consisting of an array of seven rectangular spiral resonators (RSR), and a tag antenna composed of two cross-polarized patch-based antennas etched on a skin-thin microwave laminate. The proposed system exhibits the robust capability to create frequency signatures to detect and monitor defects underneath the pipeline coating owing to water ingress that could eventuate to corrode the pipeline. The reader antenna above the pipeline comprises of two identically cross-polarized log-periodic dipole antennas with the intent to remotely capture resonances of the tag ID in real-time for early detection and prediction of potential pipeline exposure to moisture.

Next, to cover large areas and achieve long arrays, identical resonators to build Chipless RFID is introduced. Backed with theory, extensive simulation, and experimental results, the innovative concept shows the ability to expand the sensors arrays considerably. It also achieves a real-time, inexpensive, and easy-to-install coating defect detection technique. A 120 cm prototype composed of 55 identical rectangular spiral resonators coupled to a transmission line is simulated, fabricated, and experimented. It is used to detect water ingress and coating delamination, which are the leading causes of corrosion initiation.

The need to protect the conductive sensor layer against the external environment requires the investigation of the effect of such a layer (overlay) on the sensor performance. Thus, an optimization process and study of different overlay materials and thicknesses to achieve the best performance are presented. It provides a reference source for the engineering and manufacturing process in regards to the trade-off between performance and cost for more economical applications of the sensor in the field.

Preface

This thesis is an original work by Sameir Deif.

The contents of Chapter 3 have been communicated as M. H. Zarifi, S. Deif, and M. Daneshmand, "Wireless passive RFID sensor for pipeline integrity monitoring," *Sensors Actuators, A Phys.*, vol. 261, pp. 24–29, 2017. Dr. Zarifi provided support in the concept formation, experimental setup, and manuscript edits.

Additionally, the contents of Chapter 4 have been communicated as S. Deif and M. Daneshmand, "Multi-Resonant Chipless RFID Array System for Coating Defect Detection and Corrosion Prediction," *IEEE Trans. Ind. Electron.*, 2019, doi: 10.1109/tie.2019.2949520, ©2019 IEEE and S. Deif, L. Harron, and M. Daneshmand; "Out-of-Sight Salt-Water Concentration Sensing Using Chipless- RFID for Pipeline Coating Integrity," in *2018 IEEE/MTT-S International Microwave Symposium - IMS*, Philadelphia, PA, USA, in June 2018. Mrs. Lorna Harron from Enbridge Inc. helped with her ideas and opinions during the course of this manuscript.

Finally, the contents of Chapter 5 have been communicated as S. Deif and M. Daneshmand, "Long Array of Microwave Sensors for Real-Time Coating Defect Detection," *IEEE Trans. Microw. Theory Tech.*, 2020, doi: 10.1109/tmtt.2020.2973385, ©2020 IEEE and S. Deif, B. Leier, M. Snow and M. Daneshmand; "Microwave Sensor Array for Corrosion Prediction in Steel Tank Bottoms," in *2018 12th International Pipeline Conference*, Calgary, Alberta, Canada, September 2018. My colleague Mr. Brent Leier helped me with literature section write up of the manuscript. Mr. Michael Snow from Enbridge Inc. helped with his ideas and opinions during the manuscript write up.

For all the above publications, I was responsible for the concept formation, theoretical analysis, fabrication, and characterization as well as the manuscript composition. Prof. Daneshmand was the supervisory author and was involved with concept formation and manuscript edits.

"Being an Electromagnetic Engineer: It Is Not a Job, It Is a Lifestyle"

- ***Mojgan Daneshmand 1976-2020***

To the memory of **MOJGAN DANESHMAND**

به یاد **مُژگان دانِشْمند**

To my parents, **Dawlat** & **Sameir**

إلى أبي وأمي، **دَولَتْ وسمير**

To **Nesma,** my amazing wife, my life's helpmate,
whose sacrificial care for me and our children
(**Renad** & **Roaa**)
made it possible for me to complete this work

إلى زوجتي العزيزة **نِسّمَه**

Acknowledgments

Praise is to Allah by Whose grace good deeds are completed.

First, I would like to extend my sincerest gratitude to my advisor Professor Mojgan Daneshmand. May she rest in peace! It was an unforgettable journey and too hard after you left (January 8th, 2020, at 06:12 AM (GMT+4:30) on the flight PS752). I won't forget what you did for me, your belief and confidence in my abilities, your full trust in me, and your tremendous support to my family and me along the journey. So, thank you, Mojgan, for everything. By the way, your IMS didn't gather this year!

I would also like to thank Professor Raafat Mansour, and Professor Marek Reformat for co-supervising my thesis during these difficult times. It was hard, and you made it as smooth as possible. Continued thanks to Professor Vien Van and Professor Sandipan Pramanik for serving on my committee and for taking the time to provide constructive criticisms to help improve this dissertation.

Completing this work would not have been possible without the financial support provided by the Canadian Research Chair Program, CMC Microsystems, and Enbridge Inc. with a special thanks to Lorna Harron for her belief in our work potential and Michael Snow for his continual constructive support and feedback. Their support is much appreciated.

A big thanks to my friends and colleagues including Dr. Jones, Dr. Zarifi, Brent, Dr. Olokede, Zahra, Sabreen, Mohammad A., Dr. Baghelani, Dr. Nosrati, Dr. Moghadas, Navid, Niloo, Morteza, Eric, Nazli, Amar and the rest of the team at M2M. Our days together will be missed and sorry if I fought with you before for keeping our lab tide. Special thanks to Dr. Iyer, Dr. Das, and Stuart for their

generous help along the way. Extended thanks to my friends Khaled, Dr. Balbola, Dr. Mohy, Dr. Darwish for their friendship and support in tough times.

Thanks to my mother, the most important and appreciable person in my life, and my father for his silent love and care. My brother Mohammad, I can't forget what you did for me from my first days till today, and I owe you my life. Lastly, but most importantly, I would like to thank my amazing wife, Nesma, for her endless love and support. Being in my life is the cause of this work existence. It was a tough and challenging pathway, but your patience and commitment to our small family made it possible.

Table of Contents

List of Tables

List of Figures

Abbreviations & Acronyms

AC Alternating Current.

BW BandWidth.

CIPS Close Interval Potential Survey.

CP Cathodic Protection.

EM ElectroMagnetic.

FBE Fusion-Bonded Epoxy.

HFSS High Frequency Structural Simulator.

IDC Interdigitated Capacitor.

IIoT Industrial Internet of Things.

IoT Internet of Things.

ISM Industrial, Scientific and Medical.

LPDA Log-Periodic Dipole Antenna.

MFL Magnetic Flux Leakage.

MI Magnetic Induction.

NDE Nondestructive Health Evaluation.

PCB Printed Circuit Board.

PTFE Polytetrafluoroethylene.

RCS Radar Cross-Section.

RFID Radio Frequency Identification.

RSR Rectangular Spiral Resonators (RSR).

RSRR Rectangular Spiral Ring Resonators.

SHM Structural Health Monitoring.

SLPM Standard Litre per Minute.

SRR Spiral Ring Resonator.

SWCNT Single-Wall Carbon Nanotubes.

TEM Transverse ElectroMagnetic.

TPM Tapered Microstrip Line.

WSNs Wireless Sensor Networks.

Chapter 1

Introduction

1.1 Motivation

The advancement of structural health monitoring (SHM) techniques has gained attention over the conventional non-destructive health evaluation (NDE) methods to diagnose the state of structure health during its lifetime. The former provides continuous and real-time information about the integrity of in-service structures and facilities such as buildings, bridges, pipelines, etc. However, more efforts and innovative-/proactive-approaches are needed to convey the fast-growing industrial internet of things (IIoT). If the facility's integrity, such as pipelines, could be predicted and repaired promptly, its integrity could be fully sustained. Besides, proactive employment of in-situ/on-site SHM techniques to displace the scheduled-driven maintenance with conditional or on-demand could reduce the preservation cost and improve system integrity.

While the developed approach in this thesis work applies to almost any coated-metallic structures, the scope was focused on major oil and gas facilities such as pipelines and crude oil storage tanks – also called terminals – as targeted applications. Pipeline systems are considered one of the most common significant infrastructures and indispensable elements for national energy security. Therefore, it is a matter of national concern to have a safe and defect-free operation of pipeline systems [1]. This concern draws different attention views from academia, industry, and

government-wide due to its accidents' catastrophic consequences that may include fatalities. Hence, interdisciplinary work to engineering designs using fundamental and applied research outcomes as safety insurance is required. This introduced the notion core concept of integrity in pipeline systems. The most significant defect, percentage-wise, for pipeline systems is the wall surface defects due to corrosion damage [2]. Pipelines and terminals are made from carbon steel, which has 85% of all manufactured steel. Since carbon steel is thermodynamically unstable, it is susceptible to natural oxidation and galvanic corrosion [3, 4]. In practice, the remaining life assessment of pipeline is based on two deterministic failure criteria: "leak" and "rupture," and the shortest remaining lifetime is selected. Leak critical state is reached when the defect under corrosion is of depth ranges between 60% to 80% (per the code used) of the pipe wall thickness.

Embedding sensor systems during the manufacturing of structures of interest would increase its reliability and safety to the public and environmental health benefits while decreasing the structure's life-cycle cost. In the oil and gas industry, for instance, crude oil pipelines and terminals are playing a critical rule for transmitting and storing processes, respectively. Oil companies take several precautions such as pre-service integrity testing, cathodic protection (CP), and/or anti-corrosive coatings to protect these facilities against potential damage due to environmental impacts. These methods can delay the inevitable corrosion processes of the facility structure (steel for pipelines and terminals); however, it's impossible to prevent it. Current corrosion detection techniques are designed to detect flaws such as geometric deformation metal loss, thickness change, and/or cracking [5]. Magnetic flux leakage (MFL) [6], close interval potential survey (CIPS) [7], Pearson survey [8], etc., are examples of current such methods.

Recently, radio frequency (RF)- and microwave-based techniques have demonstrated viability for SHM and corrosion detection. Several experiments were conducted using wireless sensor networks distributed through the pipe [9–11], microwave

techniques [12–16], and Radio-Frequency Identification RFID-based monitoring systems [17–23]. These techniques attempt to tackle corrosion after its occurrence, while corrosion prediction would be of greater interest. Among these different sensing technologies and methods, chipless radio frequency identification (RFID) with no-chip tag has demonstrated a strong potential to operate in harsh, inaccessible and noisy environments with near-zero electric power [24–26]. In contrast to conventional sensing methods which involve wired or locally powered sensors, chipless RFID provides completely battery-free, inexpensive, and wireless solution with real-time response for vast variety of applications including displacement and corrosion detection [27, 28].

1.2 Objectives

The primary objective of this thesis is to develop a fully integrated chipless RFID-based monitoring system to be embedded in pipeline and oil tank structural coatings to predict potential defects, improving the integrity and overall lifetime of pipeline transport systems. To achieve this goal, a wireless, printable, and a chipless resonance-based array of sensors integrated with planar patch-based tag antennas are proposed. While the proposed system is applicable for any coated-metallic structure, pipelines and crude-oil storage tanks are then investigated.

The objectives of this thesis can be summarized as the following: (1) combine the benefits of multi-resonant chipless RFID array concept and a low-profile patch-based antennas into a single flexible chipless RFID system for coating defect detection (such as air breach, water ingress, and coating deterioration) and corrosion prediction focused on pipelines; (2) the capability for out-of-sight detection; (3) developing a concept for full area coverage using longer arrays of the chipless RFID sensors with simple design structure for mass-production focused on crude oil storage tanks; (4) study the effect of the overlay as a protection layer for the chipless RFID array sensor systems. The developed system design of this thesis has the potential for immediate application in the targeted industries such as manufacturing lines of pipelines,

crude-oil storage tanks and terminals, bridges, airplanes, etc. The work of this thesis will open unlimited applications to protect any coated-metallic structure against the hidden causes of failure such as corrosion.

1.3 Outline

The thesis is structured into seven main chapters as follows:

In Chapter 1, the motivation and the research objectives of the thesis are introduced.

Chapter 2 discusses a literature survey on the topics related to the thesis. These topics begin with the pipeline integrity solutions that are currently developed and applied in the field. It is followed by the undeveloped techniques which still under research and investigation. Finally, review of the RF/Microwave based techniques for pipeline integrity monitoring is also presented, then a focus on the chip/chipless RFID methods is followed.

In Chapter 3, an initial proof-of-concept for using chipless RFID-based sensors for pipeline integrity monitoring for real-time applications is presented. The tag consists of LC circuits of a coil and planar interdigitated capacitor (IDC) in addition to a readout coil. Two coating defects are monitored, coating lift-off and water ingress. The resonant frequency of the sensor demonstrates a strong relation to these defects with reliable and repeatable behavior.

Chapter 4 introduces a more complex and comprehensive chipless RFID sensor system design for coating monitoring. An array of rectangular spiral resonators combined with a slotted-patch antenna represent the sensor tag. Two of a well-know cross-polarized log-periodic dipole antennas (LPDA) are used for reading purposes. The system is an entirely passive, printable, low-cost, and wireless solution for out-of-sight pipeline monitoring. The reader circuitry is remotely capturing resonances of the tag ID in real-time for early detection and prediction of potential pipeline exposure to moisture, which represents the primary stimulus for the corrosion process.

In Chapter 5, the sensor array extended the real-time monitoring technique to cover large coated-metallic structures. Unlike the array elements in Chapter 4, 55 identical rectangular spiral resonators coupled to a 120 cm long transmission line are simulated, fabricated, and measured during the experiment. The system is developed for water ingress and coating delamination detection in real-time. The simplicity of the concept and it's easy-to-apply magnified the reliability and applicability of the system.

In Chapter 6 and to protect the sensor system developed in the previous chapters, an overlay layer and its effect on the system performance is introduced. The study provides the recommended and optimized materials' properties to be used as an overlay from thickness to the dielectric permittivity. Measured results backed with simulation proof-of-concept results exhibit the validation of the proposed overlay properties to severely minimize the effect of the external environment on such sensors.

Finally, in Chapter 7, a summary of the significant results from the thesis work and an outline of the future work is introduced, including the wireless communication range enhancement, resolution improvement, system scalability, and manufacturing.

Chapter 2

Background

This chapter presents a literature survey on the topics related to the thesis. Section 2.1 provides an introduction to the coating manufacturing and standards controlling this process. It also presents the standard tests conducted for the integrity check of a new or existing coating to be applied in the field. Next, in Section 2.2 and Section 2.3, a summary of the current developed and undeveloped solutions used in pipeline integrity are presented. Specifically, the RF- and Microwave-based solutions are introduced in detail Section 2.3 as a work in progress in such field. Finally, Section 2.4 focuses on state-of-the-art applications in chipless RFID technology as the potential and promising solution for our application.

2.1 Coating Manufacturing and Standard Tests

Many standards govern coating performance through different tests and experiments before field applications. American Society for Testing and Materials (ASTM) and Canadian Standards Association (CSA) maintain and update such standards which pipeline industry must follow to estimate their pipeline lifespan [29]. For example, the coating resistance of the cathodic protection (CP) application is defined in ASTM G95-07 and CSA Z245.20/21. Figure 2.1 shows one of the main tests for pipeline coatings quality control; cathodic disbondement (CD) test [30]. The CD test is to ensure low delamination and surface pretreatment quality for the coating

with the CP applied in the soil. Numerous parameters such as voltage, temperature, electrolyte components play an important role in the test results [30]. The coating in Figure 2.1(b) shows a good resistance for delamination (radial disbondement for Fusion Bonded Epoxy (FBE) is typically 3-4 mm [31]).

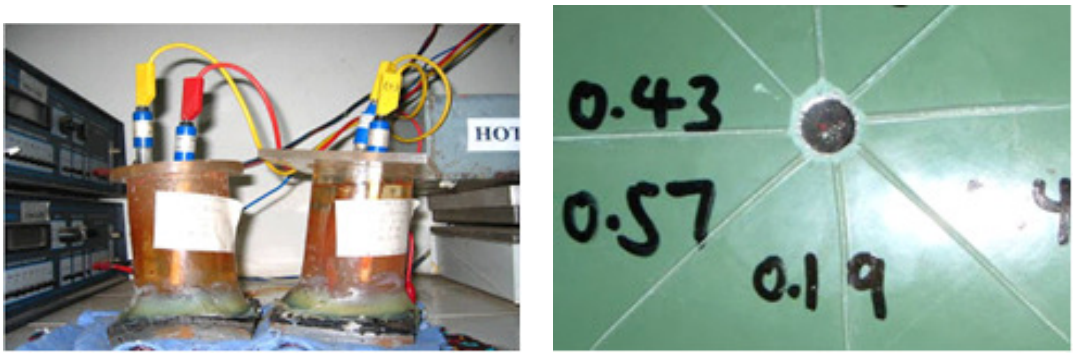

(a) (b)

Figure 2.1: Laboratory CD test in a), and b) Cathodic disbondement sample [31].

The alkalinity initiates cathodic disbondement for coatings at the boundary layer between the coating and the soil. The CP current creates alkalinity at this interface, which increases the pH level at the boundary of coating and carbon steel for the pipeline structure. Figure 2.2 shows the coating disbondement under CP currents.

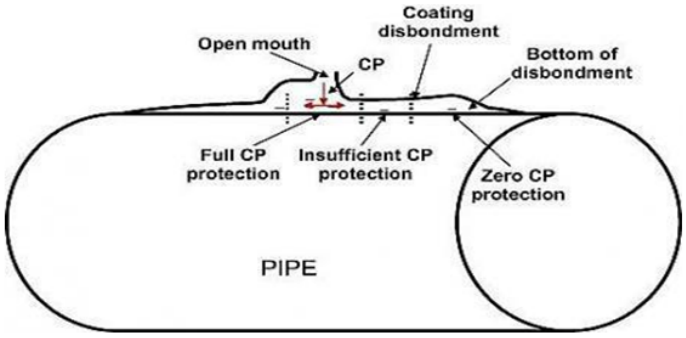

Figure 2.2: Disbondement of polyethylene-coated in buried pipelines with CP applied [32]

Once the coating disbondement instated, an electrolyte such as water will ingress below the coating and initiates *corrosion*, which is the primary source of concern that

could result in a pipe defect and possible oil spills [2, 33].

2.2 Currently Developed Pipeline Integrity Solutions

Figure 2.3 summarizes the available methods and techniques for pipeline integrity monitoring and inspection procedures [34–36]. Unlike inspection, which aims to assess the pipeline fitting for operation, the monitoring process intentions to identify or detect if the defect is taking place at the current moment. Once it runs, the inspection can inform about the expected lifetime of the pipeline or if it needs a shutdown for repairing or replacing. At the same time, monitoring can answer these questions in a reasonable time.

The inspection method will depend on the pipeline environment if it is piggable or not. Potential survey techniques and in-line-inspection (ILI) methods are the candidates when the system is piggable. On the other hand, long-distance techniques such as guided wave ultrasonic, and hydrostatic tests are types of practices for non-piggable pipes. Inspection tools give accurate information to a certain limit about the current state of the pipeline system; however, its application frequency is low due to the substantial cost associated with its usage as well as the human resources and special equipment required [35]. Because of this, to have a real-time alert system, a monitoring solution that can be distributed across the targeted monitored infrastructure is in need.

Two categories of monitoring solutions exist: non-electrochemical and electrochemical, as shown in Figure 2.3. Generally, special probes or an array of probes are distributed within a pipeline system vicinity in order to simulate the pipeline surface conditions and estimate the rate and pattern of the corrosion. Electrochemical methods can directly measure the corrosion rate; however, its use is limited when cathodic protection (CP) is applied. On the other hand, the non-electrochemical method measures the corrosion rate indirectly by comparing metal losses or sensing the physical

Figure 2.3: Comprehensive Developed Pipeline Integrity Solutions.

properties of the surrounded environment.

All methods described above can offer valuable data about corrosion, such as its level of severity and rate of occurrence. However, none of these methods can inform about the coating conditions such as disbondement or lift-off, especially at its initial stages. The ability to gather such information could lead to an efficient maintenance plan and prevent any possible spills or accidents before it happens. Though, we see a successful candidate in the promising chipless RFID technology to tackle such a situation with an accuracy that achieves the pipeline integrity goal at a reasonable and affordable cost on the other hand.

2.3 Undeveloped Pipeline Monitoring Techniques

Recent literature shows the potential of technologies such as optical fiber [37–39], wire-based [40], and RF-/Microwave-based devices to be introduced for monitoring pipeline systems. Our focus in literature will be on the RF- and Microwave-based technologies used up-to-date to investigate the ability of such methods in pipeline monitoring [10, 12, 13, 17–21, 23, 41]. A radar detection leakage method in natural gas pipelines was developed in [12]. It measures the radar cross-section (RCS) backscattered from methane leaked plume index-of-refraction inhomogeneities in the air. As the methane-air mixture changes, the index-of-refraction static and dynamic changes were observed to estimate the radar cross-section of the gas plume. The method is highly affected by weather and water content in the air. In [41], *Qing et al.* introduced a real-time active pipeline integrity detection (RAPID) system for assessing new and existing pipeline systems. The system principle is based on sending a modulated sine wave signal around the pipe structure using a belt (SMART layer in Figure 2.4). The method developed to locate and estimate the corrosion size and depth and was able to detect depth as low as 0.125 mm in a 7.14 mm wall-thickness pipe.

An RFID-based approach for pipeline monitoring was introduced in [20] to use the pipe as a communication channel between the interrogator and distributed RFIDs

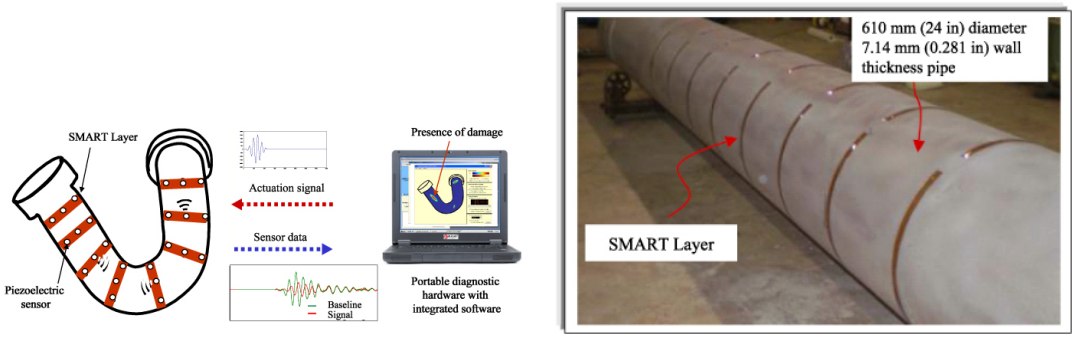

(a) (b)

Figure 2.4: Installed sensor array mounted on a pipe [41]

along the pipe, as shown in Figure 2.5. Any change in tag impedance (inductance and capacitance) will change the load impedance seen by the interrogator, and hence can be monitored. This concept is called the backscatter modulation, which tracks the reflected impedance change. It requires ground the tag sensors in addition to alternating current (AC) signal interrogated to the pipe, which is not the desired approach for pipeline systems. Magnetic induction (MI)-based wireless sensor networks (WSNs) were used for monitoring underground pipelines in [10]. The system configuration is shown in Figure 2.6, and it consists of two main layers: 1) hub layer for communication purposes, 2) in-soil sensor layer for sensing purposes. Sensors can be inside (ex: acoustic devices) and outside (ex: soil properties' sensors) the pipe and have MI transceiver to communicate with the hub. The MI transceivers embedded within the sensor array use the MI waveguide technique to send their data to a central unit for data post-processing.

Jones et al. in [42] introduces a different approach to utilize the pipeline structure as a communication channel to measure the corrosion under insulation. The method argued that the insulated pipe structure could be used as a coaxial waveguide to preserve EM wave propagation. The presence of water under insulation was the primary detection purpose of the suggested work as a significant pipeline risk and potential corrosion incubator. A pure and non-dispersive TEM mode was excited through the pipe using circumferentially distributed antenna array, as shown in Figure

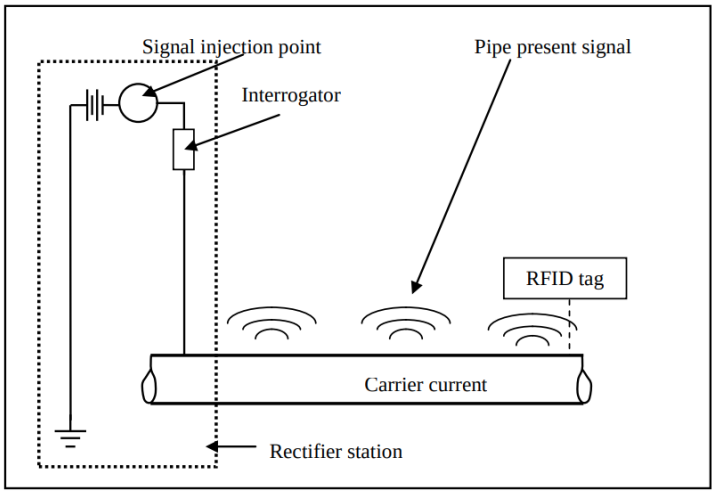

Figure 2.5: An Interrogation current was used to communicate with the RFID tags [20]

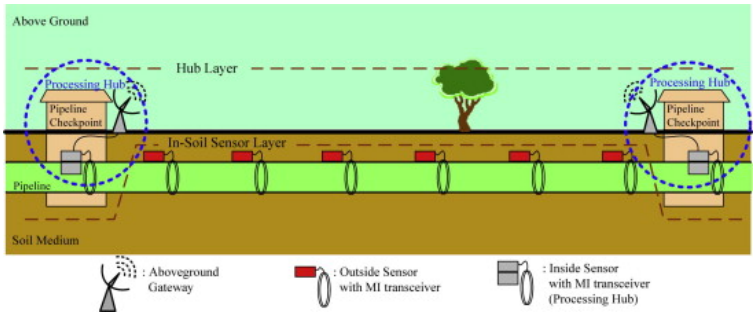

Figure 2.6: System configuration for a magnetic induction-based system for underground pipes [10]

2.7. Such work introduces a massive perturbation and intrusive way of dealing with the pipeline.

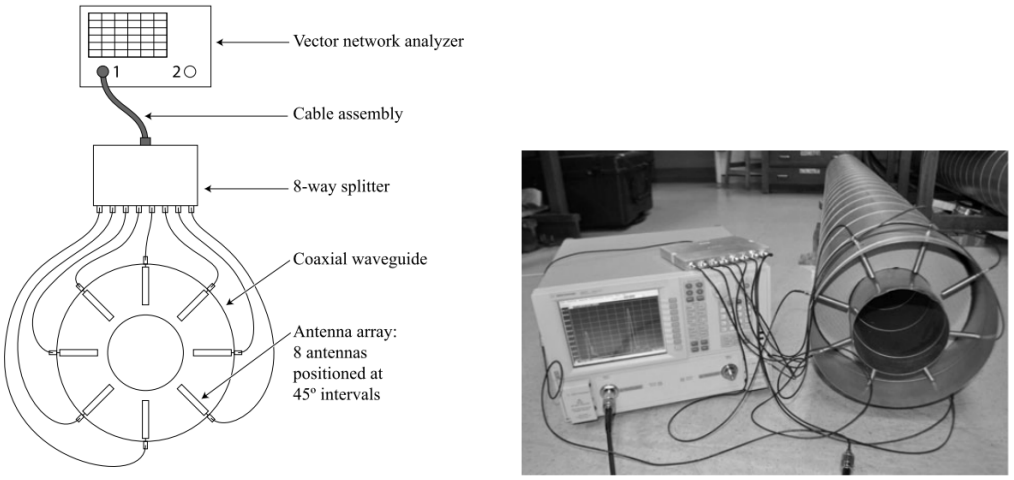

(a) (b)

Figure 2.7: The prototype for corrosion under insulation detection system [13].

RFID technology has gained great attention in pipeline field specifically for corrosion detection [17–19, 21, 23]. *Alamin et al.* have shown the ability of conventional RFID tags to distinguish between samples with different corrosion levels [18]. As shown in Figure 2.8, a reader coil is used as an interrogator for the RFID tag and read the backscatter signal. The tag was placed on top of coated and uncoated mild steel samples exposed to the atmospheric corrosion for different exposure time (1, 3, and 6 months). At 45 mm between the tag and the reader coil (read range), the system could differentiate between each sample with a corresponding amplitude, as shown in Figure 2.8(b).

Another method using RFID to estimate the corrosivity level on metals is conducted by *He et al.* in [21]. Using ready-made RFID tags and cover them with corroded steel foil (25, 50, 150, 200, and 300 um thicknesses) and measure the signal received from these tags. At first, the uncorroded foil completely blocks the signal from the tags to the interrogator, Figure 2.9. After the corrosion affects the foil sheets, the reader start receives a signal from the RFID tags, as shown in Figure 2.9(b).

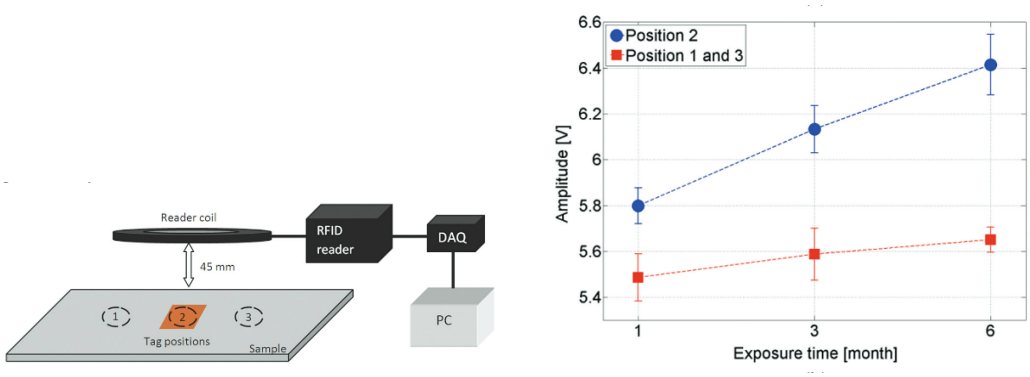

(a) (b)

Figure 2.8: RFID-based corrosion monitoring system shows its main components in (a), and amplitude response of the measured positions shown in (b) [18].

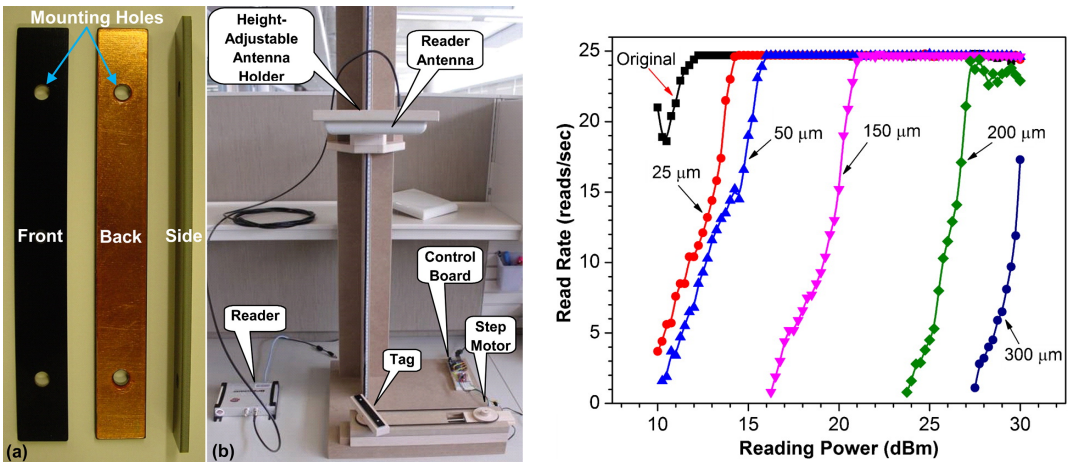

(a) (b)

Figure 2.9: RFID-based corrosion system: a) tag and reader platform, b) tag response to the interrogator vs reading power for different sheet thicknesses [21].

A passive UHF RFID tag was developed by *Hong et al.* as an on/off state indicator for corrosion monitoring for pipelines [19], Figure 2.10. It has the same idea of having a corroded element (exposed metal parts in Figure 2.10(b)), which connects between a chip-based sensor and two antennas.

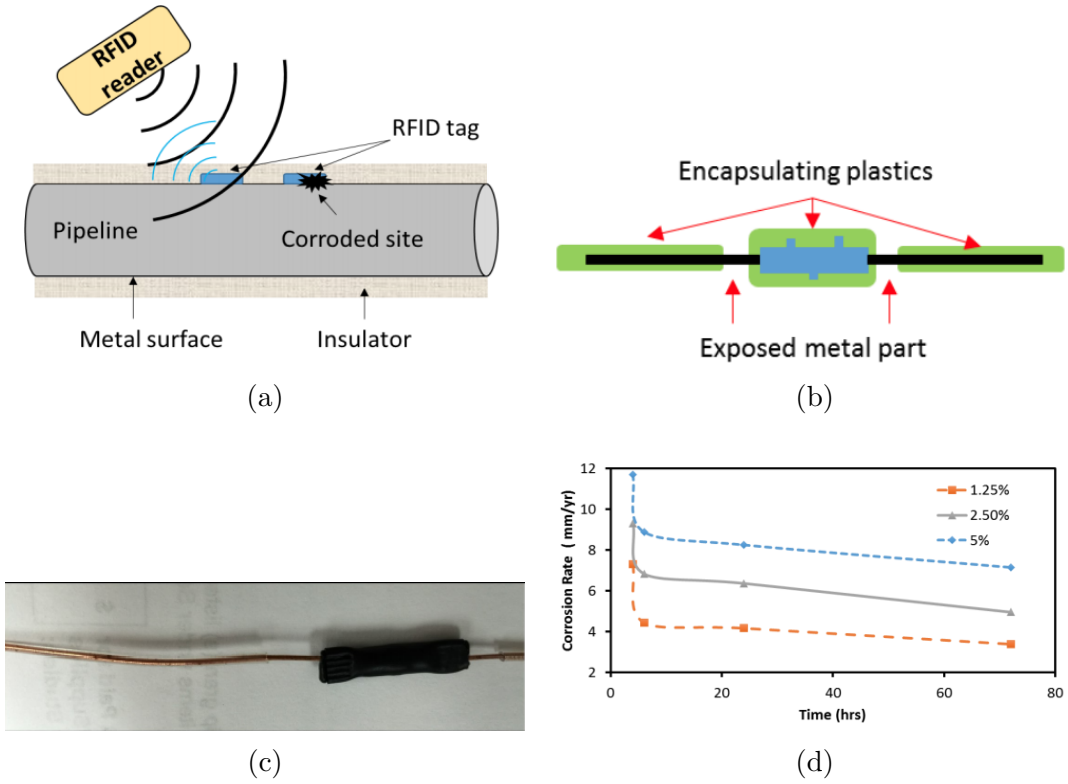

Figure 2.10: RFID-based corrosion system: a) The system designed mounted on pipeline b) the tag components, c) strips corroded according to their thicknesses [17], and d) variation of corrosion rate with time at different concentrations of acidic soils.

Lawand et al. have proposed a corrosion indication system based on metallic strips made from the same pipeline materials to corrode at the same rate [17]. The sensor circuit has a transponder coil to energize an indicator LED connected through the strips, as shown in Figure 2.11. Once the strips are fully corroded, it breaks the circuit to inform that total corrosion had happened in that location.

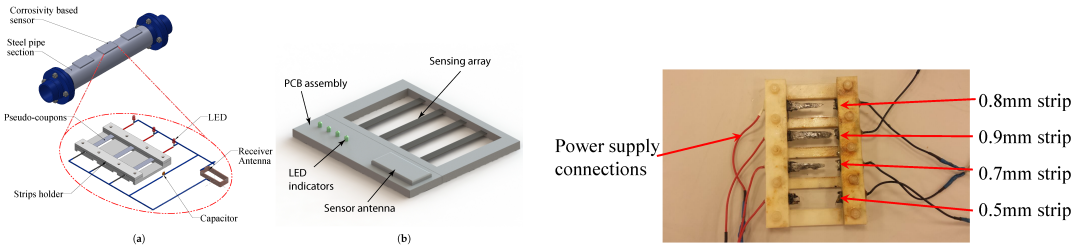

(a) (b)

Figure 2.11: RFID-based corrosion system: a) The system designed mounted on pipeline b) strips corroded according to their thicknesses [17].

2.4 Chipless RFID Technology

Chipless RFID is a traditional RFID with the IC chip device eliminated and hence, it becomes more popular and attractive research topic in the recent years [43]. Figure 2.12 shows a generic RFID system with its main components in addition to the difference between a chip and chipless RFID tags. Chipless RFID ability to use inkjet-printing technology to stamp the tags on numerous flexible surfaces extending from textile, metal, plastic, to paper with oxidation immunity, put it as a potential substitute to barcode and conventional chipped-RFIDs [44–51]. Presently, chipless RFID technology shows the ability for use in temperature [52–54], humidity- [55], [56], and light-sensing [57], as well as tracking [58], [59] and evacuation [60] purposes. In addition, the chipless RFID extends its existence for Nano-applications such as gas sensing [61–63], strain sensing [64], [65], as well as humidity sensing [66, 67] for Nano-scale applications.

Chipless RFID sensor composed of multi-spirals resonators coupled to a transmission line was used for temperature sensing by *Amin and Karmakar* in [52]. Stanyl TE200F6 polyamide, which has a linear variation of its dielectric constant with the temperature, was embedded in the spiral structure, which served as the sensitive element of the sensor. The sensor with the lowest frequency was modified for the sensing, and another two resonators represent the tag ID, Figure 2.13. Another example of a chipless RFID temperature sensor by *Vena et al.* using dual-polarized spiral ring

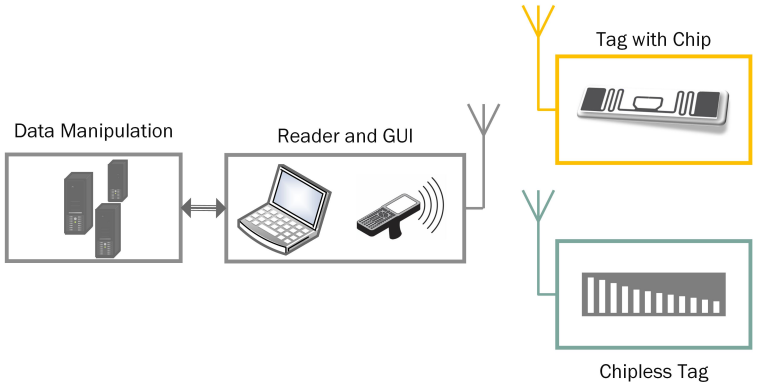

Figure 2.12: RFID system shows the difference between chip and chipless Tags.

resonator (SRR); one used for coding (V) and the other one used for sensing (H), as shown in Figure 2.14 [53]. The sensor used for CO_2 detection in addition to the temperature. Silver ink was used for the SRR conductive structure, and single-wall carbon nanotubes (SWCNTs) were used for printing the sensitive part of the sensor. The sensor shows the ability to detect CO_2 concentration and also the temperature only by deposit a new coating layer to prevent the CO_2 effect.

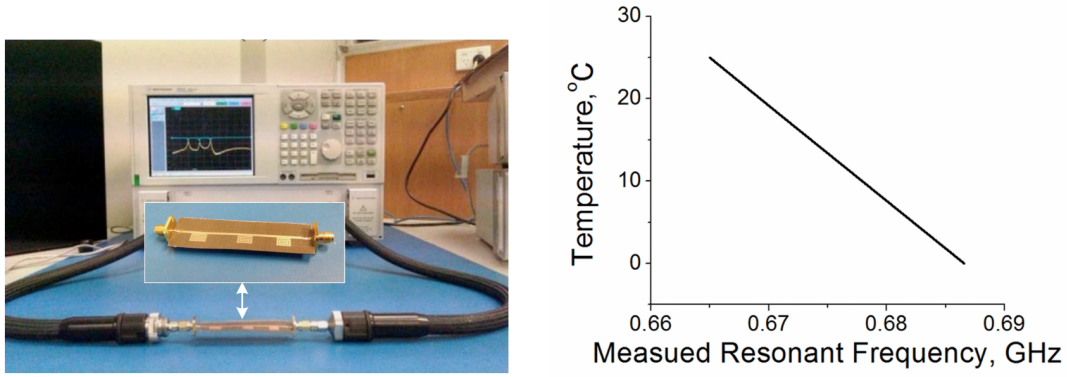

(a) Dual-polarized SRRs printed using different inks.

(b) The sensor under test in the test chamber.

Figure 2.13: Chipless RFID for Temperatures Sensor [52]

The chipless RFID also employed in humidity sensing applications using a dual planar LC resonator (IDC) inkjet-printed on a paper substrate [55]. With one resonator used for sensing and another one for the ID encoding, the paper substrate utilized as the sensing material. The system provides relative humidity range from 20-70%,

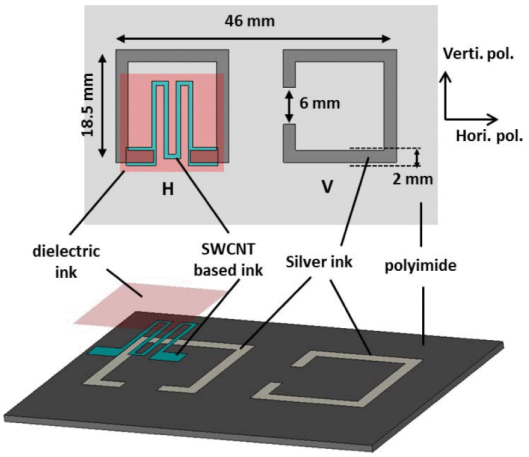

(a) Dual-polarized SRRs printed using different inks.

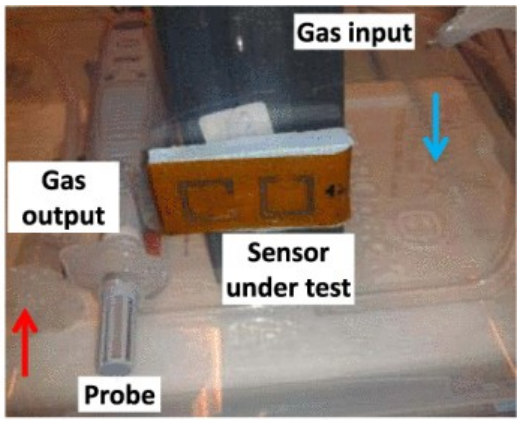

(b) The sensor under test in the test chamber.

Figure 2.14: Chipless RFID for Gas Sensing [53].

as shown in Figure 2.15. *Habib et al.* introduced 8-bit paper-based chipless RFID for humidity sensing using L- and I-shaped dipole structure inkjet printed with silver ink as shown in Figure 2.16 [56]. By introducing different lengths for each dipole, the frequency signature was created and measured using the Radar Cross-Section (RCS) method. Results showed the capability of the printable sensor for humidity sensing, as exhibited in Figure 2.16.

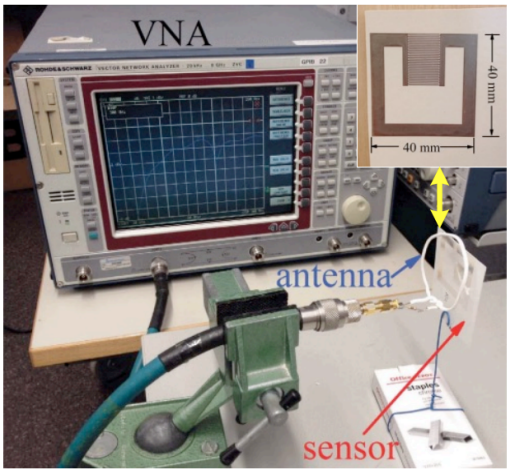

(a) Measurement setup for the sensor and the reading antenna.

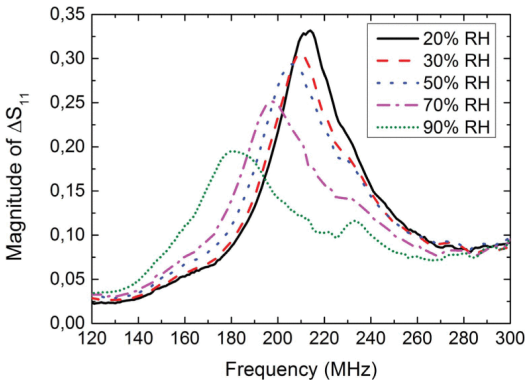

(b) Measured $\triangle S11$ vs relative humidity (RH) levels at 25 ^{o}C.

Figure 2.15: Chipless RFID for Humidity Sensing [55].

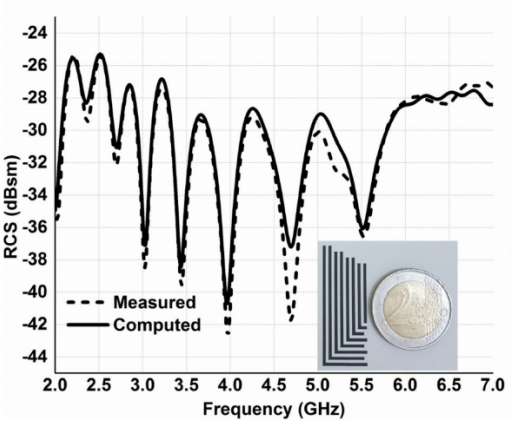

(a) Radar Cross-Section response for the tag structure.

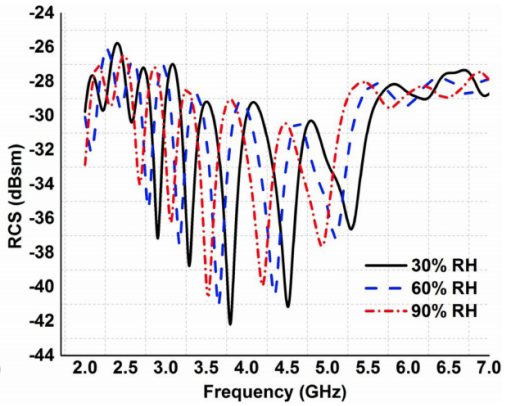

(b) Measured RCS vs frequency for different relative humidity (RH) levels.

Figure 2.16: Chipless RFID for Humidity Sensing [56].

One of the promising fields for chipless RFID is the replacement of standard barcode in item tracking [58], [59]. An entirely passive chipless RFID system was introduced by *Preradovic et al.* for item tracking with a significant difference from previous work to encode the data in both signal amplitude and phase [58]. UWB monopole antennas were used as the tag antennas, and Log Periodic Dipole Antenna (LPDA) was used for the data reading; both are cross-polarized for minimum cross-talk as shown in Figure 2.17. A successful 6-bit and 35-bit chipless RIFD tags were fabricated and tested.

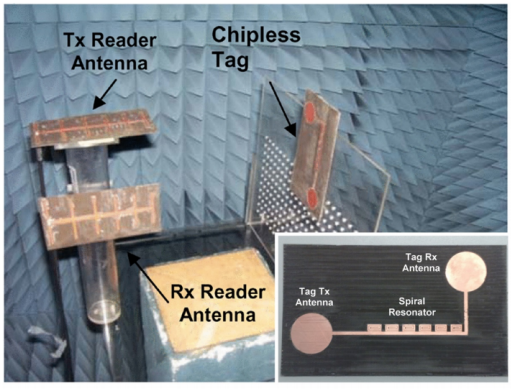

(a) Prototype measurement setup with the 6-bit chipless RFID tag as an inset.

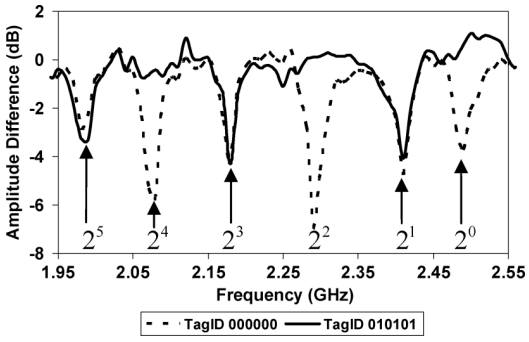

(b) Received tag signal at the reader end from distance 5 cm.

Figure 2.17: Chipless RFID Tracking Sensor [58].

Further, a time-domain tracking sensor based on chipless RFID was proposed by *Shao et al.* with 8-bit ID generating circuit shown in Figure 2.18(a) [59]. Silver ink was used in the tag printing process on HP photo paper. The capacitors were created using tapered Microstrip line (TPM), as shown. Moreover, Figure 2.18(b) shows a chipless RFID photosensitive sensor based on commercially LC anti-theft tag composed of a coil (for communication) and IDC capacitor covered by photopolymer layer (for sensing) [57].

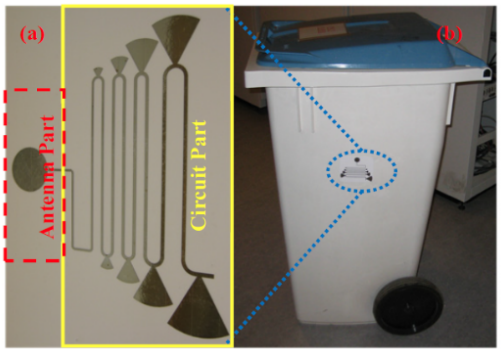

(a) Chipless RFID Tracking Sensor (Time Domain-Based) [59].

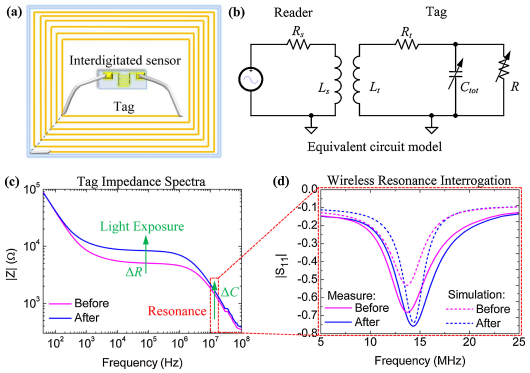

(b) Chipless RFID Light Sensor [57].

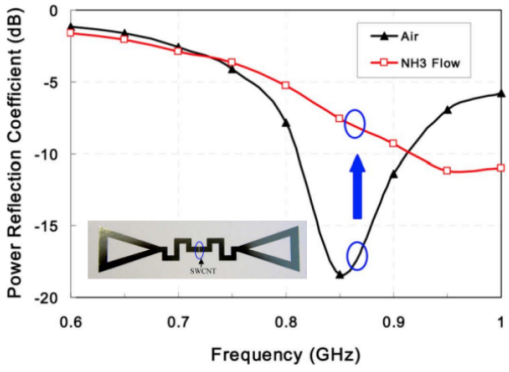

(c) Chipless RFID Nano-Based Gas Sensor [61].

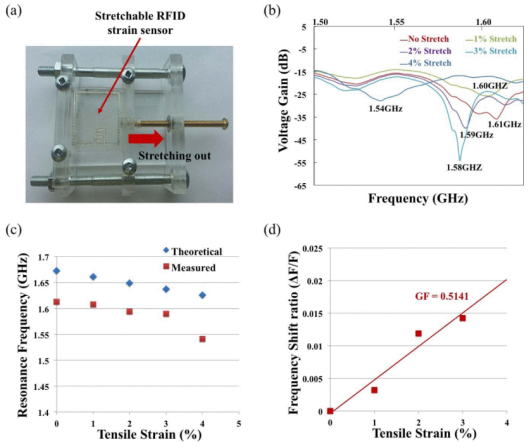

(d) Chipless RFID Nano-Based Strain Sensor [65]

Figure 2.18: Various applications of chipless RFID.

On the other hand, a Nano-based chipless RFID gas (NH_3) sensor with SWCNT as the sensitive part and bow-tie antenna as the communication mean as shown in Figure 2.18(c). Lastly, a Nano-based strain sensor using the chipless RFID technique

printed with silver ink is introduced by *Kim et al.* shown in Figure 2.18(d) [65]. The sensor consists of two LC circuits (inductor turn and IDC) stamped on PET substrates. The results show the robustness of the strain sensing using the proposed techniques, as shown in Figure 2.18d.

2.5 Summary

Although there is significant attention to finding a viable solution for monitoring pipeline integrity, most methods target the detection of corrosion, which occurs at the later stage in the process of defect generation. The existence of oxygen and water in the proximity of carbon steel is the main cause of stimulating corrosion [68–70]. Because removing oxygen from groundwater is not a practical method for corrosion control, we propose to *predict* corrosion by monitoring coating deterioration and possible water ingress that is eventually responsible for corrosion-related incidents.

Chapter 3

Wireless Passive RFID Sensor for Pipeline Integrity Monitoring

The primary objective of this thesis is to develop a fully integrated chipless RFID-based monitoring system to be embedded in pipeline and oil tank structural coatings to predict potential defects. In this chapter, a proof-of-concept experiment is conducted using a battery-free LC-based sensor for pipeline integrity monitoring in a real-time fashion. The sensor monitors water ingress and coating lift-off from the pipeline, which is the initial step in the external corrosion of a metal pipe.

The system utilizes a passive sensor tag on a pipe, which wirelessly communicates with an external readout device. Figure 3.1 demonstrates the system in one of its prototyping. Breaching of the polymer coating results in distance variation between the coating and metal pipe and consequently affects the interdigitated capacitor on the tag. The capacitor variation is wirelessly transferred to a reader coil and its effect is reflected in return loss parameter (S_{11}). It is shown that air or water penetration underneath the coating can be detected by the use of the proposed sensor.

The organization of the chapter is as follows. Section 3.1 presents a theoretical operation of the proposed sensor including a full-wave simulation of an LC-based chipless RFID sensor and generation of the lumped element circuit model, and emulation of the pipeline defects such as lift-off or water ingress. Measured results and discussion of the sensor performance are provided in Section 3.2. The important conclusions of

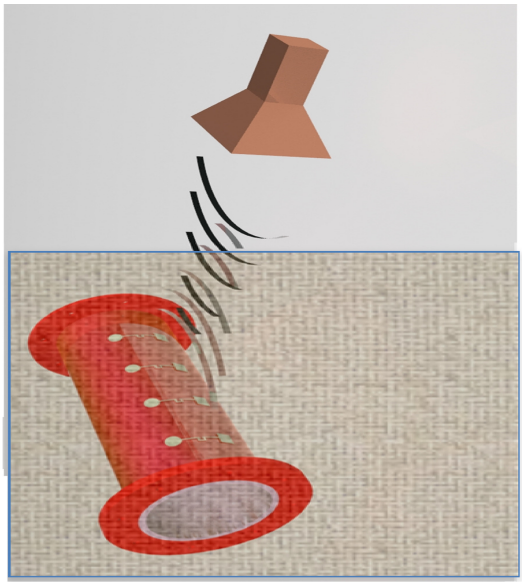

Figure 3.1: The proposed sensor patched (stamped) on a pipeline and scanned using reader coil (or antenna).

the chapter are give in Section 3.3.

3.1 Theory of Operation and Simulation

A chipless RFID sensor with LC tag is designed and simulated in High Frequency Structural Simulator (HFSS) [71]. The simulated structure along with its lumped circuit model is presented in Figure 3.2. The sensor has a reader coil, which is connected to readout circuitry, a coil, and an interdigitated capacitor on the tag side. The connection in between the readout circuitry and sensing tag is established by a magnetic link in between the tag-coil and reader-coil. The tag is implemented on a flexible substrate Ultralam 3850 from Rogers Corporation with the dielectric constant of 2.9 and dielectric thickness of 100 µm. In practical applications, it is expected that such patterns can be printed on the coatings.

To simulate the lift-off or water ingress process, the distance between the coating and incorporated sensor with the steel pipe is changed and the gap volume is filled with air (ε_r=1) or water (ε_r=80) material. As shown in the simulation results (Figure 3.3), coating lift-off, which is caused by air, demonstrates an up-shift in resonant

frequency; where for water ingress, the resonant frequency has a down-shift variation as a response to the process. The direction on resonant frequency change can be used as an indicator for determining the cause of damage on the pipe coating. This can be described by capacitor change per unit length on the sensor tag (C_t) and its effect on the input effective impedance seen by the readout circuit at the receiver side (Z_{in}).

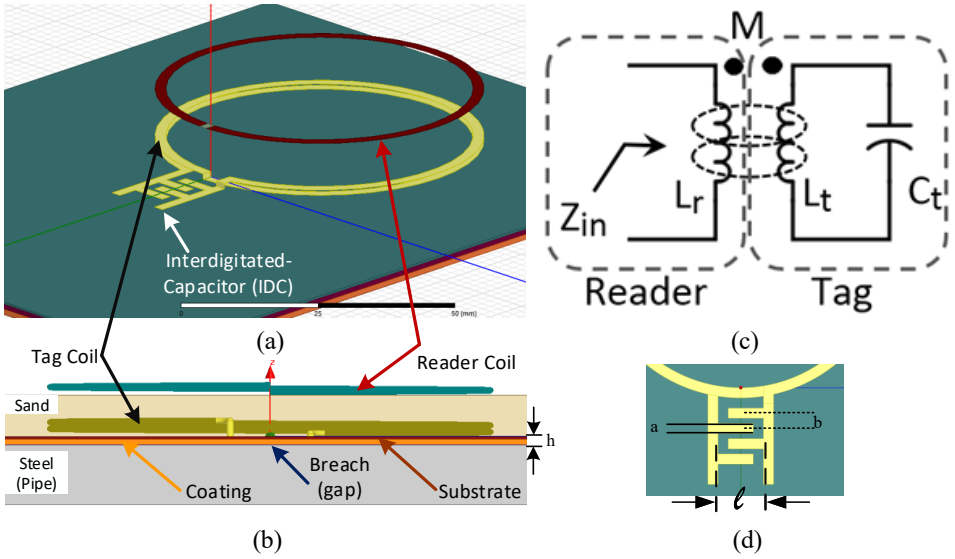

Figure 3.2: Simulated structure in HFSS (a) top view, (b) side view with coating and metal pipe, (c) lumped circuit model of the sensor, and (d) is the IDC design parameters.

As shown in Figure 3.4, the total capacitance of the IDC depends on fringing capacitance through ε_{re1} (C_1), fringing capacitance through ε_{re2} (C_2), the IDC finger space parallel plate capacitance (C_3), the coupling capacitance through the pipe surface (C_S). The overall interdigitated capacitance excluding the impact of the pipe is $C_t = C_1 + C_2 + C_3$ which can be calculated as follows (3.1), (3.2) [72]:

$$C_t = (\varepsilon_r + \varepsilon_s)\,\kappa\varepsilon_0, \tag{3.1}$$

$$\kappa = \frac{l\,(N_C - 1)\,K\left[1 - \left(\frac{a}{b}\right)^2\right]^{\frac{1}{2}}}{2K\left[\frac{a}{b}\right]}, \tag{3.2}$$

where C_t is the tag interdigitated capacitor, ε_0 is the free space permittivity ($\varepsilon_0 = 8.854\times10^{-12}\ F/m$), ε_r is the environment permittivity, ε_s is the substrate permittivity, a, b and l are dimensions defined in Figure 3.2(d), N_C is the number of capacitor electrodes, and K is the elliptic integral of the first kind [72].

The impact of the pipe is considered through C_s which could be mainly calculated based on the two series parallel plate capacitances between the IDC and the pipe surface, calculated as follows:

$$C_s \sim \frac{\varepsilon_{re2}\ A}{h} \tag{3.3}$$

where h is the distance between the IDC and the pipe, ε_{re2} is the effecitve permittivity including the substrate and the air/water breach, and A is the common area between the IDC and the pipe. Breaching of the coating affects the substrate's permittivity (ε_s) in between the sensor and the coating impacts C_s and C_t through variation in h and ε_{re2} and results in variation on the overall capacitor of the tag.

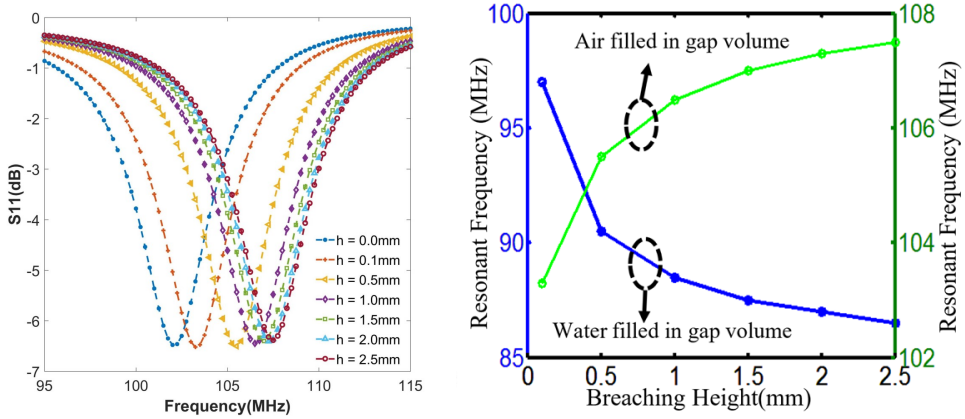

(a) (b)

Figure 3.3: HFSS simulation results for a variant breaching height, (a) S11-parameters versus frequency for different breaching heights with air filled volume, (b) resonant frequency comparison for air and water filled gap volume for variant breaching heights.

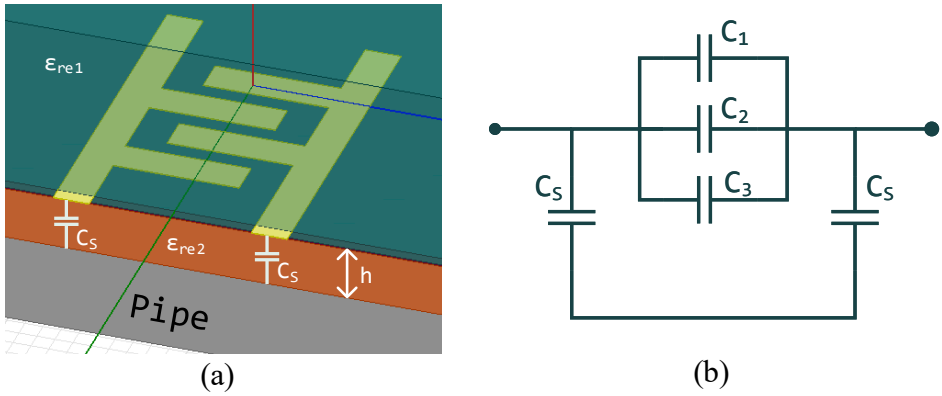

Figure 3.4: Interdigitated Capacitor (IDC) a) Simulated Model, b) Capacitances representations for the simulated model.

3.2 Measured Results and Discussions

The experimental setup is presented in Figure 3.5, where the sensor tag is implemented on a piece of metal pipe with appropriate coating. A Polytetrafluoroethylene (PTFE) polymer tube is placed in between the pipe and coating to bring air and water to create the lift-off and water ingress during the experiment. A mass flow controller is also utilized to control the air flow rate precisely. The implemented tag and metal piece is located under a sand pile with permittivity of ($\sim$ 2.5) and the thickness of the sand between the tag and the reader coil is ($\sim$ 1.0 cm). A Vector Network Analyzer from Agilent (E8361C) measures the return loss parameter (S_{11}) from the reader coil. The initial sensor configuration without purging air or water demonstrates a resonant frequency of 105 ($\pm$ 2) MHz.

Figure 3.6(a) presents the resonant profile variation for different rate of air flow, which causes gap volume variation in between the coating and the metal pipe. The purged Air in the gap volume reduces the effective tag capacitor, and increases the resonant frequency consequently. In contrast, having water ingress in between the coating and the metal pipe increases the effective permittivity in the capacitor environment and leads to down-shift in resonant frequency as shown in Figure 3.6(b).

Knowing the water ingresses volume and the pipe section area, we could translate the volumetric change into mm to be make the simulation results. The direction of the variant resonant frequency can be used as an indicator to distinguish between the two causes of failure in between the coating and the pipe.

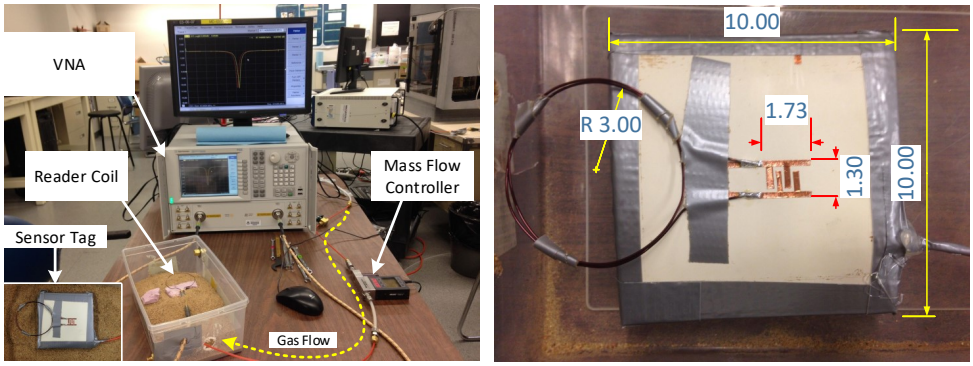

(a) (b)

Figure 3.5: Experimental setup, for liftoff and water ingress measurement between the coating and metal pipe using chipless RFID tag.

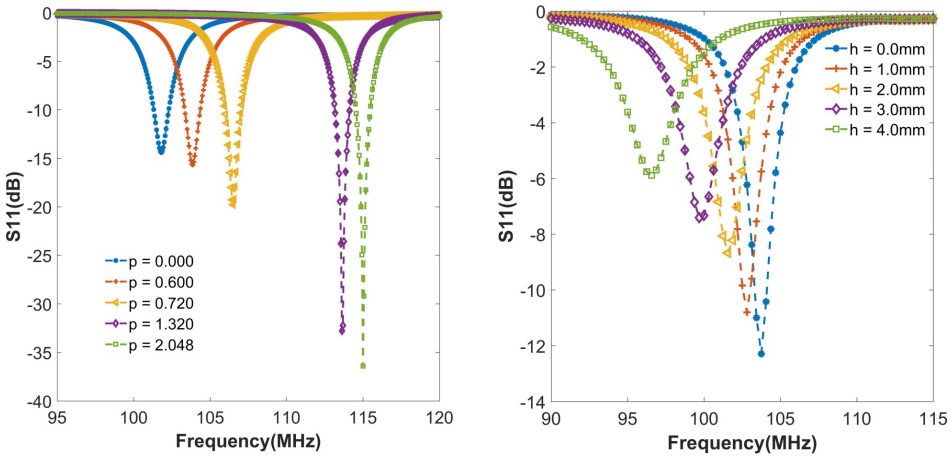

(a) (b)

Figure 3.6: Measured resonant profiles (S11) (a) variant air flow rate in SLPM [volume change], (b) variant water height (mm),in the gap volume between the coating and pipe [volume was translated to gap variation].

To assure accuracy of the results, S_{11} parameters are measured 2 minutes after

applying the air/water purging. In addition, every measurement is performed 5 times and the results are presented with error-bar (Figure 3.7).

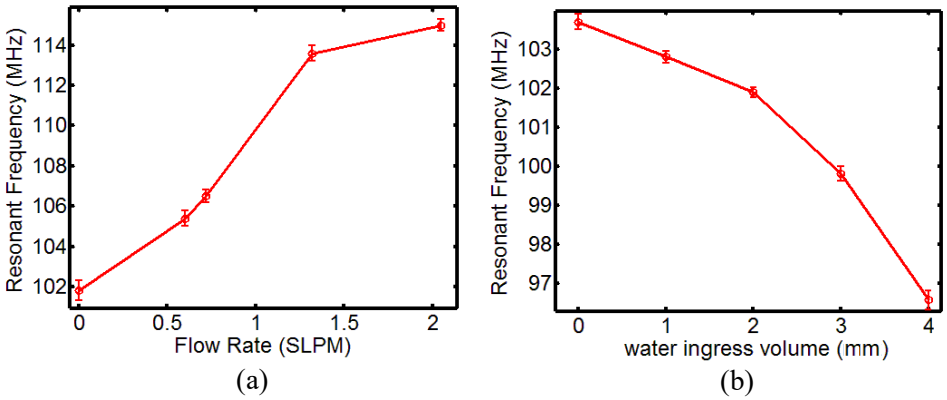

Figure 3.7: Measured resonant frequency for 5 independent experiments, (a) coating lift-off with different air flow rate, (b) water ingress height between the coating and pipe gap [volume was translated to gap variation].

As shown in Figure 3.7, the slope of the resonant frequency variation is positive when the coating to pipe gap volume is filled with air; where it is negative, when water filled gap creates the defect. The results clearly demonstrate that the sensor is capable of distinguishing the two different causes of coating failure and could potentially predict corrosion occurrence.

3.3 Summary

This chapter has proposed a system to predict corrosion using a low-cost stamped-coating solution suitable for smart coating. A resonance-based, passive-wireless sensor is presented for pipeline integrity monitoring by real-time coating inspection. The resonant frequency of the sensor demonstrates a strong relation to the gap between the coating and the metal pipe. The tag is built on a flexible substrate for wrapping around the pipe and to represent the pipe coating. The sensor is conformal, battery-free and low cost which makes it suitable for pipeline monitoring in harsh environments. The sensor's resonator was tuned to 105 MHz with a Q factor of ~115.

The sensor demonstrates the maximum resonant frequency change of 11.7 %, when 2 standard liter per minute (SLPM) of air lifts the coating; and 7.46 % when 4 mL of water ingress happens in between the coating and the pipe. Besides, the proposed sensor demonstrates a selective response to different causes of coating failure, where air lift-off leads to up-shift in resonant frequency and water ingress results in a down-shift of resonant frequency response. The contactless measurement capability of the sensor is suitable for automated readout technologies and IoT from pipeline integrity monitoring.

Chapter 4

Multi-Resonant Chipless RFID Array System for Coating Defect Detection and Corrosion Prediction

The theory and proof-of-concept of the fully-passive RFID-based monitoring system for pipeline integrity were presented in Chapter 3. Compared to the conventional RFID-based solutions, the proposed system achieved battery-free, low-cost, reliable, and contactless technique. However, the low-frequency introduced can lead to lower resolution in addition to the difficulty for mass-production. In this chapter, the combination of an expandable resonator-based sensor array and a patch-based tag antennas is investigated to achieve a fully passive, wireless solution for out-of-sight pipeline monitoring, as illustrated in Figure 4.1. Using such a combination, a flexible and single-layer sensor array design was achieved for easy to install/stamp providing mass-production capability. The structures are all low-cost conductive patterns that can simply be stamped or printed on the coating.

This chapter is organized as follows. First, Section 4.1 outlines the proposed system design and its main components. In section 4.2, the sensor array design and its measurements are introduced. Detailed wireless communication setup and antenna design are discussed in section 4.3. In Section 4.4, the in-lab setup for the proposed system and its measurement are then presented. Lastly, research challenges are discussed in

Section 4.5 followed by a summary of the chapter in 4.6.

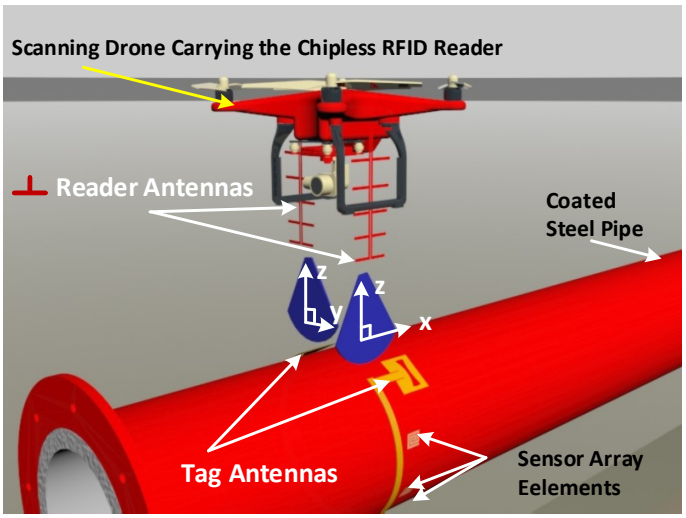

Figure 4.1: Chipless RFIDs distributed along the pipeline and a drone scanner holding the reader circuitry.

4.1 Proposed System Design

Figure 4.2 shows the block diagram of the proposed system shown in Figure 4.1, including its main subcomponents. The system is composed of the sensor array, the sensors' sending/receiving antennas extended above the pipe surface, and reader antennas [73]. The sensor array would be installed at the underside of the pipe where there is no direct line of sight with the reader antenna

The sensor array will generate the spatial signature for the design, and a wide-band reader antenna is required for the interrogation and communication of the data. Since a low cross-polarization is needed to overcome the cross-talk problem, linearly-polarized sensor/reader antennas are developed. All of system elements are passive, and can utilize the system reciprocity theory to send/receive data either way that both reader and tag antennas are cross-polarized configured. An aerial surveillance drone could be used to align the reader antennas (and associated circuitry) for scanning through the longitudinal extent of the pipeline as depicted in Figure 4.1.

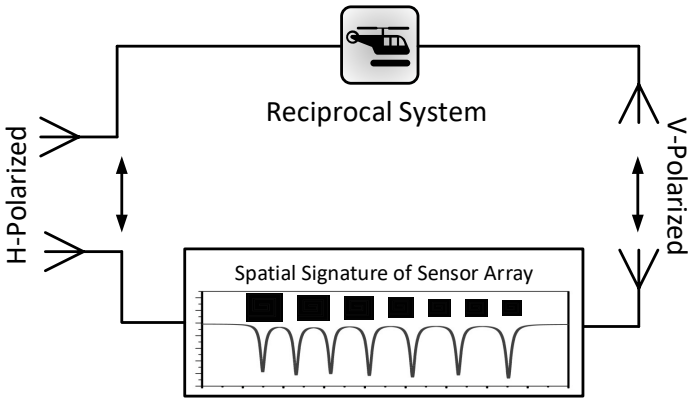

Figure 4.2: Proposed design schematic of the system presented in Figure 4.1 to show the chipless RFIDs, tag antennas, and reader antennas with its cross-polarized communication.

4.2 Sensor Array

The tag array consists of six non-identical microstrip rectangular spiral resonators, popular for their low profile and compact design. Figure 4.3 shows the spiral parameters and its equivalent lumped circuit [74]. The resonator creates a narrow stop band (notch) at its resonance, and can represented by series RLC_r circuits - shown in Figure 4.3(b). At resonance, the resonator can be modeled by parallel RLC_{eq} circuits [74] owing to its blocking characteristics when coupled to the transmission line of 50 Ω (corresponds to W_f in Figure 4.3). The spiral is both magnetically- and electrically-coupled to the resonator with coupling coefficients L_m and C_m [75, 76] and resonant frequency f_r can be defined as [77]:

$$f_r = \frac{1}{2\pi\sqrt{C_{eq}.L_{eq}}} \tag{4.1}$$

where C_{eq} and L_{eq} are the total equivalent capacitance and inductance of the LC tank shown in Figure 4.3(c), respectively. At the resonant frequency, the coupled resonator reflects the signal back, thus acting as a notch band.

By cascading multiple resonators, a frequency signature structure of a series of stop bands to cover our target can be created. As shown in Figure 4.3(a), l_s is the

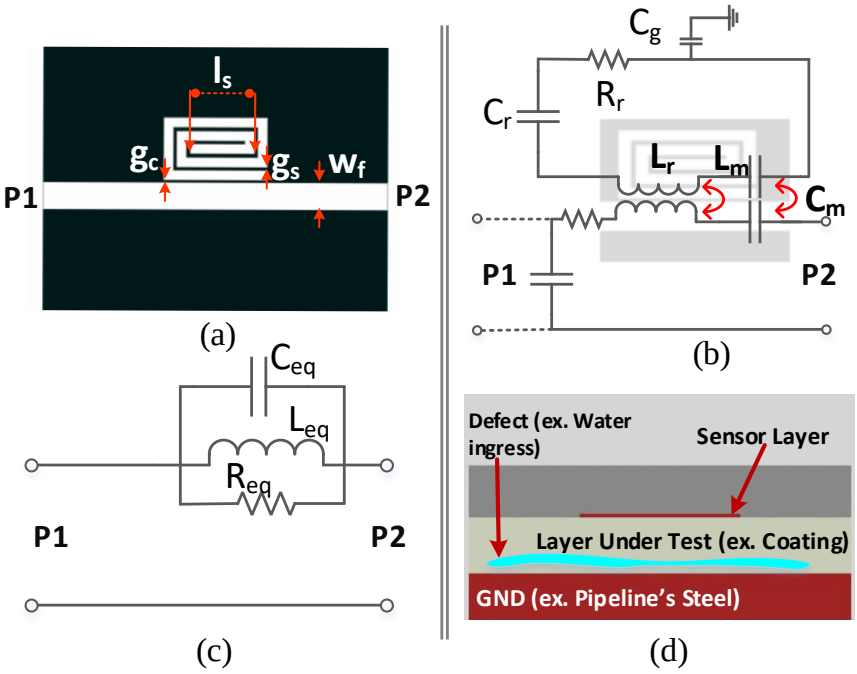

Figure 4.3: The equivalent circuit for the spiral resonator a) The spiral resonator, b) It's an equivalent circuit, c) Equivalent circuit at resonance state, and d) cross section showing the defect location under the sensor layer.

basic length which determines the highest/lowest resonant frequency. Parametric optimization by addition/subtraction of a fixed length (*delta*) controls the frequency span of each resonator by a value that can determined using:

$$L_{Sn+1}=L_{Sn}+delta;$$

The arrangement is such that the preceding resonator is shorter by a length (*delta*) across the array, thus making them unidentical in sizes. Doing this invariably increases the spiral's total length by five (5) times of *delta*. The distance between two consecutive resonators is kept at a fixed value s of 0.8 cm as shown in Figure 4.4. The frequency response of such an array is shown in Figure 4.5 which shows seven (7) distinct resonances in response amplitude and seven (7) disturbances in the response angle.

Each sensor's size is optimized to achieve a sharp and distinct resonance between consecutive resonators. This prevents any frequency overlap between them, allowing for dynamic range of the readings. This also determines the geometrical difference between the respective sensors (l_s). The separation (s) between the sensors is chosen firstly to be greater than a quarter guided wavelength ($\lambda_g/4$), however, the choice of the distance is flexible and can be adjusted according to coverage requirements. The separation (s) also determines coupling strength between adjacent resonators [78]. This will be vital for further studies on detecting between the sensors as well.

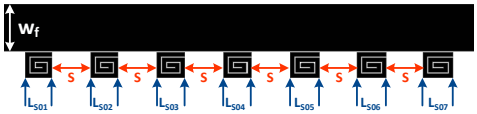

Figure 4.4: The sensor array design showing a gradual length increase/decrease corresponding to a frequency decrease/increase.

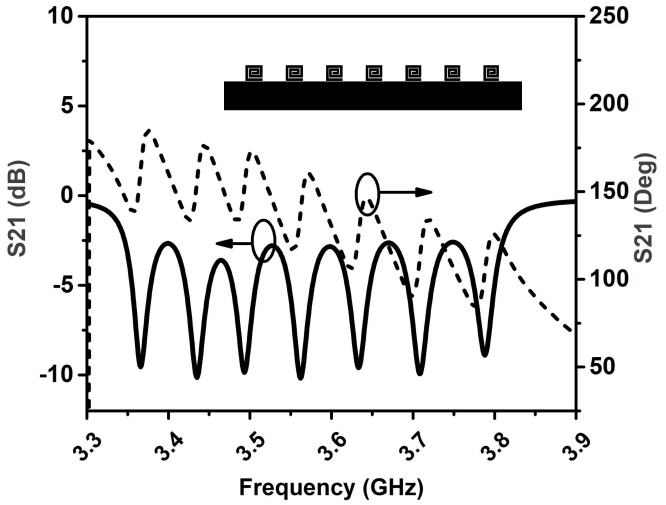

Figure 4.5: Simulated Transmission coefficient (S21) in magnitude (in dB) and phase (in Deg.) for a 7-spiral array.

4.2.1 Conformal Flexible Sensors Array Measurement

Prior to embedding the sensor tag antennas, investigation of the feasibility of the sensor array to identify defects in the coating layer. Figure 4.6 shows a diagram of the measurement setup used for the proof-of-concept. It started with a bare pipe (carbon steel) of length 11 cm, a diameter of 14 cm, and thickness of 4 mm. Then a 3 mm of Teflon layers (2 mm and 1 mm) were added, which represent actual pipe coating. The 2 mm Teflon layer was engraved and fit with seven polymer tubes, each centered below a resonator as shown in Figure 4.6(b). The sensor array was printed on a flexible skin-thin substrate of RT/duroid 5880 ($\varepsilon_r = 2.2$ and $tan\delta = 0.0009$) of thickness 0.127 mm. Lastly, the flexible sensor array was affixed around the pipe's circumference as shown in Figure 4.6(a). A copper tape was used to connect the SMA ground to the pipe steel as a GND reference. The in-lab design setup is shown in Figure 4.7 while its measured S-parameters are illustrated in Figure 4.8. It is shown that there are 7 distinct frequency resonances with 7 notch bands. Each of these frequencies is directly from one of the resonators.

A syringe was used to inject water below the resonators through the polymer

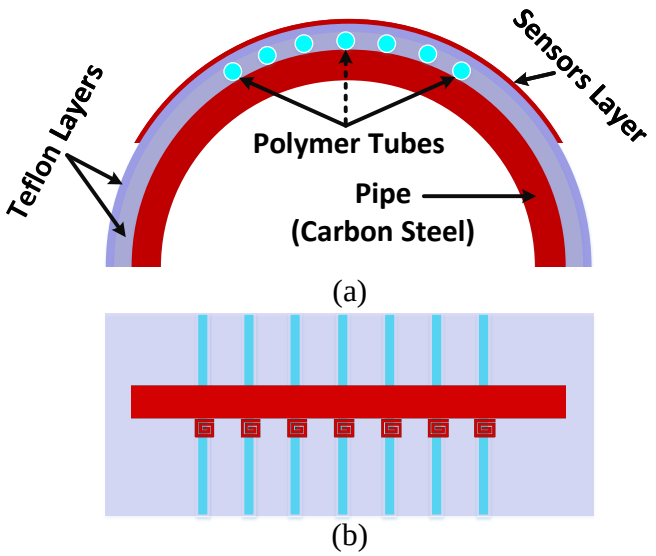

Figure 4.6: Schematics show the sensors' arrangement on a pipeline coating layer with polymer tubes to insert water below sensors and within the coating layer.

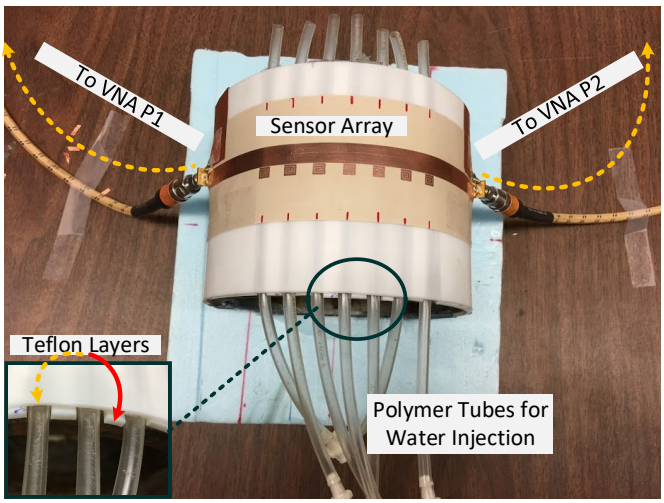

Figure 4.7: Lab setup for testing the sensors before embedding the tag antennas.

pipes one at a time. The measured transmission coefficient (S21) for the sensor array is shown in Figure 4.8 in terms of both amplitude and phase. Seven dips (dotted line) are shown as an amplitude response signature and seven disturbances (solid line) indicating phase responses. The signature is therefore detectable either by magnitude or phase response, thus providing some degrees-of-freedom with respect to measurement accuracy. When water was injected into the polymer tube, it was noticed changes in both frequency and phase responses associated with the surfacing resonator, while other responses were undisturbed. Figure 4.9 (a-d) depicts this, using resonators S01, S03, S05, and S07 as examples. The responses reverted to original form when water was ejected from the tubes, demonstrating a stable and reversible detection technique.

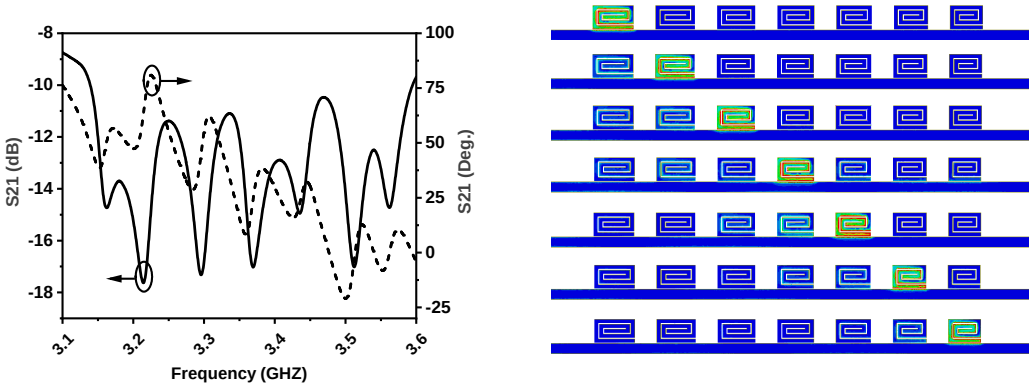

(a) (b)

Figure 4.8: Amplitude and Phase response of the transmission coefficient of the sensor array showing 7 amplitude notches and 7 phase disturbances in a), and b) The Electric field distribution (in Mag. [V/m]) at each resonance frequency.

4.3 Integrated Sensor System

4.3.1 Antenna Performance within metallic Structure Proximity

To communicate with the tag sensor array, two tag antennas are required. These antennas are to be printed conformally on the pipe surface. This section outlines the

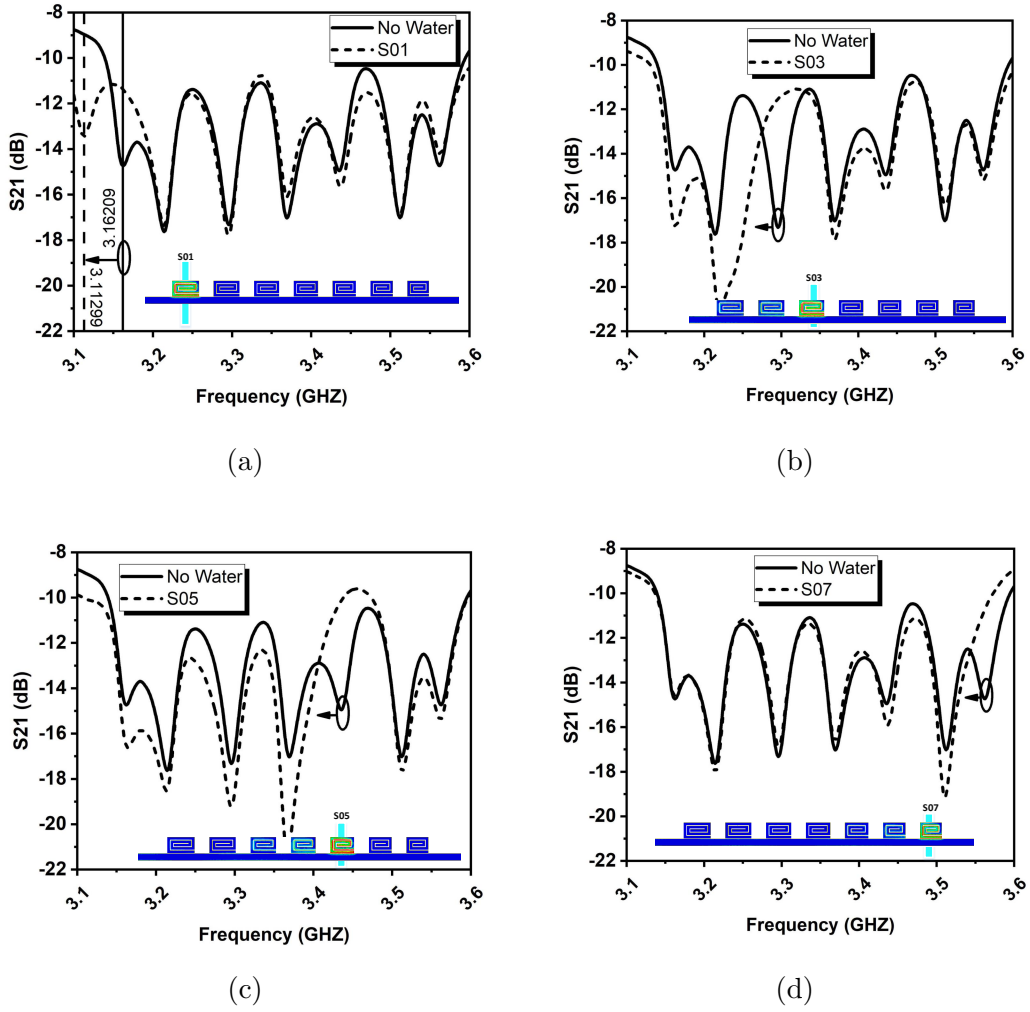

Figure 4.9: Measured transmission coefficient amplitude response (S21) when injecting water beneath the sensor S01 (a), S03 (b), S05 (c), and S07 (d).

design details of the sensor tag antenna.

Design of a wideband antenna to be surface-mounted on a metallic pipeline is very challenging. The pipeline coating is considered as the substrate, while the pipeline itself becomes the metallic ground layer. Therefore, the antenna and its feed system should be in the same layer. Though the pipeline could be used as a potential ground; there is no direct connection to this layer. For our project, a use of a Teflon substrate ($\varepsilon_r = 2.1$ and $tan\delta = 0.001$) with a thickness of 3 mm to represent the well-known coating of fusion-bonded polyethylene ($\varepsilon_r = 2.25$ and $tan\delta = 0.001$), with a $3mm$ coating thickness [79]. This material is a popular pipeline coating in the oil and gas industry and has been strategically chosen as the substrate for the sensor array and its antennas. For these tag antennas to serve effectively as a transponder to our sensor array, the tag antennas are expected to be wideband to cover the frequency span of the array.

Looking at Figure 4.1 and Figure 4.2, it is evident that communication requires two side-by-side antennas to transmit and receive between the tag and reader antennas. To minimize cross-talk, a two linearly-polarized antennas patterned orthogonally to each other were proposed.

To overcome the design constraints, patch antennas were chosen due to their features of being conformal, low-cost, low-profile, and non-intrusive. Consequently, the metallic surface of the pipeline can be exploited for use as a ground plane. This could solve the metallic structure proximity but will limit the antenna bandwidth (BW); hence, various broadbanding techniques such as parasitic patches or slots [80, 81] have to be used. The following section explains the proposed antenna structure.

4.3.2 Tag Antenna: Tapered-slot patch antenna

As discussed earlier, the patch antenna is a preferred candidate to utilize the pipe's metallic structure as a ground plane. Although the patch antenna is a low-cost, low-profile, and simple design, it suffers narrow BW. There are many broadening

techniques used to improve patch antenna BW such as resonance overlapping, parasitic patches, stepped notch, introducing slots and slits, etc. [81]. To make the tag design as simple as possible, slots were introduced to the patch. Many types of slots were used in patch antennas to increase the BW such as rectangular slot [82], V-slot [83], U-slot [84], and circular slots [85, 86].

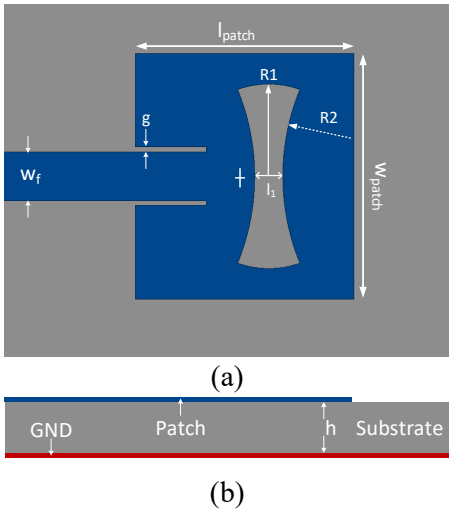

Figure 4.10: Microstrip patch antenna with microstrip line feed and meandered-shape slot. a) The designed patch antenna with shown dimensions, b) side view of the structure.

Here, a new slot shape for the patch antenna designed for the application in hand is presented. We initially started with a stepped-impedance slot which is document in [87]. Then, a tapered slot is proposed to broaden the patch BW by introducing (and overlapping) a new resonance in proximity to the patch resonance. Figure 4.10 and Table 4.1 show the optimized patch parameters and dimensions after using Ansys HFSS for parametric optimization. The current distribution in magnitude at each resonance is shown in Figure 4.11. At 3.75GHz, the introduced slot generated the current path, while at 3.65GHz, the main patch current path was dominant. The reflection coefficient and the antenna radiation patterns are shown in Figure 4.12 and Figure 4.13 respectively. The antenna has a BW of 0.35GHz and achieved a gain of 7 dB. Since linear polarization was required by the design for minimal cross-talk, a

cross polarization as low as -30 dB was achieved as shown in Figure 4.13.

Table 4.1: Microstrip Patch with Tapered-Shape Slot Dimensions.

Parameter	Length (mm)	Parameter	Length (mm)
w_f	9.5	g	1
l_{patch}	43	w_{patch}	48.2
R_1	18.1	R_2	45
l_1	5.5	h_1	0.13
h_2	3		

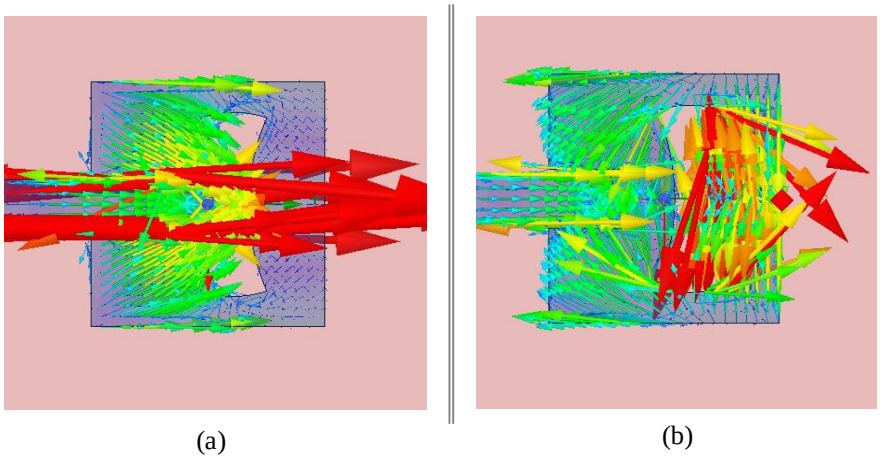

Figure 4.11: Current distribution (magnitude) of the patch antenna a) at 3.56GHz, and b) at 3.75GHz.

Lastly, integration of the sensor array and the antenna in one design and fabrication on a flexible substrate were introduced as shown in Figure 4.14.

4.3.3 Reader Antenna: Log Periodic Dipole Antenna

A high-gain, linearly-polarized and highly-directive reader antenna is required to achieve directional reading. Figure 4.15 shows a linearly-polarized Log Periodic Dipole Antenna (LPDA) and its dimensions [44]. Ansys HFSS was used in the optimization process. The final dimensions and the fabricated antenna are depicted in Figure 4.15.

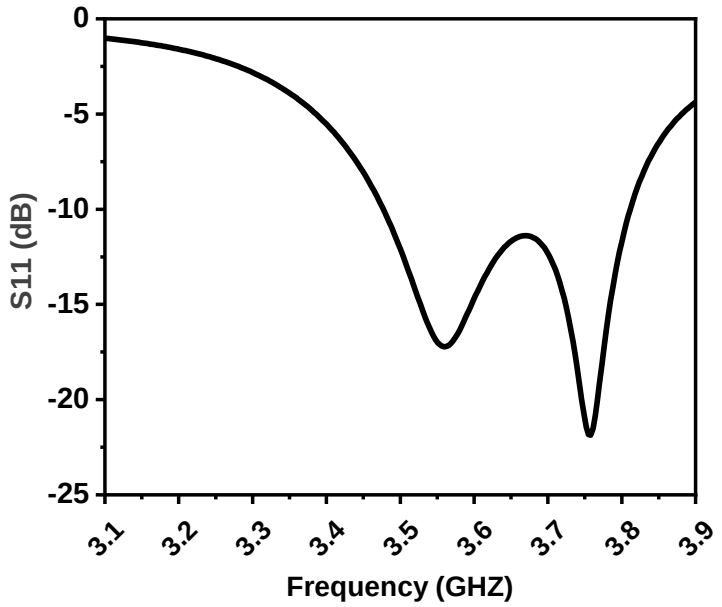

Figure 4.12: Reflection coefficient (S11) the tapered-slot patch antenna.

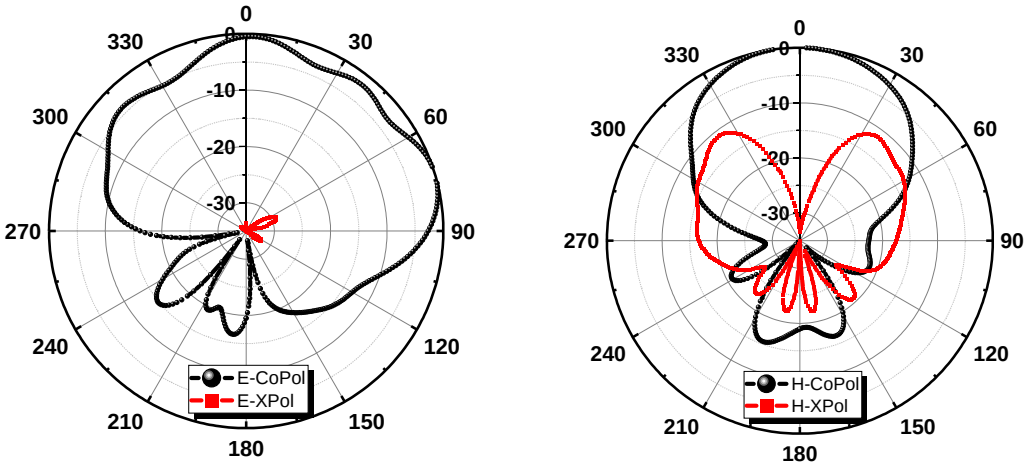

(a) (b)

Figure 4.13: The simulated radiation pattern (in dB) for the designed tapered-slot patch antenna a) E-Copol[dark]; E-Xpol[red], and b) H-Copol[dark]; H-Xpol[red].

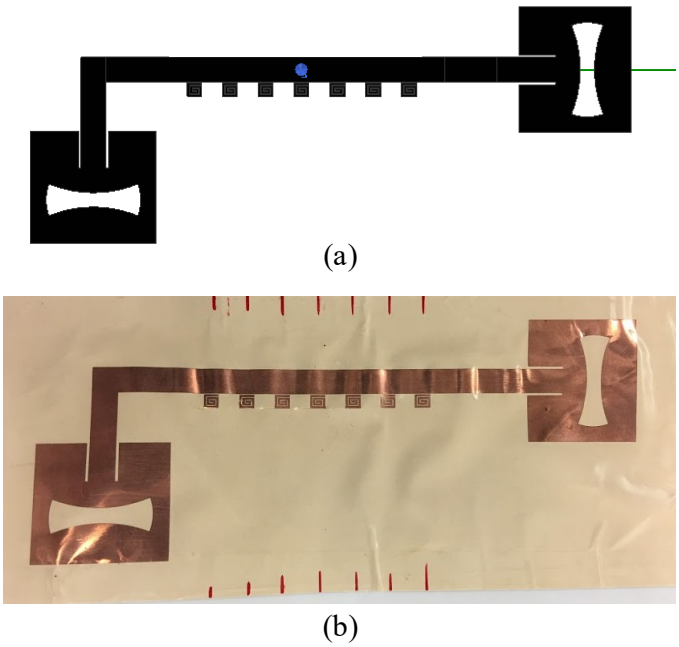

Figure 4.14: Fully integrated tag shows the sensors and the send/receive antennas.

Figure 4.16 shows the reflection coefficient (S11) of the proposed LPDA antenna illustrating its wideband behaviour over the frequency band of interest. The simulated antenna radiation pattern in E- and H-planes is shown in Figure 4.17. Due to the absence of the balun for the LPDA (directly connected to the SMA as shown in Figure 4.15), the radiation pattern used in the actual system would differ from simulated radiation pattern in Figure 4.17 from the symmetry point of view.

4.4 System Setup and Measurement

Figure 4.18 shows the complete in-lab setup for the proposed work. The same piece of pipe used in the previous section is employed. The RFID tag, consisting of an array of 7 sensors, is integrated with the two cross-polarized antennas. Tubes are incorporated within the Teflon coating, centered beneath the sensors. Injecting water into the tubes allows for testing of water ingress between the coating and the pipe surface. The reader antennas were aligned according to their polarization to match

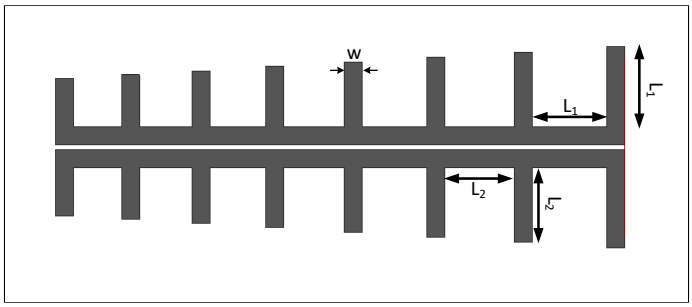

(a)

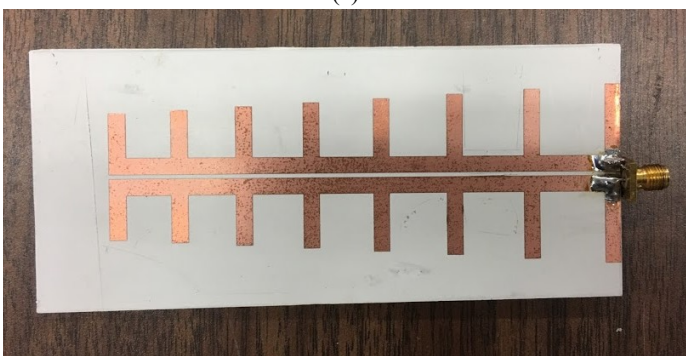

(b)

Figure 4.15: The designed and fabricated reader antenna (8-element LPDA) with $L_{n+1} = \tau L_n$ where $L_1 = 17\ mm$ and $\tau = 0.93$ etched on Rogers RO3003 substrate with $\varepsilon_r = 3$ and $tan\delta = 0.0013$ with thickness $t = 1.52\ mm$.

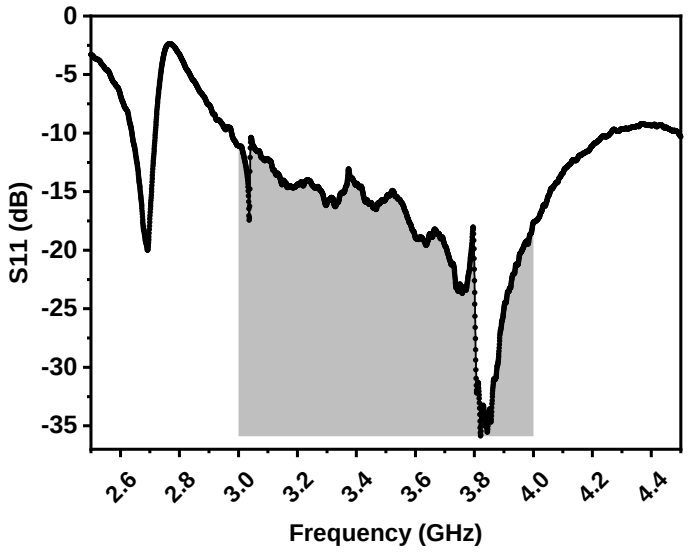

Figure 4.16: The measured reflection coefficient (S11) for the designed reader antenna (8-element LPDA).

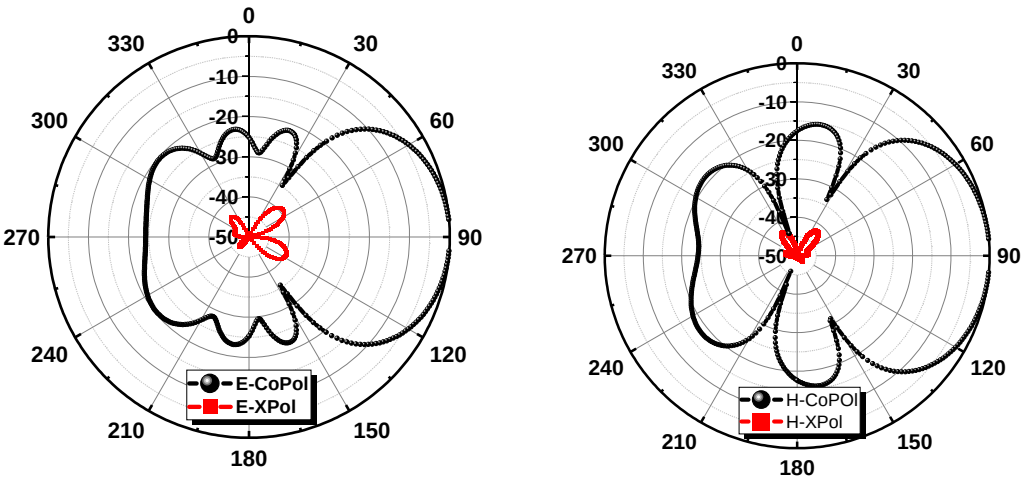

(a) (b)

Figure 4.17: The simulated radiation pattern (in dB) for the designed reader antenna (8-element LPDA), a) E-Copol[dark]; E-Xpol[red], and b) H-Copol[dark]; H-Xpol[red].

the two cross-polarized tag antennas as shown in Figure 4.18.

The same procedure was repeated to inject water below each sensor, one at a time. The signal path starts at one of the reader antennas, then continues to the corresponding tag antenna. The signal then passes through the transmission line, which is coupled to the sensor array, to the second tag antenna. Lastly, the second reader antenna will read the scattering signal from the tag antenna. Our measurement data is based on the transmission coefficient (S21).

To examine the sensors' behaviour, it started by shorting the resonators and monitoring the specific resonant behaviour. Figure 4.19 shows the S21 when all resonators are shorted. It was successfully verified all sensors locations in a consecutive order during this experiment.

Figure 4.20 and Figure 4.21 presents our measured data for different states and defect locations. All the sensors from S01 to S07 are evaluated, measured, and presented. It is clear from Figure 4.21(a) that when S07 detects water in the tube, the resonant frequency shifts and the correlated notch vanishes. This trend is also ap-

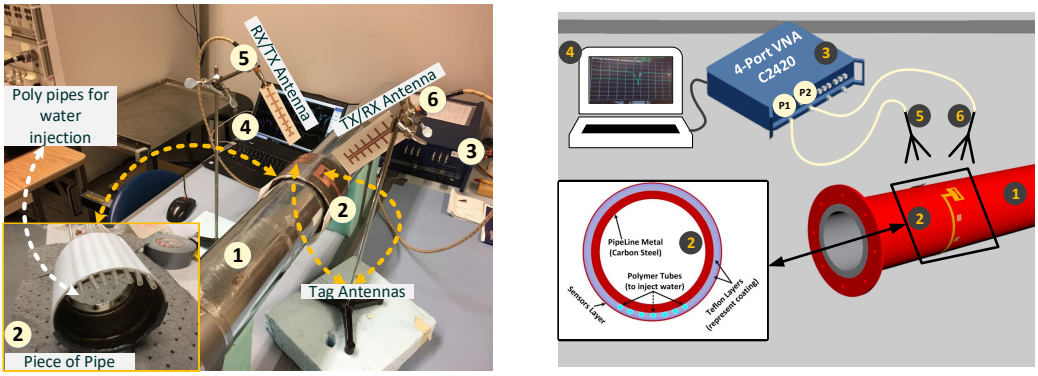

(a) (b)

Figure 4.18: The in-lab setup for the proposed system measurement in (a), and the block diagram shows the setup connections in (b).

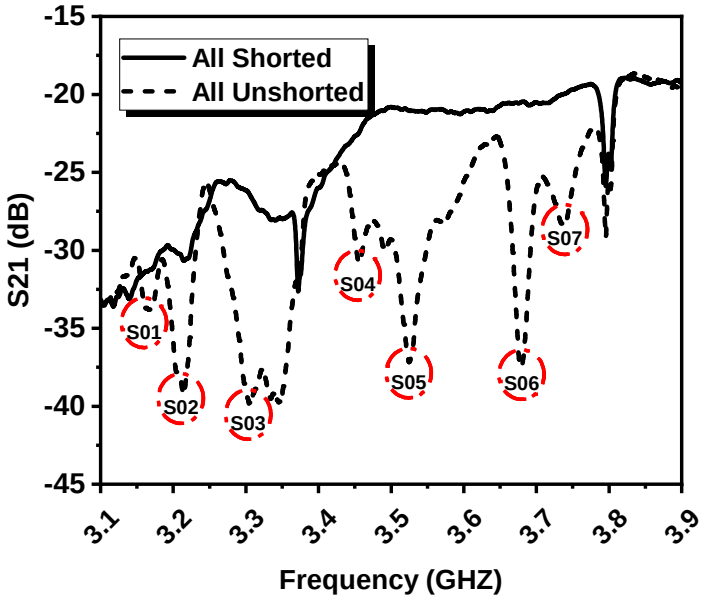

Figure 4.19: The transmission coefficient (S21) of the whole system when shorted/unshorted resonators to locate them in the frequency spectrum.

parent from S06 where the sixth resonant disappears in the presence of water. S05 and S04 also exhibit distinct shifts in the corresponding resonant frequencies. The same trend is similarly observed for the remaining sensors. It is worth noting that for the frequencies of less than 3.3GHz, the sensor operating frequency falls outside of the antenna direct well-matched BW. Thus, the sensor resonant frequency shift is less evident when compared to the passband of the antenna at 3.4GHz to 3.8GHz. This problem could be better addressed if an antenna with wider BW is employed.

4.5 Discussion

4.5.1 Predictive Approach

This work presents a completely new approach to achieving a corrosion free pipeline, especially suitable for lines in remote areas. To date, standard approaches focus on detecting corrosion and quantifying the problem after it has occurred. The proposed approach is completely different. We target "*prediction*" of corrosion before occurrence. This is done by monitoring the environmental conditions around the pipeline coating. The proposed design is based on chipless RFID tags which do not contain any passive or active components or IC chips. The fact that the chipless RF tag is to be installed on a pipe imposes design and realization challenges that have been outlined in the paper. The cross-polarized tag and reader antennas ensure that cross-talk between the two links is minimized.

In coordination with the entire system, the tag can detect coating delamination or water ingress, both of which can initiate corrosion. Predicting corrosion through early detection of these precursor events allow for a proactive response, rather than reactive. Adopting a proactive response mitigates risks to the environment and company assets and productivity.

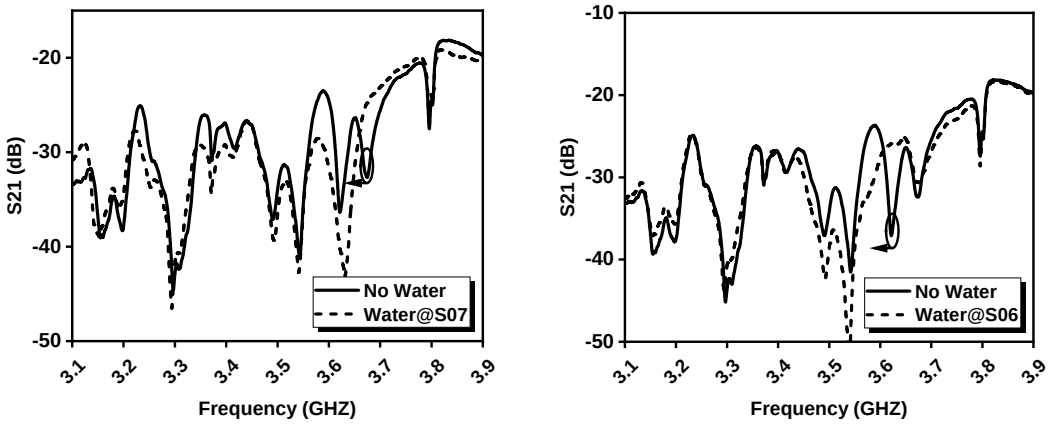

(a)

(b)

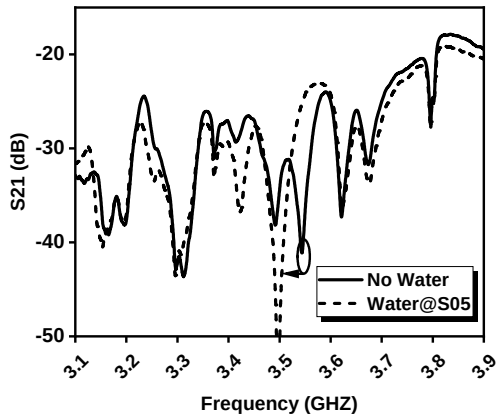

(c)

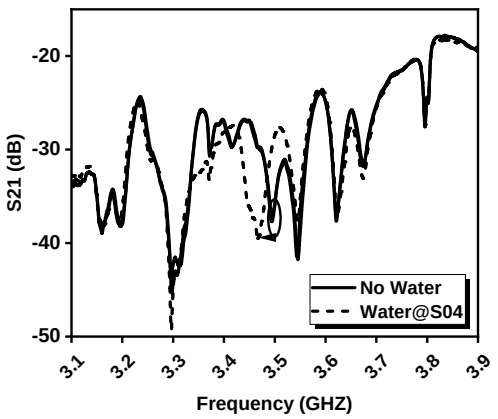

(d)

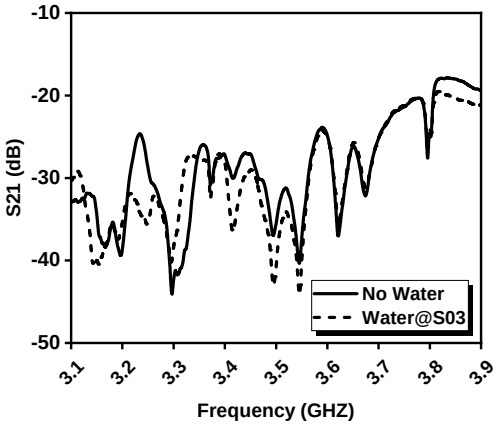

(e)

Figure 4.20: (a-e) The measured transmission coefficient (S21 in dB) when injecting water beneath the 7^{th}–3^{rd} sensor (S07-S03)

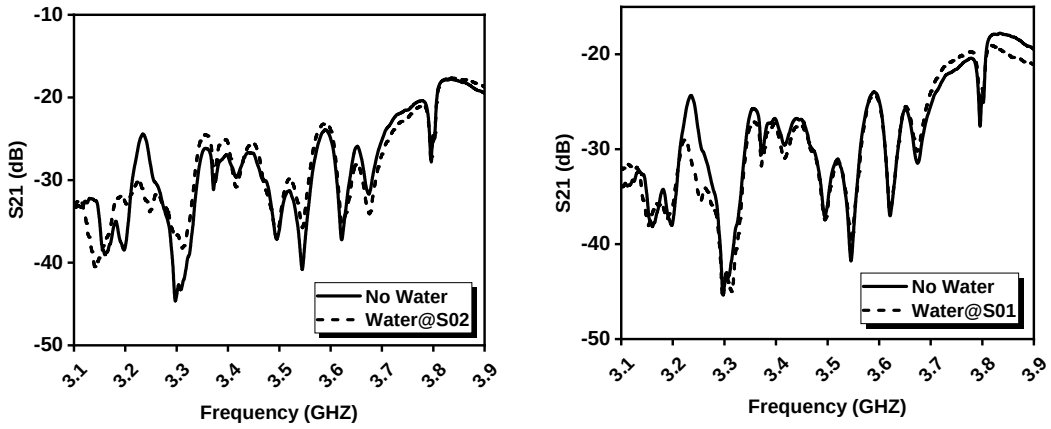

(a) (b)

Figure 4.21: (f-g) The measured transmission coefficient (S21 in dB) when injecting water beneath the 2^{nd}– 1^{st} sensor (S02-S01)

4.5.2 Sensor Array Manufacturing and Material Considerations

In practice, the system elements shown in Figure 4.1 can be implemented in the pipeline field with manufacturing challenges in mind. The sensor tag, which is comprised of the resonator array and the Tx/Rx patch antennas, requires a conductive material. One potential conductive material could be Silver Nanoparticle ink, for which its conductivity is dependent on the particle size, shape, and distribution [44, 88]. Therefore, this can offer a cheap and promising ink. The tag can be printed or stamped on the coating layer during pipeline manufacturing. For printing process, thermal spray techniques can be used for mass production after the coating application phase [89]. The sensor layer will be protected using additional material on top of it to eliminate direct contact with the pipeline surrounding electrolytes (such as humid air or water). This layer could allow the sensor layer to be made from cheaper materials such as copper or aluminum instead of the silver ink. In this work the focus is on onshore pipelines, with ease of access for the reader in-mind.

4.5.3 RF System design

Choice of the frequency for use in this application involves a trade-off when considering lower and higher frequency ranges. Lower frequencies, such as in the Megahertz or Kilohertz range, would create much larger sensing footprints, thus providing poor spatial resolution. Additionally, the antenna structures would become much larger and less practical. On the other hand, higher frequencies impose challenges in the readout circuitry. Either the technologies are not readily available or are very expensive. Therefore, using RF range creates an optimum balance between the readout technology and the physical structures.

Chipless RFID reader circuitry for short range applications was introduced in the literature [73, 90, 91]. The readers were designed for UWB that could cover a wide range for frequencies and allow for cascading the sensors and long arrays required for monitoring purposes. Such reader systems encompass three main sections: digital/control section, RF section, and Tx/Rx antennas. The reader, including the antennas, can be mounted on scanning vehicles or drones. The onshore pipeline can then be scanned for early defects. A 3D model of the system implementation in the field is shown in Figure 4.1.

Currently, the proposed sensor can be monitored with two antennas at a distance of 7cm. This distance is suitable for monitoring above the ground pipelines. For buried pipelines, although it is expected that the sensors operate with no problem, the soil type, and its wetness impact the communication link. For such scenarios, the communication link should be further optimized. The communication range could be increased by improving the antenna gain, reducing the transmit antennas cross coupling, and enhancing the antenna.

To cover a longitudinal area of the array, more of these arrays could potentially be installed in parallel. Although, there is no limitation on the number of the possible arrays, challenges in installing them close together are anticipated. To have

multiple arrays, cross coupling in the antenna and communication links must further investigated.

4.5.4 Comparison of the Proposed Technique

Table 5.2 below summarizes the performance of the system proposed in this work and compares it to other research utilizing the same technology (RFID) to detect corrosion. It is clear from the comparison table that the proposed work is the first solution to-date that focuses on predicting corrosion using chipless RFIDs. Although the proposed sensor requires short distance reader and tag communication (suitable for crawling or proximity flying drones), it enables out of sight detection. To the authors' knowledge, this work is the first of its kind.

4.5.5 Minimum Detection Requirements

Minimum detection is a quantity that is defined by instrumentation industry and generally is referred to the early detection of the smallest corroded area. As this work focuses on predictive approach, it is expected that the proposed sensor to satisfy all the stringent requirement. However, the predictive approach also has its limitations. Based on the results presented in Figure 4.20 and Figure 4.21, the frequency shift (in average) is 48 MHz. The lower the readout electronic frequency detection resolution, the lower volume of water ingress can be detected. Thus, the minimum detectable water will highly depend on the final readout and tag integrated system. It should be noted that the corrosion might even happen if a monolayer of water penetrates in between the coating and the pipe for long time, which requires further investigation to reach such level of detection.

4.6 Summary

In this chapter, an integrated chipless RFID system for pipeline integrity monitoring was proposed. This system allows for prediction of out-of-sight coating defects in

Table 4.2: Literature comparison with the proposed work.

Ref.	Chip/ Chip-less	Application	Detection/ Prediction?	The tag (sensor)?	Off-sight detection?	Pwrd?	Read Range?
[18, 92]	Chip (Passive)	coated/ uncoated steel plates	Detection	Off-the-shelf LF RFID (125 kHz) coil antenna	No	No	4.5 cm
[93]	Chip (Passive)	uncoated steel plates	Detection	Off-the-shelf HF RFID (13.56 MHz) coil antenna	No	No	0.5-2.5 cm
[25]	chipless	coated steel in coastal zones	Detection	Stub-based-resonator sensors (450 MHz) with T/RX Microstrip antennas (S21)	No	Yes	150 cm
[94]	Chip (Passive)	coated steel samples	Detection	3D Antenna (patches) (940 MHz)	No	No	100 cm
This work	**Chipless**	coated pipelines	***Prediction***	Planar Spiral-based-resonator sensors (3.5 GHz) with T/RX Microstrip antennas (S21)	**Yes**	No	7 cm

real-time. Sensor array composed of distributed spiral resonators each creating its spectral frequency signature were used. The resonant frequencies of these structures are utilized as measures for sensing the corrosion causes in pipeline. Two pairs of tapered-slot patch antennas and Log Periodic Dipole Antennas are utilized to transmit and receive the signal, respectively. The resonant frequencies of the sensors are then monitored and tracked. It is shown that the presence of water can be identified and monitored wirelessly. To realize the pipe coating in experiment, a 3 mm Teflon layer is utilized for its similar electrical characteristics to polyethylene, which is commonly used as pipe coating. The sensor is fabricated on a flexible material and conformably wrapped around the pipe. It is demonstrated that the system can detect out-of-sight defects while communicating to the reader.

Chapter 5

Long Array of Microwave Sensors for Real-Time Coating Defect Detection

In Chapter 4, a resonance-based sensor array was introduced for pipeline integrity monitoring. Each resonator has a unique frequency signature which facilitates the detection process, however, it limits the expansion of the array for large surfaces due to the harmonics overlap with the fundamental frequencies. This chapter, on the other hand, will introduce a novel SHM method for monitoring the external surface of any coated metallic structure such as a tank bottom plate or pipelines as shown in Figure 5.1. A sensor array is utilized, which is comprised of identical and equidistant rectangular spiral ring resonators (RSRR) electromagnetically-coupled to a transmission line [95]. Each RSRR creates a notch band frequency response with very high isolation, tuned to operate in the ISM band (2.57 GHz). When the sensor's environment is altered, such as a result of coating defects like liquid ingress or air breach, a resonance(s) for the affected sensor(s) will be formed (shifted) according to the damage severity [96].

An initial prototype for testing tanks of 1-1.5 m (3-5 ft.) diameter is investigated and can be extended to larger diameters based on the theory of the technique. The system can be used for on-site application by having access to the two-port network, or for in-situ application by connecting the system to a wireless sensor network using

transceiver systems [73]. The system has the capability of real-time monitoring for corrosion prediction in harsh or inaccessible environments. It has the versatility for mass installation on existing structures and facilities, or for inclusion in manufacturing of a smart structure as a lifetime cycle monitoring system.

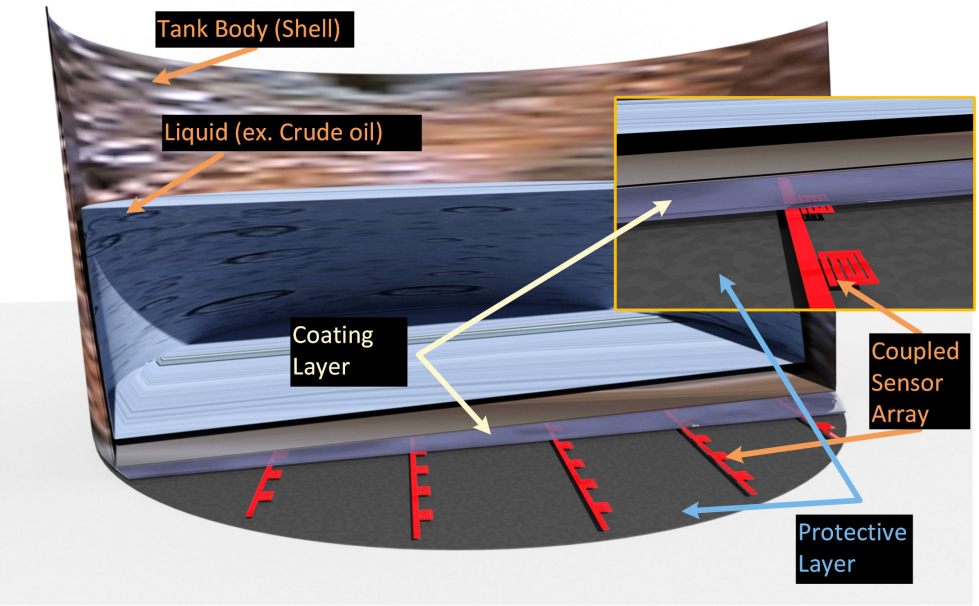

Figure 5.1: A 3D model shows the distributed sensor array for application on the bottom of an oil tank.

Theory and modeling of a single element sensor will be introduced in Section 5.1 which focuses on calculating resonator elements (R, L, and C) as well as the coupling capacitance between the sensor and the transmission line. The array design, simulation, and measurements for 11-element array are introduced in Section 5.2. Finally, an integration of 11-element flexi array with four PCB 11-element arrays were combined in Section 5.3 and Section 5.4 to make the 55-element sensor array.

5.1 Single Element Sensor Theory and Modeling

The key element in our design is a rectangular spiral resonator; known for its low profile, tunability, and small size when compared with open-loop resonators and the miniaturized hairpin resonator [97]. In this section, we closely study the resonator

behavioral model and its equivalent lumped circuit representation to accurately understand the interaction between the successive sensors and surrounding environment.

5.1.1 Series Resistance:

The series resistance R of a resonator can be estimated from the geometry and the material resistivity using [98]

$$R = \frac{\rho l}{w_s t_{eff}} \tag{5.1}$$

where ρ is the resistivity in Ωm ($\rho = 1.68 \times 10^{-8}$ Ωm for copper), l is the total length of all spiral segments, w_s is the spiral width as shown in Figure 5.2(a) and t_{eff} is the spiral conductor effective thickness which is a function of the skin depth as

$$t_{eff} = \delta(1 - e^{-t/\delta}) \tag{5.2}$$

where t is the spiral conductor thickness as shown in Figure 5.2(b) and δ is the skin depth and is defined as

$$\delta = \sqrt{\frac{\rho}{\pi \mu f}} \tag{5.3}$$

where μ is the permeability in H/m and equal to $\mu_0 \mu_r$ where μ_0 is permeability of free space ($4\pi \times 10^{-7}$ H/m) and μ_r is the relative permeability (unity for copper), and f is the frequency in Hz.

5.1.2 Resonator Inductance and Capacitance Based on Transmission-line Based Model:

The spiral resonates close to its half-guided-wavelength ($\lambda_g/2$) so we can consider it as two series $\lambda_g/4$ transmission lines (TLs) and compute its equivalent inductance and capacitance as follows [99]

$$L_1 = \frac{2Z_0}{2\pi f_0} \tan\left(\frac{\theta}{2}\right) \tag{5.4}$$

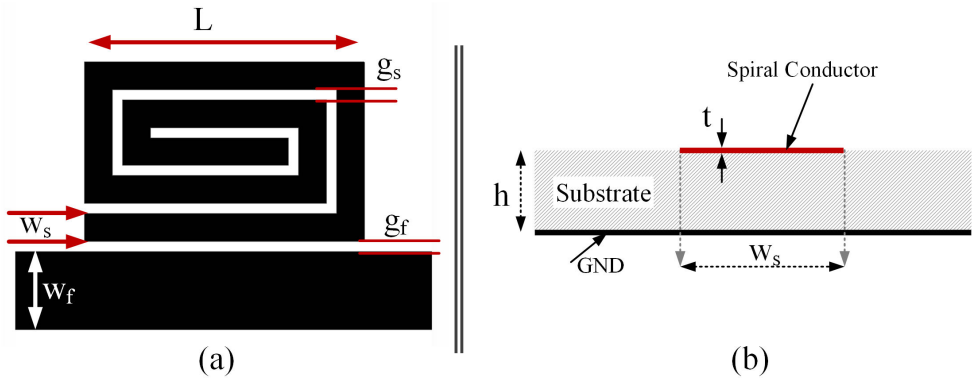

Figure 5.2: Spiral resonator model (a) dimensions, and (b) side view.

$$C_1 = \frac{1}{(2\pi f_0)(2Z_0)} \tan\left(\frac{\theta}{2}\right) \tag{5.5}$$

where Z_0 is the characteristic impedance of the TL of electrical length θ at the frequency f_0. When $\theta = \lambda_g/4$, (5.4) and (5.5) simplify, allowing L_1 and C_1 to be easily computed using

$$L_1 = \frac{2Z_0}{2\pi f_0} \tag{5.6}$$

$$C_1 = \frac{1}{(2\pi f_0)(2Z_0)} \tag{5.7}$$

5.1.3 Coupling Capacitance Based on Asymmetrical Coupled Transmission Lines Model:

As shown in Figure 5.3, the coupled capacitance between the 50Ω TL and RSRR can be expressed as two parallel capacitors, C_{ga} and C_{gd}, which represent the coupled field lines in air and dielectric respectively [76, 100]. Please refer to [100] for a full analysis of the microstrip transmission line.

First, the air gap capacitance C_{ga} can be defined as

$$C_{ga} = 0.5\ C_{cps-air} \tag{5.8}$$

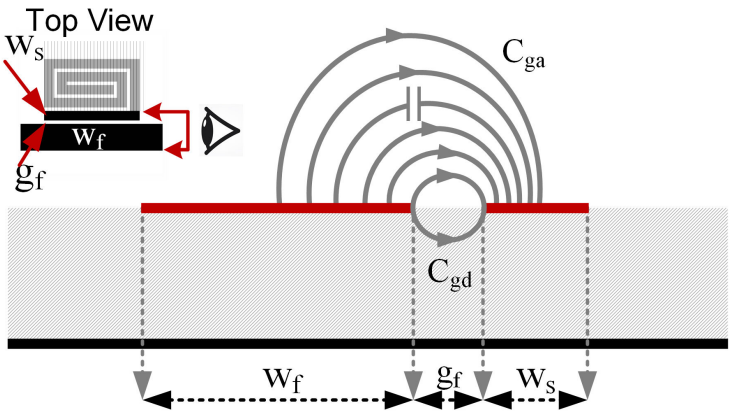

Figure 5.3: Asymmetric coupled microstrip lines' capacitances with the fringing fields and the ground capacitances ignored [100]

where $C_{cps-air}$ represents the field capacitance in the air for the asymmetrical coplanar strips and is given by

$$C_{cps_{air}} = \varepsilon_0 \varepsilon_{r_{air}} \frac{\kappa(k^{'})}{\kappa(k)} \tag{5.9}$$

with

$$k^2 = \frac{1 + W_f/g_f + W_s/g_f}{(1 + W_f/g_f)\,(1 + W_s/g_f)} \tag{5.10}$$

and

$$k^{'2} = 1 - k^2 \tag{5.11}$$

where g_f, W_f, and W_s represent the gap between the two lines, and the widths of the feed and spiral lines respectively. The ratio of the elliptic functions $\frac{\kappa(k^{'})}{\kappa(k)}$ is given by

$$\frac{\kappa(k^{'})}{\kappa(k)} = \begin{cases} \frac{1}{\pi}\ln\left(2\frac{1+\sqrt{k^{'}}}{1-\sqrt{k^{'}}}\right) & \text{for } 0 \le k^2 \le 0.5 \\ \ln\left(2\frac{1+\sqrt{k}}{1-\sqrt{k}}\right) & \text{for } 0.5 \le k^2 \le 1.0 \end{cases} \tag{5.12}$$

Secondly, the coupling capacitance between the two lines inside the dielectric material is given by

$$C_{gd} = \sqrt{(C_{gdf} - C_{gds})} \tag{5.13}$$

and

$$C_{gdY} = 0.5(C_{oY} - C_{eY}) \tag{5.14}$$

where $Y = f$ for feedline, $Y = s$ for spiral line and

$$C_{XY} = \frac{1}{c_v 60\pi} \frac{\kappa(k_{XY})}{\kappa(k_{XY}{}')} \tag{5.15}$$

where $X = o$ for odd mode, $X = e$ for even mode and c_v is the light velocity in free space. Lastly, the elliptic function and its complement can be calculated as

$$k_{XY} = \begin{cases} \tanh\left(\frac{\pi}{4}\frac{W_Y}{h}\right) / \tanh\left(\frac{\pi}{4}\frac{S+W_Y}{h}\right) , & \text{odd mode} \\ \tanh\left(\frac{\pi}{4}\frac{W_Y}{h}\right) \tanh\left(\frac{\pi}{4}\frac{S+W_Y}{h}\right) , & \text{even mode} \end{cases} \tag{5.16}$$

and $K_{XY}{}'$ can be calculated using (5.11).

$$k'_{XY}{}^2 = 1 - k_{XY}{}^2 \tag{5.17}$$

We developed a MATLAB^{TM} code to calculate C_{ga} and C_{gd} using (5.8)-(5.17). The equivalent total coupling capacitance will be the parallel combination of the two capacitances and C_c can be given as

$$C_c = C_{ga} + C_{gd} \tag{5.18}$$

Table 5.1 shows the design values used in the calculations and the resulting capacitance values. Figure 5.4 presents the circuit model of the RSRR and coupled TL.

Using the resonator models (ideal and non-ideal models) shown in Figure 5.4 and the calculated coupling capacitor value of 0.05pF, we achieved a well-matched resonance frequency compared to the simulated resonator as shown in Figure 5.5. There

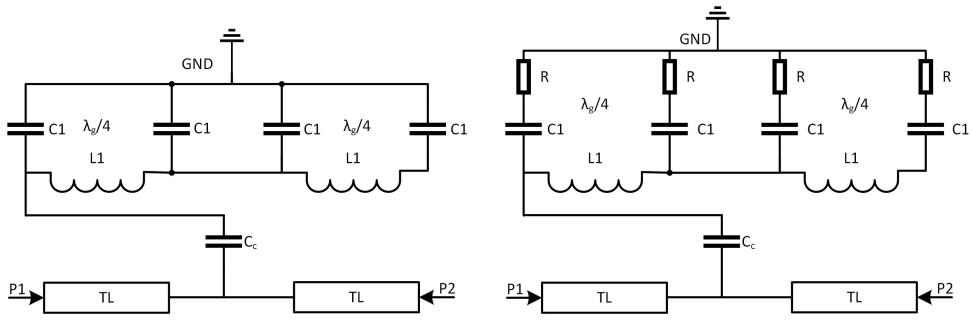

Figure 5.4: The circuit model of the half-wavelength spiral resonator where at 2.6 GHz, $C_1 = 0.3pF$, $L_1 = 11.5nH$, and $C_c = 0.05pF$ for ideal (lossless) model in (a), and non-ideal model (lossy) in (b) with $R = .25\ \Omega$

Table 5.1: Dimensions and Variables used in the Simulation model and MATLAB Code.

Param.	Value	Unit	Param.	Value	Unit
Z_0	50	Ω	C_{ga}	5×10^{-12}	F/m
f_0	2.6	GHz	C_{gd}	1.8×10^{-12}	F/m
W_s	0.8	mm	C_c	0.05	pF
W_f	2.26	mm	C_1	0.3	pF
g_f	0.3	mm	L_1	11.5	nH

is a slight variance in the two results due to imperfection of the etching process, de-embedding of the connectors, and the degree of uncertainty for the dielectric constant of the substrate. In Figure 5.4(b), a resistance R was used to model these losses which achieved a better match with the simulated and fabricated results. The sensor was built on a Rogers high-frequency laminate, RT/duroid 5880, with dielectric constant $\varepsilon_r = 2.2$, and loss tangent $\tan\delta = 0.0009$. The thickness of the substrate and copper cladding were 0.8mm and 35μm, respectively.

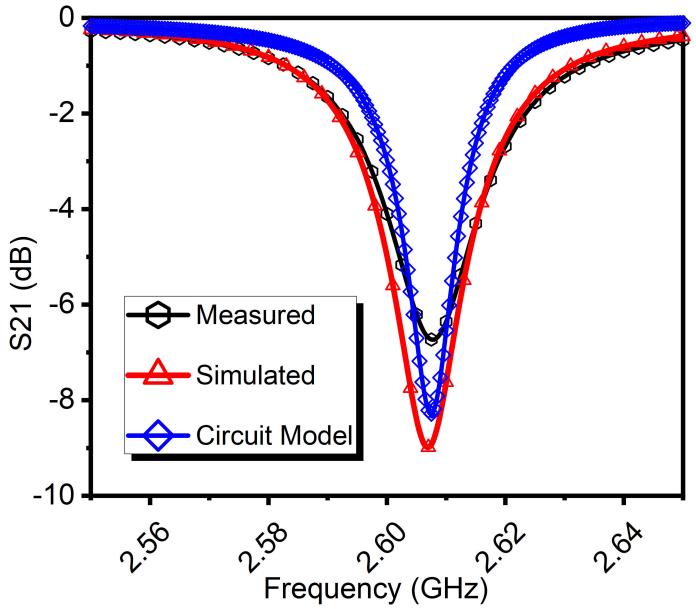

Figure 5.5: Comparison between spiral resonator frequency profiles for measured, simulated, and non-ideal circuit models.

To fabricate the RSRR as shown in Figure 5.2, the dimensions were optimized to operate at 2.57 GHz. A conventional etching process using 410 Ammonium Persulfate from MG Chemicals was used to pattern the copper. Figure 5.6(a) shows well-etched copper traces with gaps as small as 0.3 mm, and Figure 5.6(b) shows the fabricated two-port RSRR and coupled TL. The simulation model was designed and optimized using High Frequency Structural Simulator, HFSS®.

To evaluate the sensing capability of the single resonator surface area and its impacts on the resonance frequency, a substrate sample (Rogers RO3003 with $\varepsilon_r = 3$,

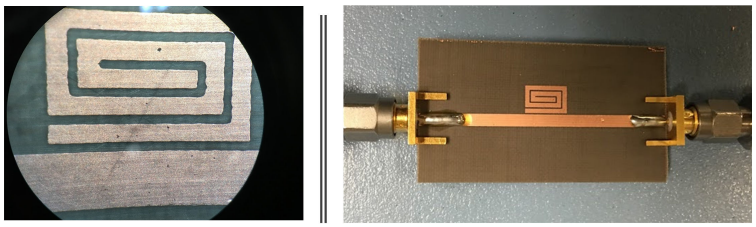

(a) (b)

Figure 5.6: Fabricated spiral resonator (a) close-up view emphasizing etching, and (b) fabricated design with connectors.

tanδ = 0.001, and thickness t = 0.51 mm) was held on top of the resonator covered different fractions of its surface as shown in Figure 5.7. The resonant frequency (f_r) of the spiral resonator coupled to a microstrip can be calculated by [74, 101, 102]

$$f_r = \frac{1}{2\pi\sqrt{C_e L_e}} \tag{5.19}$$

where C_e and L_e are the equivalent capacitance and inductance of the resonator, respectively. On the other hand, the frequency of an electromagnetic (EM) wave travelling in a medium of relative permittivity $\varepsilon_{r_{eff}}$ can be found by

$$f_r = \frac{\upsilon}{\lambda_g} = \frac{c/\sqrt{\varepsilon_{r_{eff}}}}{\lambda_g} \tag{5.20}$$

where υ is the speed of the EM wave in the medium and c is the speed of light in the free space (3×10^8 m/s) and λ_g is the guided wavelength of the EM wave in the material. From (5.19) and (5.20), the spiral resonance frequency vary with the change in the effective dielectric permittivity $\varepsilon_{r_{eff}}$ which accordingly affect the equivalent capacitance (C_e) and inductance (L_e) of the resonator. The described mathematic trend agrees with the measured results shown in Figure 5.8.

5.2 Sensor Resonator-Based Array Design

The spiral resonator above creates a stopband at its resonance when coupled to the transmission line as shown in Figure 5.5. Cascading the resonators along the trans-

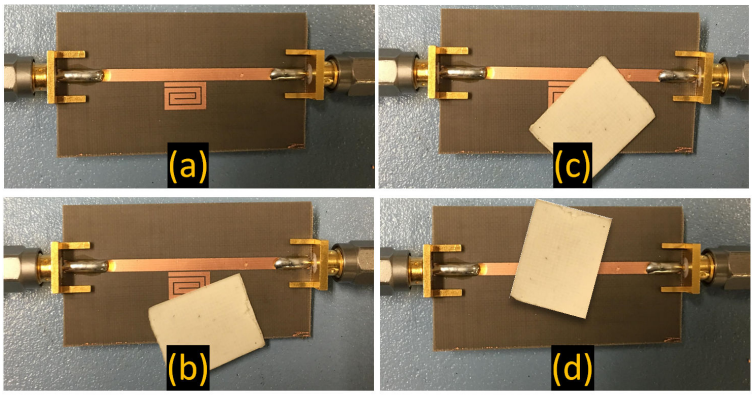

Figure 5.7: The fabricated resonator with the sample covering parts of the sensor.

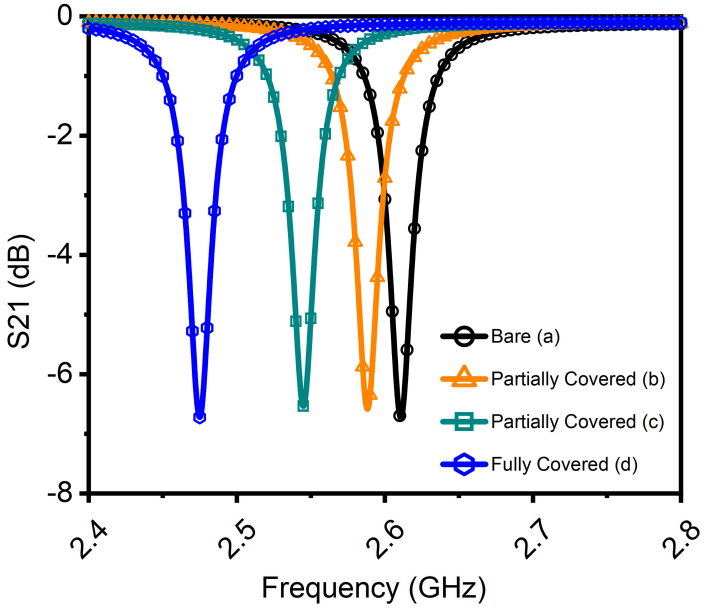

Figure 5.8: Measured results of the single sensor at different stages of sample coverage.

mission line, as shown in Figure 5.10, will create a stopband filter of the n^{th} order [76]. In addition, the more cascaded resonators, the higher the stopband rejection amplitude. To show the effect of the distance between the sensor elements, a simulation model of 2-element array as shown in Figure 5.9 was created and a parametric study was conducted. It shows that the distance between sensors has a slight effect on both parameters (resonance frequency and the fractional bandwidth (FBW)) as long as no direct coupling occur between adjacent sensors. It can be concluded that such sensor design provides flexibly in real applications to optimize between the preferred resolution and cost.

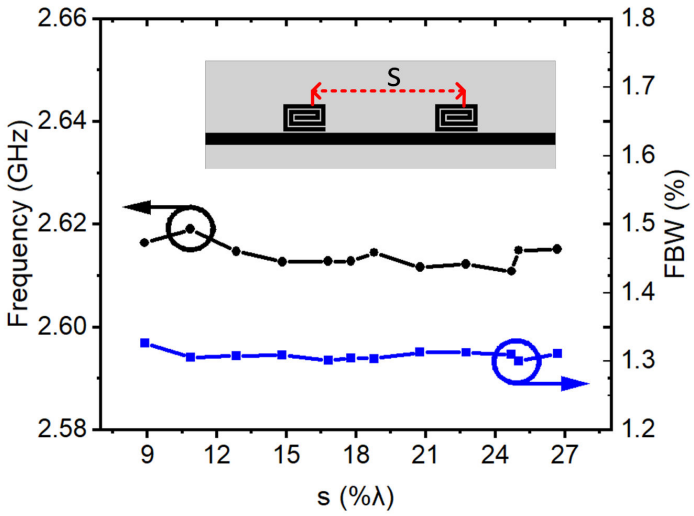

Figure 5.9: Simulated results for 2-element sensor array showing change of the resonance frequency and FBW versus the distance between the sensors (S).

An array of resonators was cascaded as shown in Figure 5.10. The distance between each sensor is 1.5 cm, built on the same substrate as of the single sensor in section 5.1.

The simulation results showing the responses for different array sizes are depicted in Figure 5.11 and Figure 5.12. The results clearly show the effect of cascading the resonators in an array, where the FBW and the magnitude of the rejection amplitude both increase with more cascaded resonators. Additionally, a shift in center frequency

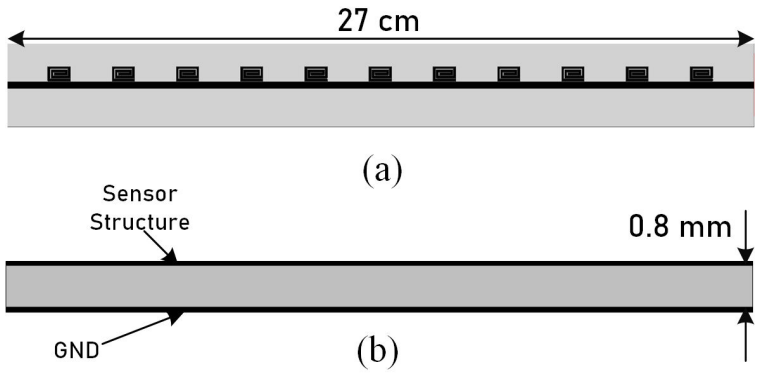

Figure 5.10: A sensor array of 11-elements (a) top view, and (b) side view showing the different layers of the system.

occurred when more resonators were cascaded. We believe this was due to loading effects of individual resonators on each other [78]. The changes in FBW and the pass/stopband amplitudes are summarized in Table 5.2.

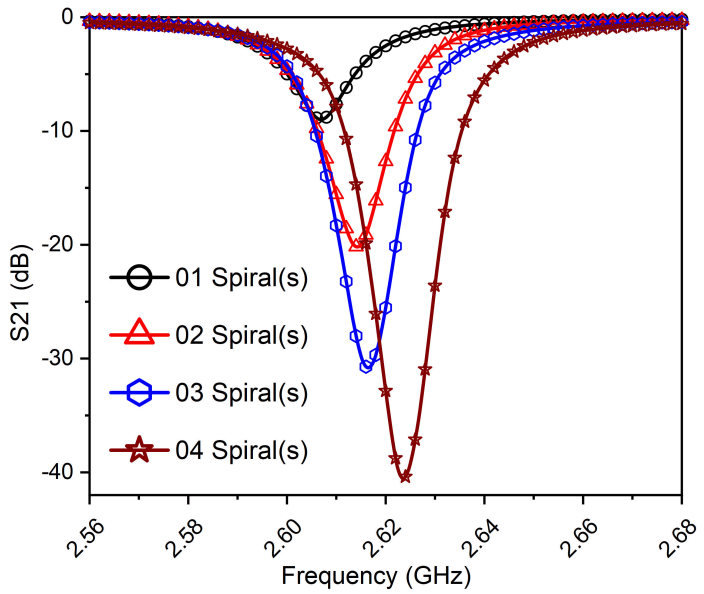

Figure 5.11: Simulated transmission coefficient S21 (in dB) for different array sizes (1,2,3, and 4 elements).

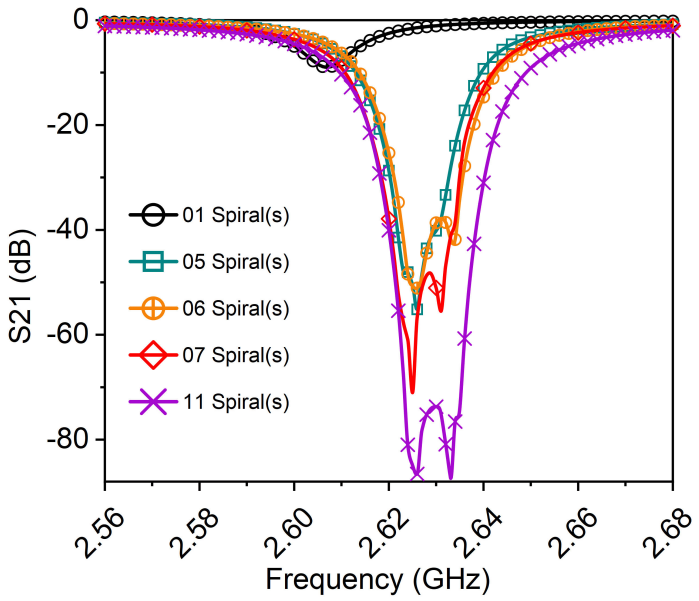

Figure 5.12: Simulated transmission coefficient S21 (in dB) for different array sizes (1, 5, 6, 7, and 11 elements).

Table 5.2: Center Frequency and the FBW for the Cascaded Resonators.

#	f_1 (GHz)	f_2 (GHz)	f_0 (GHz)	FBW (%)	Max. Amp. (dB)	Rej. Amp. (dB)
1	2.607	2.6294	2.60688	0.85927	-0.0472	-9
2	2.614	2.6478	2.61315	1.29346	-0.075	-20
3	2.616	2.6542	2.61633	1.46006	-0.0805	-31
4	2.624	2.6681	2.62351	1.67714	-0.1222	-40
5	2.626	2.6745	2.62624	1.84675	-0.1209	-55
6	2.628	2.6801	2.62802	1.99009	-0.1579	-54
7	2.626	2.6832	2.62624	2.17802	-0.1516	-71
11	2.630	2.7008	2.62986	2.69216	-0.3467	-87

5.3 Theoretical Analysis & Proof of Concept

In this section, we design and test the sensor in the form of an array. We investigate increasing the number of elements and discuss the performance. An nth order notch filter-based sensor can be represented by the equivalent circuit shown in Figure 5.13 for shunt-series topology. For identical resonators (e.g. $L_1 = L_2 = \cdots = L_n = L$ & $C_1 = C_2 = \cdots = C_n = C$), all resonance branches will have the same resonance condition that results in a unique rejection band. To illustrate the concept, arbitrary values for L and C are chosen and tuned to create a lossless notch at 2.6 GHz, resulting in $L = 29.19$ nH and $C = 0.13$ pF and utilizing the equivalent circuit model shown in Figure 5.13. Figure 5.14 shows a comparison between 1^{st} and 5^{th} order filter responses for an ideal sensor array (without any resistive loss). A unique resonance frequency is observed but exhibits change in FBW as a result of cascaded resonators.

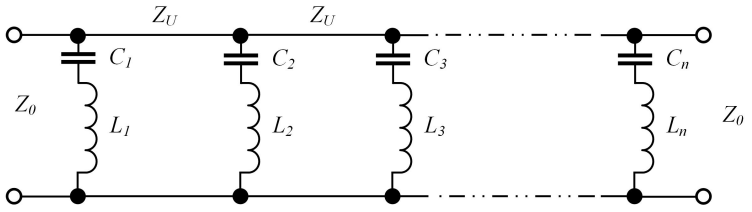

Figure 5.13: N^{th} order bandstop filter (notch sensor) equivalent circuit for series-parallel resonant branches.

Given the results observed in Figure 5.14, one can expect that by changing L_i and C_i of a single resonant branch, a new resonance will be created out of the main rejection bandwidth. For example, by increasing/decreasing the 3^{rd} element equivalent inductance and capacitance by 10%, a new resonance will arise before(lower)/after(higher) the original resonance frequency ($f_0 = 2.6$ GHz) as shown in Figure 5.15.

Changing the inductance and capacitance of a single resonator can be exploited for the targeted application of coating defect detection. For example, coating delamination would decrease the effective permittivity ($\varepsilon_{r_{eff}} \downarrow$) of the sensor environment, hence decrease its capacitance ($C_e \downarrow$), resulting in a positive frequency shift ($f_r \uparrow$),

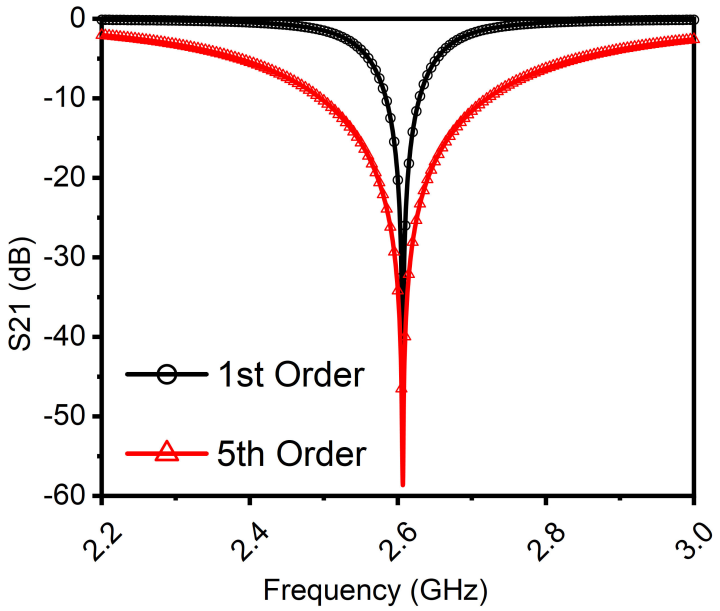

Figure 5.14: Simulated transmission coefficient S21 (in dB) for the notch sensor equivalent circuit shown above (1^{st} and 5^{th} order).

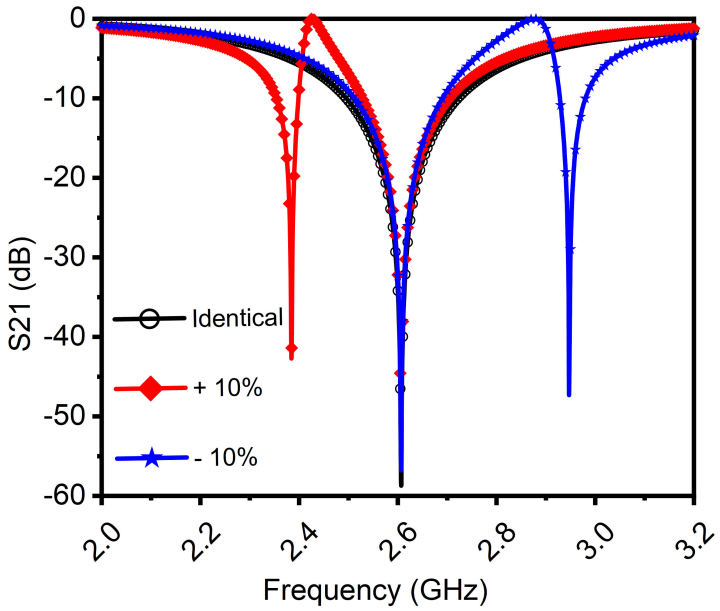

Figure 5.15: Simulated transmission coefficient S21 (in dB) for 5^{th} order filter when changing single element equivalent inductance and capacitance.

see (5.19) and (5.20). On the contrary, a water ingress below a coating would greatly increase the effective permittivity ($\varepsilon_{r_{eff}} \uparrow$) of the sensor environment, leading to an increase in capacitance ($C_e \uparrow$), thus negative frequency shift ($f_r \downarrow$). This premise of sensing, when combined with the previous discussion of creating different resonances, suggests that a sensor array is viable for effective prediction of coating defects over large surface areas.

An 11-element array was designed for use as a building block for initial testing in simulation, fabrication, and experiment. Firstly, we study the effects of perturbing the sensor surroundings by placing a sample (the same RO3003 used in previous section representing a defect) over individual sensors of the array. The cross-section exhibiting the different layers of arrangement is shown in Figure 5.16, where Layer Under Test (LUT) is the introduced film representing a defect.

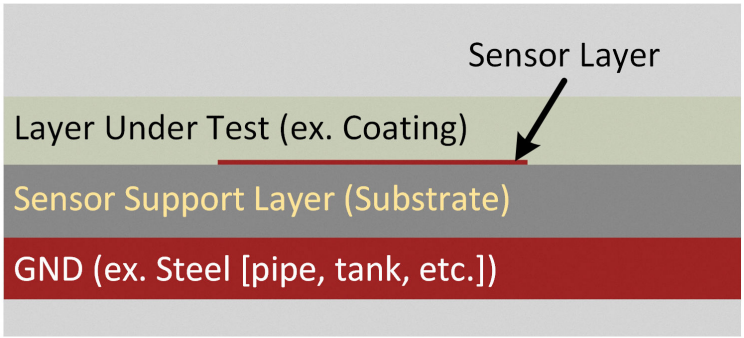

Figure 5.16: Side view of the layer under test added above the sensor layer,

The LUT is positioned on different sensing elements and at different locations as shown in Figure 5.17. The test sample changes the effective relative dielectric permittivity ($\varepsilon_r^{'}$) of the specific sensor, causing change to its original resonance frequency (f_0). A new resonance frequency ($f_0^{'}$) will arise due to the alteration, as shown in Figure 5.18. If two sensors have identical defect coverage (S4 and S7 in Figure 5.17(c)), the two created resonances will overlap as shown in Figure 5.18 case (c). However, considering different amounts of coverage (half of S4 and full S7 in Figure 5.17(d)), or non-identical defect shapes, two distinct resonances will occur as

shown in Figure 5.18 case (d).

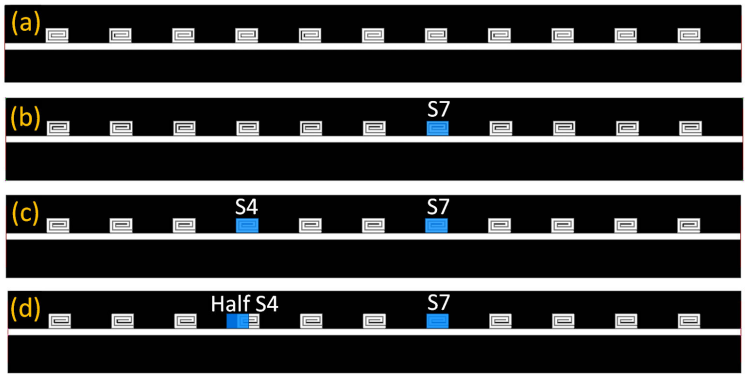

Figure 5.17: Test samples on different sensor locations in HFSS simulation.

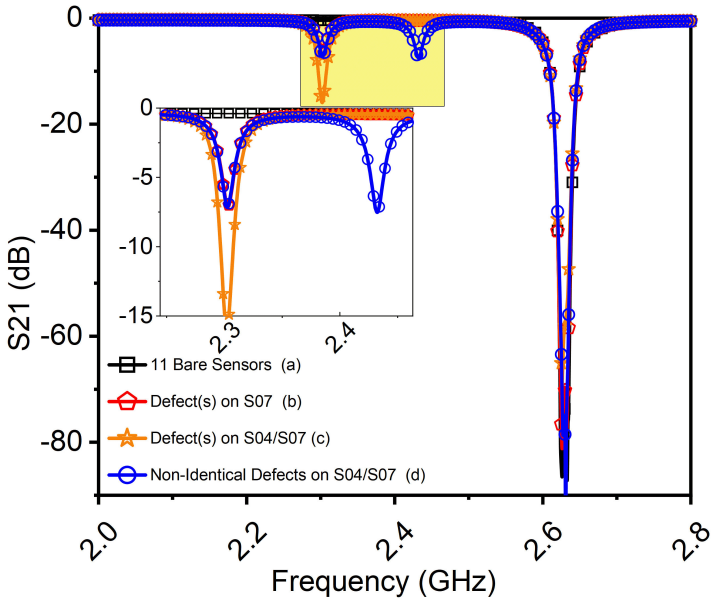

Figure 5.18: Simulated S21 (in dB) for 11-element array with defects shown/described above.

Figure 5.19 demonstrates the fabricated 11-element sensor array with identical resonators coupled (electromagnetically) to the transmission line. For experiment, test samples were distributed on different sensors to represent non-identical defects. A unique resonance at each resonator with defect can be observed in Figure 5.20, and the absolute value of the main resonance amplitude will decrease due to the newly-shaped stop bands. For example, when the test samples are distributed above

the sensors 1, 3, 5, and 9, four resonances are shown (blue plot with triangle-shaped symbol) at 2.264, 2.314, 2.393, and 2.513 GHz, respectively, while the original array resonance occurred at 2.639 GHz. In addition, each created resonance has an average amplitude of -7.2 dB (-8.13 dB @ 2.264 GHz, -6.72 dB @ 2.314 GHz, -7.54 dB @ 2.393 GHz, and -7.18 dB @ 2.513 GHz) at the center frequency. Through experimental verification, it is now clear that the occurrence of secondary frequency shift is an indication of permittivity change about a given element. It is also clear that when a resonator frequency is shifted, the rejection is reduced at the main resonance notch. Such behavior gives our system two degrees of freedom for the detection mechanism: frequency and amplitude changes.

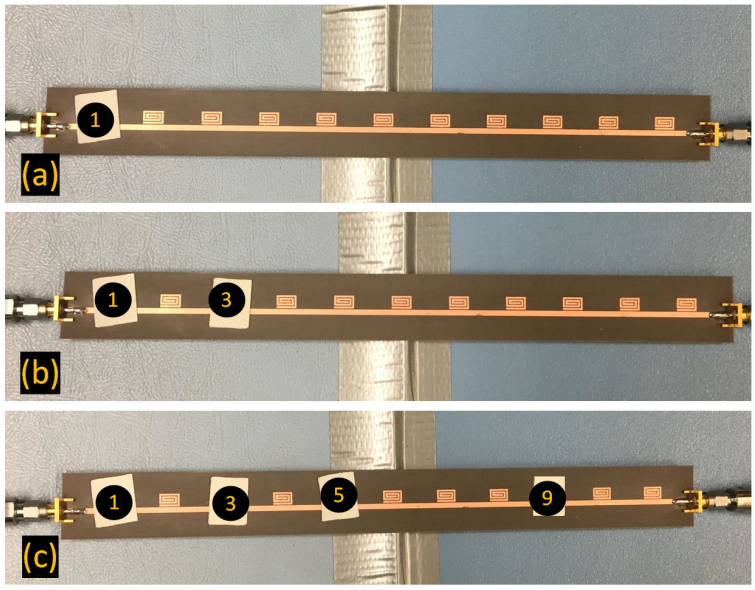

Figure 5.19: Measured S21 (in dB) for 11-element array with defects.

To extend the measurement range and area of coverage, we lengthened the array to 33-elements using three 11-element arrays. Using the previous experimental procedure of distributing the test sample on certain sensors, the measured frequency response of the 33-element array is shown in Figure 5.21. The figure shows the number of stopbands that appear in response to test samples at each sensor (sensors 5, 16, 25, 29) compared to the bare state with no defects.

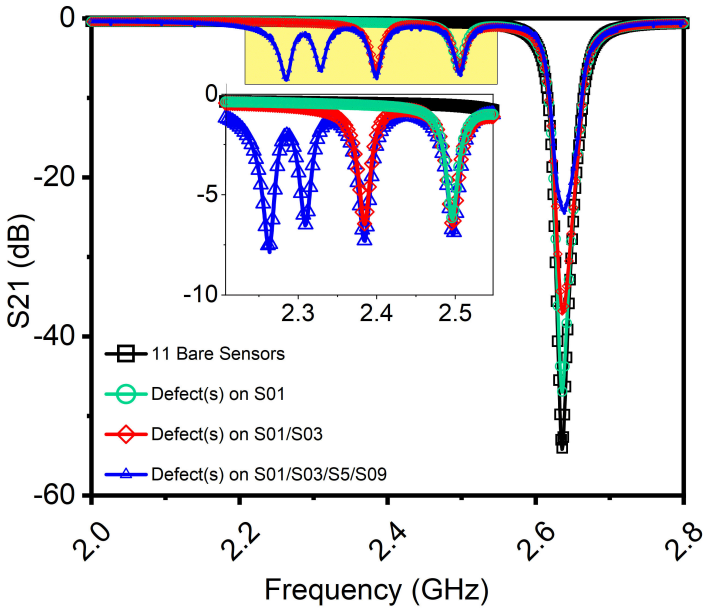

Figure 5.20: Measured S21 (in dB) for 11-element array with defects at different locations shown in 5.19

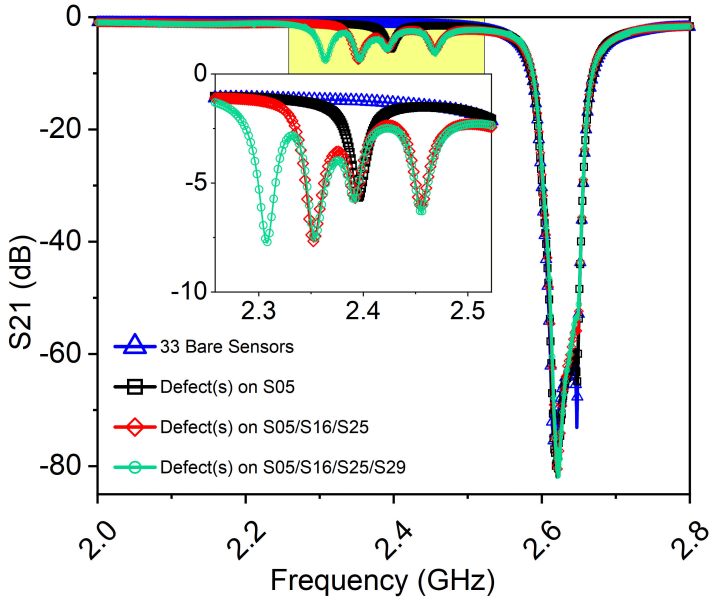

Figure 5.21: Measured S21 (in dB) for a 33-element array with defects.

As an indication of the performance comparison, different array sizes were compared, including a 44-element sensor array. The array frequency response is shown in Figure 5.22. As previously shown, including more cascaded elements deepens the stop-band amplitude.

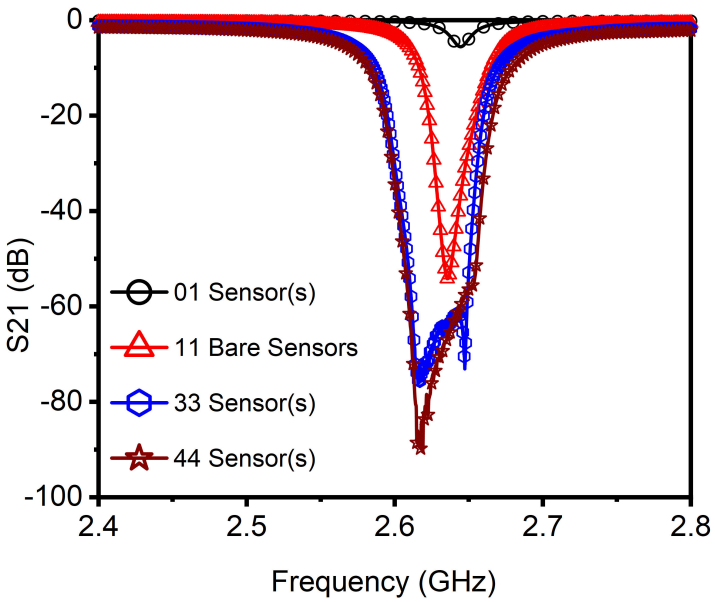

Figure 5.22: Measured transmission coefficient S21 for different array sizes: 11-, 33-, and 44-elements.

5.4 Integration of Long Sensor Array into Coating

When the proposed system is integrated with a real coating of steel structures, such as tanks, the most important defects to detect occur between the sensor and the steel surface. In other words, the defects between the sensor signal line and ground plane are representative of true problems. Therefore, this section focuses on the sensor response for an arrangement like that of shown in Figure 5.23. This time, the LUT is located between the sensor signal line and the ground plane.

To develop a test structure and confirm the sensor performance, we fabricated an array block on a very thin and flexi substrate. It utilized the same RT/duroid 5880 substrate as previous fabrications, but with 130μm thickness. The flexible design

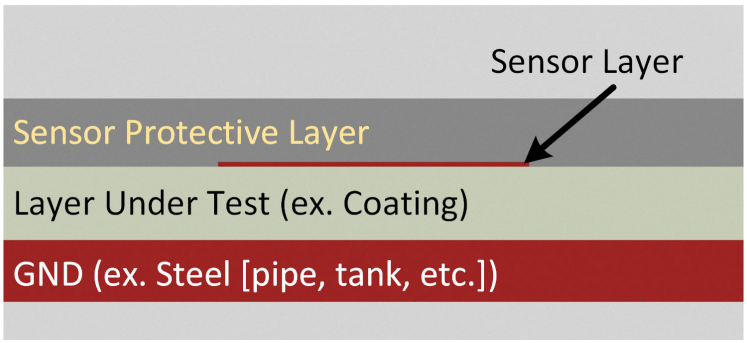

Figure 5.23: Side view of the LUT added above the sensor layer.

(flexi) was attached to the original substrate thickness of 0.8mm. Using two substrates allows for intentional introduction of moisture or water ingress, which will be explained in detail. First, the fabricated design was measured individually and then added to the 44-element array to make a 55-element array. Figure 5.24 shows the measurement before and after adding the flexi design to the extended array.

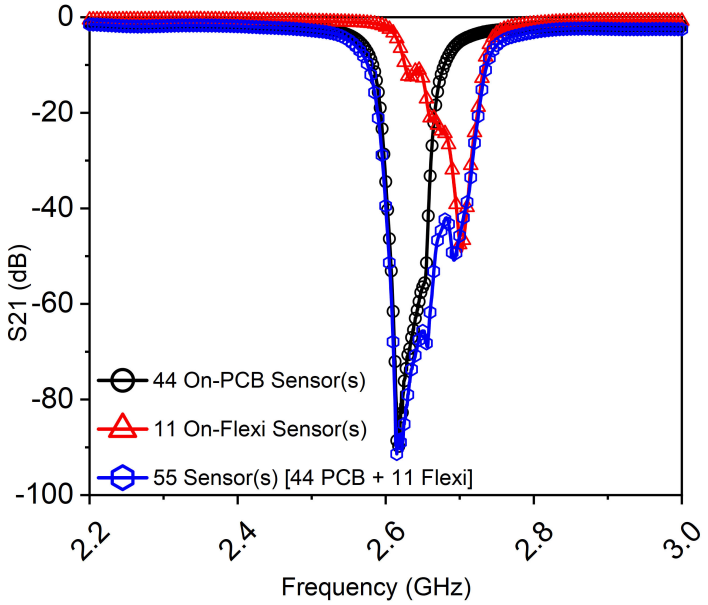

Figure 5.24: Adding the flexi array block to the extended 44-element array.

It is noticed in Figure 5.24 that the flexi substrate resonant frequency is slightly shifted due to the adhesive tape layer, which also generated air gaps, and the slight increase in overall substrate thickness. We made sure to be able to insert a *moisture*

test sample under each sensor for the proof-of-concept test. The measurement setup is shown in Figure 5.25 and exhibits the 55-element array. The figure inset shows the wet test samples inserted under the flexi array. A 4-Port C2420 VNA from Copper Mountain Technologies was used for the measurement.

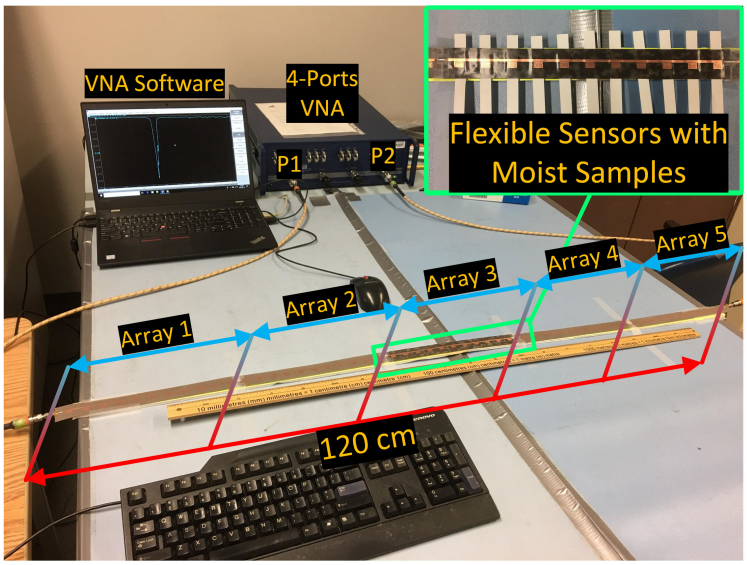

Figure 5.25: In-lab test setup is showing the long array connected to a VNA, with moist samples added to the flexi part.

A closer look at the flexi portion of the long array, and the process of adding and removing the moist samples, is shown in Figure 5.26. Each sensor has a thin paper inserted between the sensor and the ground plane substrate that has a dry part and wet part as shown in Figure 5.26(b,c). The sample is composed of a wet (in blue) and a dry (in yellow) portions. At first, the dry portion of the sample is inserted under a given sensor. By pulling the sample, the wet portion is transferred beneath the sensor, and the results are monitored and recorded.

To test the detection of water or moisture, individual sensors of the flexi array are tested. When inserting the wet part of the test sample below a sensor, a new resonance will occur at a lower frequency as shown in Figure 5.27 and Figure 5.28. We can notice two different aspects of the created stopband for the moist samples when compared to the test sample used above the sensors in section 5.3. First, the

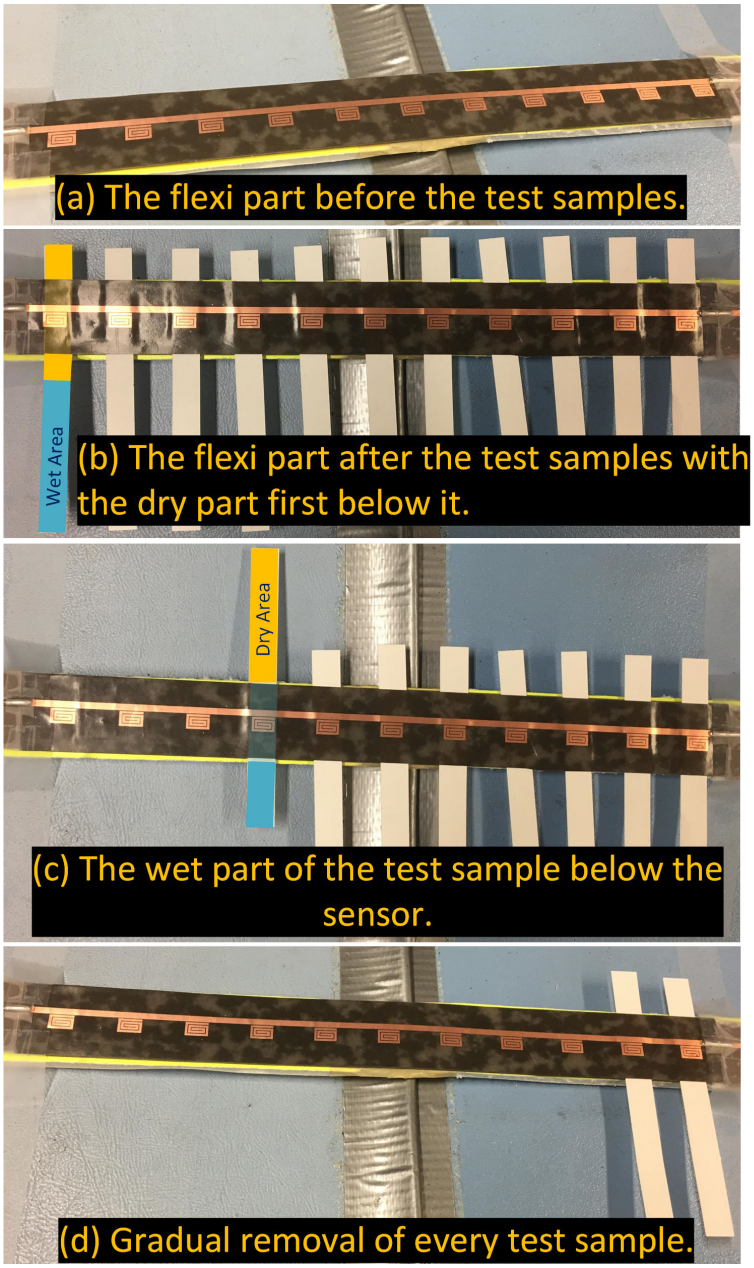

Figure 5.26: The test samples (wet and dry areas) added beneath the flexi array, tested, and finally removed.

created resonance happens at a lower frequency (around 2.0 GHz) than the substrate test sample (around 2.2 GHz) due to the immense difference in the dielectric constant value between both ($\approx$ 3.2 for the substrate sample and $\approx$ 80 for water at 20℃ [103]). This can be interpreted from the relation shown in (5.20) where the effective permittivity is increased. The second variance is associated with the difference in the losses between the two samples which reflects upon the 3dB BW of the created stopband (and as a result, the Q-Factor or the FBW). This can be clear by knowing the loss tangent of the substrate sample is $\tan\delta = 0.0018$ compared to $\tan\delta > 0.1$ for water [104].

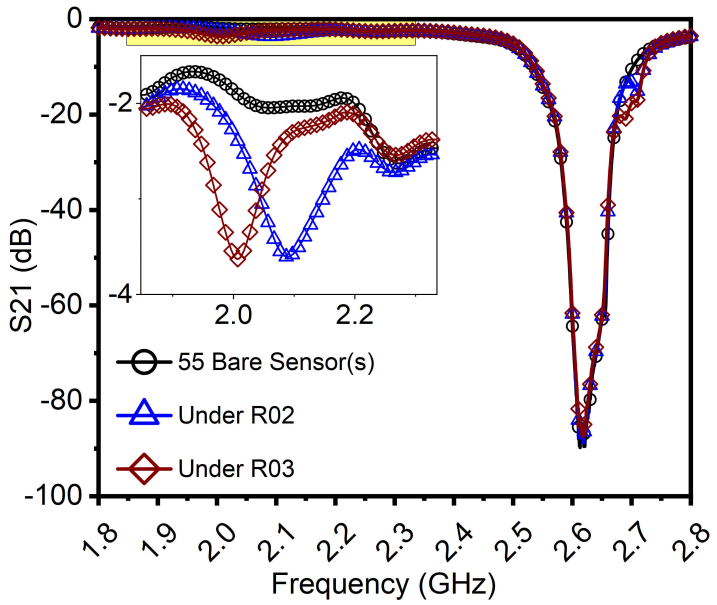

Figure 5.27: Measured S21 (in dB) when moist sample is inserted under the sensors.

Lastly, an air gap is created by lifting the sensor layer of the flexi block of the long array as shown in the inset of Figure 5.29, with results presented in Figure 5.29. As can be expected from (5.20), the effective permittivity is reduced, and a stopband will occur at a higher frequency than the main array resonance. This is an indication of coating delamination.

Comparing the results presented in Figure 5.27-5.29, it becomes evident that these sensors can selectively sense water ingress and coating delamination. As a result, by

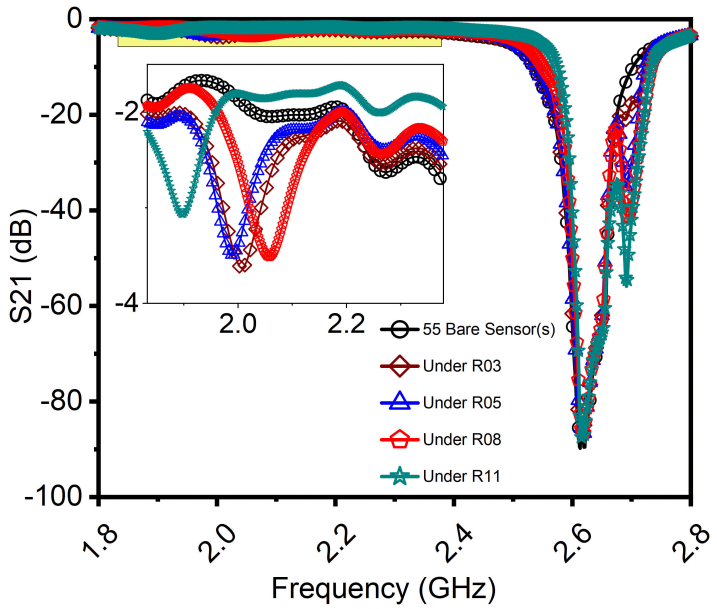

Figure 5.28: Measured S21 (in dB) when moist sample is inserted under the sensors.

distributing these sensor arrays using printing technologies, real-time monitoring can be available for sensitive structures such as the bottom of the oil storage tanks or long pipelines.

5.5 Summary

Unlike the sensor array introduced in Chapter 4 which is limited by the higher harmonics of the lower resonator's frequency, this chapter introduced an expandable array of identical resonators as innovative and repeatable technique for real-time coating defect detection on metallic structures. A prototype array composed of 55 identical rectangular spiral resonators coupled to a 120 cm long transmission line was explored. A stopband was created at the fundamental resonant frequency of the resonators. Any perturbation to the sensor environment (area of coverage) that changes the effective dielectric permittivity will lead to a generation of new frequency resonance. If the perturbation makes the permittivity higher, such as humidity or water ingress under the coating, a new resonance frequency will arise lower than the fundamental one. In contrast, for a coating lift-off or air gap created under the coating, a higher frequency

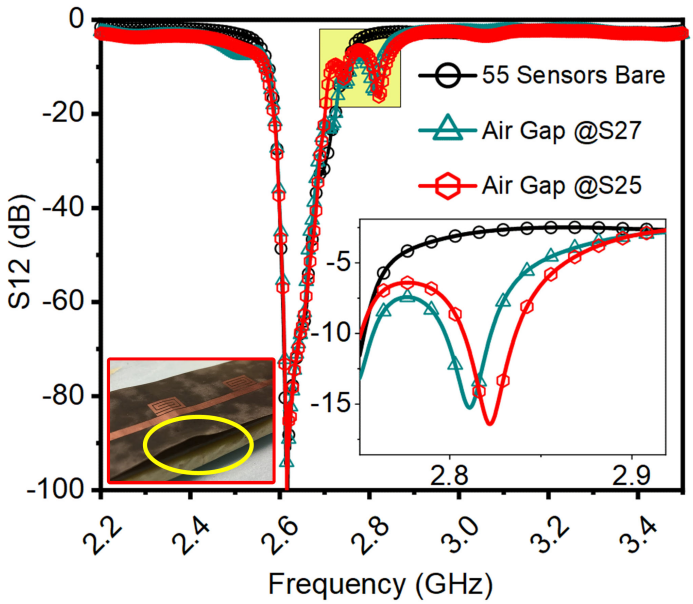

Figure 5.29: Measured S21 (in dB) when an air gap is created under the sensors.

will be created.

The developed concept in this chapter provides a massive scalability feature to cover very large surfaces while maintaining the detection notion simple and reliable. With the help of ink-jet printing and stamping technology, mass production of the proposed sensor can be a light addition to the manufacturing process makes it economically feasible. The high sensitivity of the sensor that can be responsive to an air-gap defect in a coating, put this technology as the first line-of-defense for maintaining the integrity of the targeted structures such as terminals and pipelines.

Chapter 6

Study of the Overlay Effect on Microwave Sensors for Coating Monitoring

The proposed sensors in the Chapter 4 and 5 will be stamped or printed on a coating layer of a metallic structure using a conductive material or ink [88]. In the field, this sensor layer will be covered by a protective layer, which also called *overlay*. Such layer is designed to minimize the interaction between the sensor and the exterior environment. Overlays play a critical role in designing microwave integrated circuits (MICs), antennas, and microwave-based sensors. They have been studied vastly for RF applications such as antenna gain enhancements [105], packaging of RF systems [106], and capacitive sensors coverage in touch sensors [107]. It has been shown that the choice of overlay material has a significant impact on the performance of the device.

Consequently, the need to study the sensor performance following the application of the overlay is paramount. In this chapter, the study of overlay effect on sensor system for coating monitoring is presented. Figure 6.1 exhibits an example of the overlay application. The study provides the recommended and optimized materials' properties to be used as an overlay from thickness to the dielectric permittivity. Measured results backed with simulation proof-of-concept results exhibit the validation of the proposed overlay properties to severely minimize the effect of the external

environment on such sensors. Dry and wet sand as external environmental effects were studied and showed that the sensors' immunity for certain overlay thickness to optimize reliability and cost for mass production.

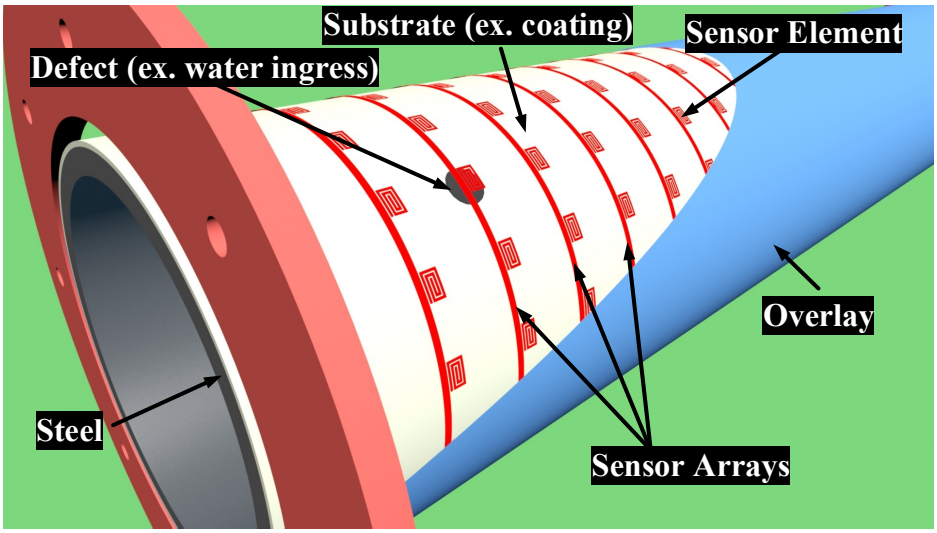

Figure 6.1: An application for the overlay on a chipless array used for coating monitoring.

This chapter is organized as follows. First, Section 6.1 outlines the principle of the operation for the embedded sensor and the necessity to apply the overlay layer in addition to the specifications of the sensor under test. The simulation setup and the analysis of the simulated results are then presented in Section 6.2. Section 6.3 exhibits the setup and the experimental materials used followed by the measured results and discussions. Final conclusions are presented in Section 6.4.

6.1 Proposed Principle for Embedded Sensors with Overlay

Utilization of a layer of an overlay to embed the sensor and confine the RF field such that external environment does not impact the sensor operation is introduced. This concept is visualized in Figure 6.1. The followings explain the sensor and its overlay design.

6.1.1 RF Sensor Specifications

A split-ring resonator sensor coupled to a microstrip line was chosen for its wider surface area, simple design and parameterization. The resonator was tuned around the 2.45 GHz ISM frequency band. As shown in Figure 6.2(a), the resonator dimensions are: the gap between arms $g_s = 0.3$ mm, the resonator line width $w_s = 0.8$ mm , the feed gap $g_f = 0.3$ mm, the 50 Ω transmission line width $w_f = 2.41$ mm, and the tuned length for 2.45 GHz $l = 8.65$ mm. Figure 6.2(b) shows the reflection coefficient (S11 in dB) of the resonator shown in (a). The resonator behaves as a stopband filter at its resonance.

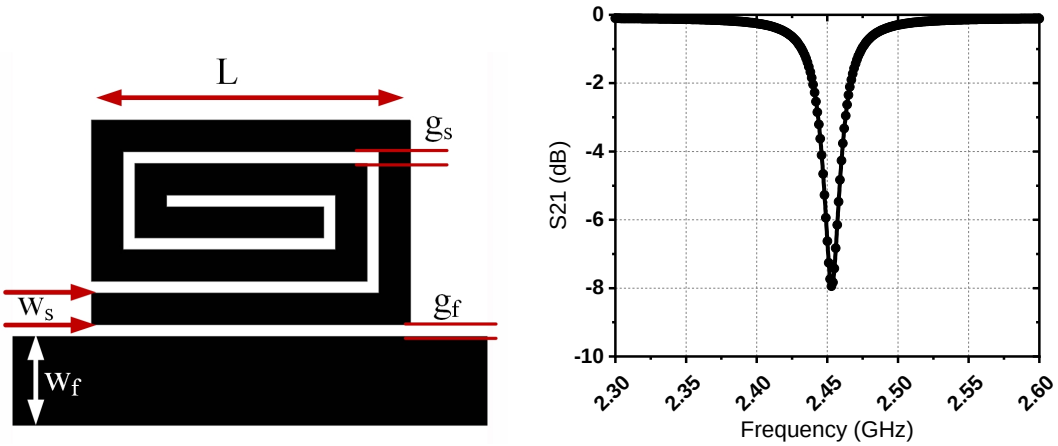

(a) (b)

Figure 6.2: Simulation model showing the spiral dimensions in a), and the frequency response in the form of Transmission Coefficient (S21) in b).

6.1.2 Coating and Overlay

The choice of the overlay material is such that it provides minimal impact on sensor performance. Since the targeted application for the sensor in this chapter is for coated-metallic structures, the sensor will be built on the coating where the metallic body acts as a GND plane as shown in Figure 6.1. The cross-sectional view of the intended application is shown in Figure 6.3. For lab-test, the sensor was built on a substrate, which in fact represents the coating in the targeted use and called layer

under test in Figure 6.3. This coating layer will be manufactured on the pipe's steel body which is represented with GND plane in this prototype. On top of the sensor layer, the overlay layer will be coated to minimize the external environment impact, such as the soil or sand for buried pipelines.

The overlay layer should be chosen such that the entire E-field is contained in between the layer and eliminate any fringing field to the external environment. This concept allows reducing the environmental impact while maintaining the full functionality of the sensor. In other words, any defects on the coating impacts the resonant behaviour of the sensor while the external environment will not, eliminating false readout.

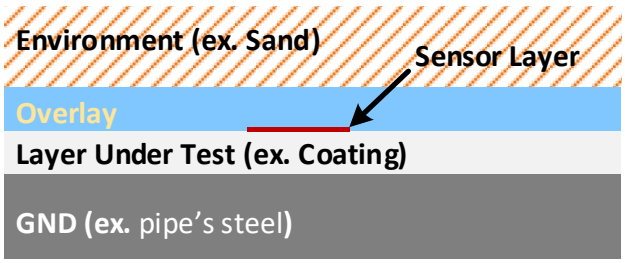

Figure 6.3: Layer stack for the potential application shown in Figure 6.1

6.2 Simulation Setup and Analysis

The 3D model of the simulation setup is shown below in Figure 6.4. The sensor substrate is chosen to be Arlon DiClad 880 with electrical properties of $\varepsilon_r = 2.2$, $tan\delta = 0.0009$, height $h = 0.79$ mm, and copper thickness of $t = 17.5$ μm. First, the sensor was covered by a material (overlay) with parameterized properties (dielectric constant $\varepsilon_{rOverlay}$ and height $h_{Overlay}$) as shown in Figure 6.4(b). Then, another material represents an external environment with parameterized properties (dielectric constant $\varepsilon_{rExt.Env.}$ and height $h_{Ext.Env.}$).

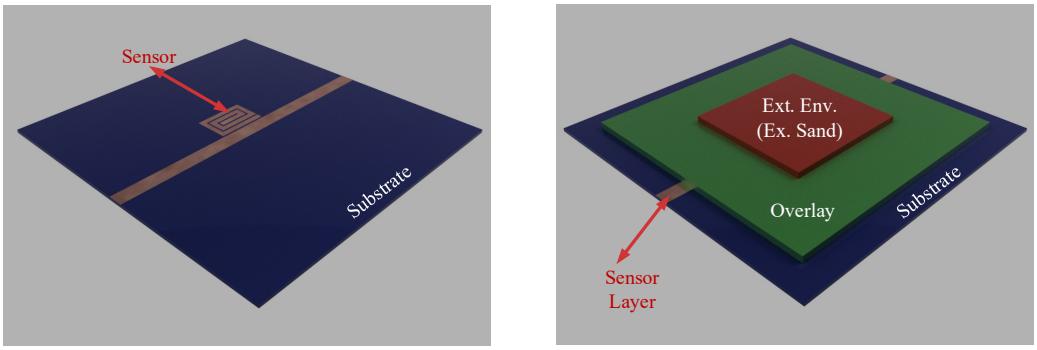

(a) (b)

Figure 6.4: The 3D model shows the overlay on top of the sensor layer in addition to another material represents the external environment effect.

There are two parameters to consider for the overlay material when the sensor is used for coating monitoring; the dielectric constant of the overlay and its thickness. For the thickness study, the goal is to find the optimized cover layer thickness needed to make the sensor layer invulnerable to its external surroundings. It would be rational to say the thicker, the better for such layer; however, it comes on the additional cost as well as the associated high profile and weight. Therefore, it is worth to optimize the layer thickness based on the parametric study. The simulation setup is shown in Figure 6.4(b) and the simulation results are shown in Figures 6.5 to 6.8 exhibits the relationship between the sensor's resonance frequency versus the dielectric constant of the external environment ($\varepsilon_{rExt.Env.}$) for different overlay materials ($\varepsilon_{rOverlay}$). The results in Figure 6.5(a) exhibits the change in resonance frequency of the sensor when changing $\varepsilon_{rExt.Env.}$ from 1.0 to 10.15 and for different $\varepsilon_{rOverlay}$ of 2.2, 4.5, 6.15, and 10.2 when $t_{Overlay} = 0.51$ mm. The selected values for both materials (thicknesses and dielectric constants) were to match the available commercial substrates that can be tested in the lab. On the other hand, Figure 6.5(b) illustrates alternative representation to the same data but with focusing on how much frequency shift occurs for each overlay material for each external environment material.

The trend follows in Figure 6.6, Figure 6.7, and Figure 6.8 for $t_{Overlay} = 1.02, 1.53,$

and 2.04 mm, respectively. The results show that, for lower dielectric permittivity of the overlay and the higher the dielectric constant of the external environment, the higher the resonance frequency shift (ex. ■ curve in Figure 6.5(a)). On the other hand, as the height of the overlay increases, the effect of external material diminishes, and the frequency shift becomes minimal (ex. ▼ curve in Figure 6.8(a)). It can be concluded that the external environment effect was minimized for $t_{Overlay} \geq 1.51$ mm.

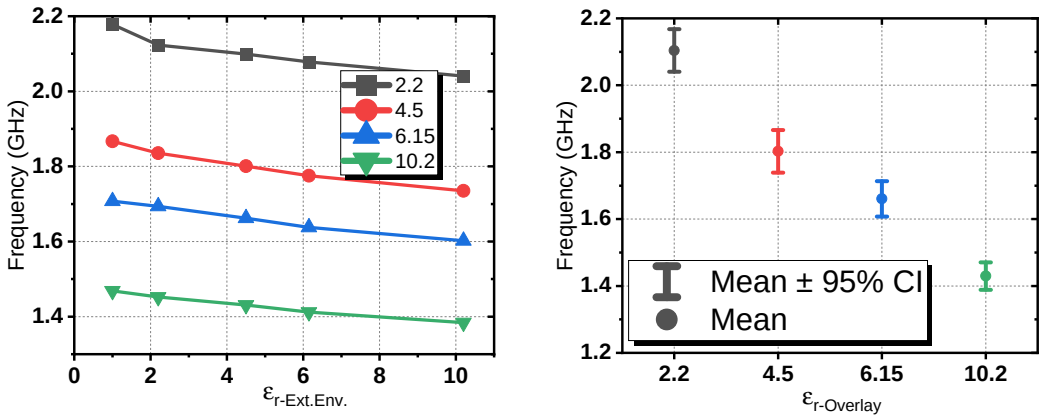

(a) (b)

Figure 6.5: The frequency change vs $\varepsilon_{rExt.Env.}$ for the different dielectric constant of $\varepsilon_{rOverlay} = 0.51$ mm in a) and vs $\varepsilon_{rOverlay}$ with confidence interval 95% in b).

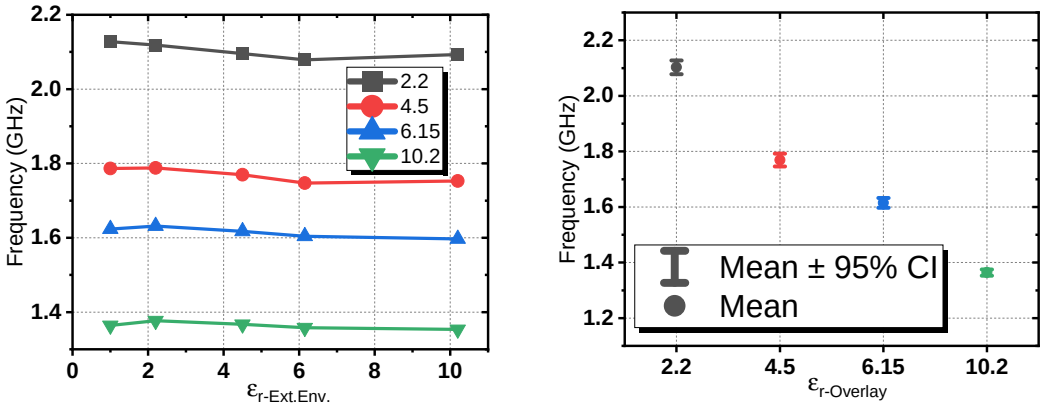

(a) (b)

Figure 6.6: The frequency change vs $\varepsilon_{rExt.Env.}$ for the different dielectric constant of $\varepsilon_{rOverlay} = 0.51$ mm in a) and vs $\varepsilon_{rOverlay}$ with confidence interval 95% in b).

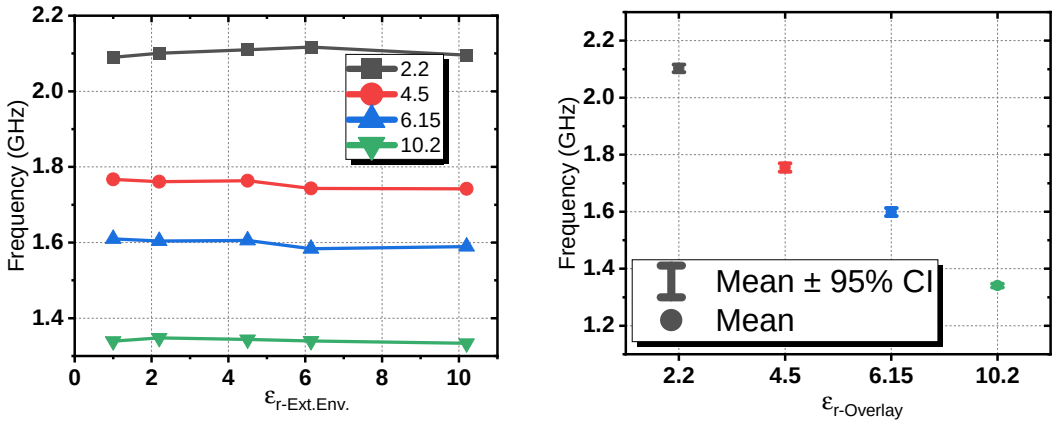

(a) (b)

Figure 6.7: The frequency change vs $\varepsilon_{rExt.Env.}$ for the different dielectric constant of $\varepsilon_{rOverlay} = 1.53$ mm in a) and vs $\varepsilon_{rOverlay}$ with confidence interval 95% in b).

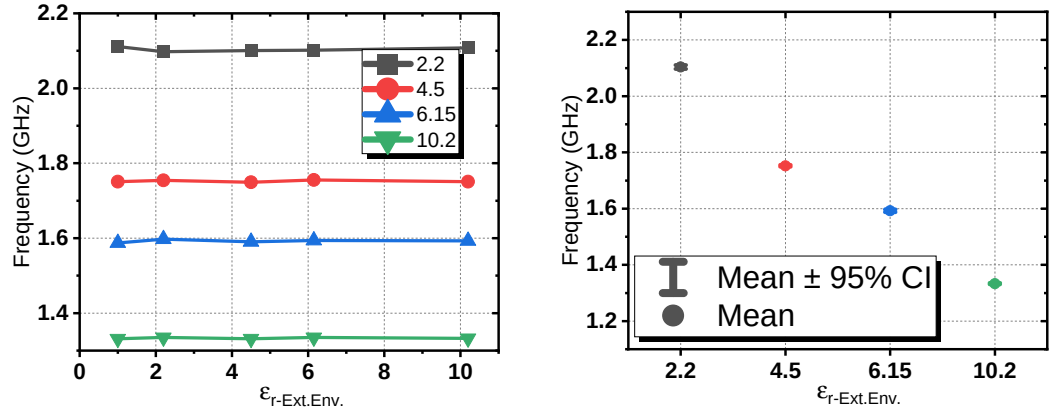

(a) (b)

Figure 6.8: The frequency change vs $\varepsilon_{rExt.Env.}$ for the different dielectric constant of $\varepsilon_{rOverlay} = 2.04$ mm in a) and vs $\varepsilon_{rOverlay}$ with confidence interval 95% in b).

6.3 Measured Results & Discussion

6.3.1 Setup & Experimental Materials Used

Figure 6.9 exhibits the in-lab structure for the experiment, which was conducted using the 4-port C2420 VNA from Copper Mountain. Different materials were used in the test as follow: MAT1) DiClad 880 with dielectric constant $\varepsilon_r = 2.2$, copper thickness $t = 35\mu$m, and loss tangent $tan\delta = 0.0009$, MAT2) TMM4 with $\varepsilon_r = 4.7$, $t = 35\mu$m, and $tan\delta = 0.002$, MAT3) AD1000L with $\varepsilon_r = 10.2$, $t = 35\mu$m, and $tan\delta = 0.0023$. The sensor was built on a substrate of MAT1 with a thickness of $t = 0.79$ mm using 410 Ammonium Persulfate conventional etching path.

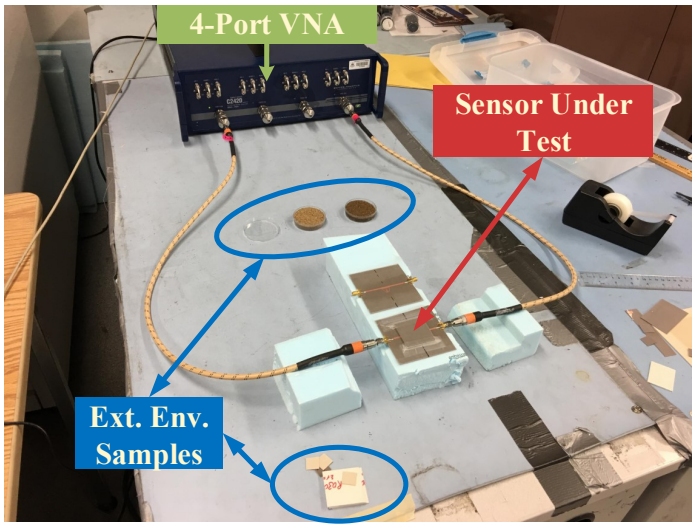

Figure 6.9: In-lab test setup shows the sensor and the materials used.

The materials arrangements are shown in Figure 6.10(a), (b). The overlay material was placed directly on top of the sensor layer. Figure 6.10(b) shows the dimensions for both the overlay and the external environment layers. One layer of the overlay material is 4 cm $\times$4 cm with a thickness of $h_{Overlay}$= 0.51 cm while a layer of the material that represents the external environment is 2cm $\times$2 cm with a thickness of $h_{Ext.\ Env.}$= 0.51 mm.

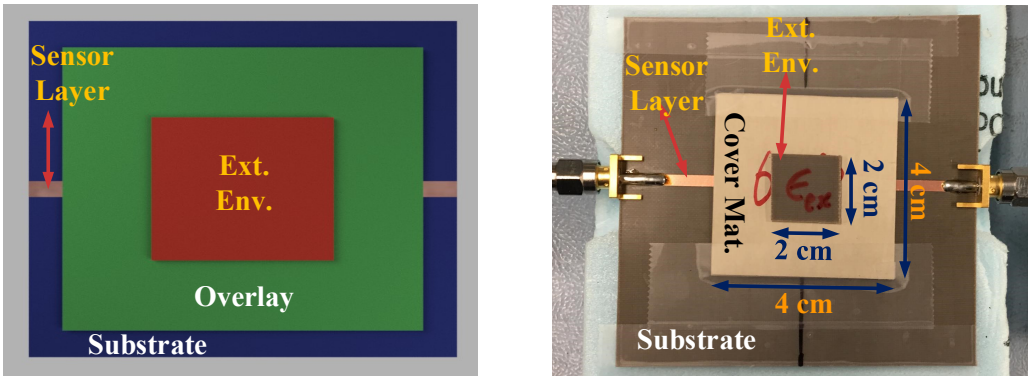

(a) (b)

Figure 6.10: 3D model shows the cover material on top of the sensor layer in addition to another material represents the external environment effect.

6.3.2 Measurement Procedure

Each material of the items mentioned in the previous section was used for both the overlay and the external environment layers. It started by placing one layer as an overlay and another layer of external environment layer on top of it, as mentioned in Section 6.2 and, as shown in Figure 6.10. The next step was to change the external material ($\varepsilon_{rExt.Env.}$) from MAT1 to MAT3 to have a gradual increase in the dielectric permittivity. Figure 6.11(a) exhibits the measured results for one overlay layer of MAT1 versus the dielectric permittivity of different types of $\varepsilon_{rExt.Env.}$ material. As shown, the frequency shifts reduces by increasing the material's dielectric permittivity (ε_{reff}) as expected from equation (6.1) [74]:

$$f_r = \frac{\upsilon}{\lambda_g} = \frac{c/\sqrt{\varepsilon_{reff}}}{\lambda_g} \tag{6.1}$$

where υ is the speed of the electromagnetic (EM) wave in the medium, c is the speed of light in the free space, and λ_g is the guided wavelength of the EM wave in the material.

In the same way, in Figure 6.11(b), two samples of sand (dry and water-saturated) as a real application for buried sensors for structure monitoring, such as pipeline sys-

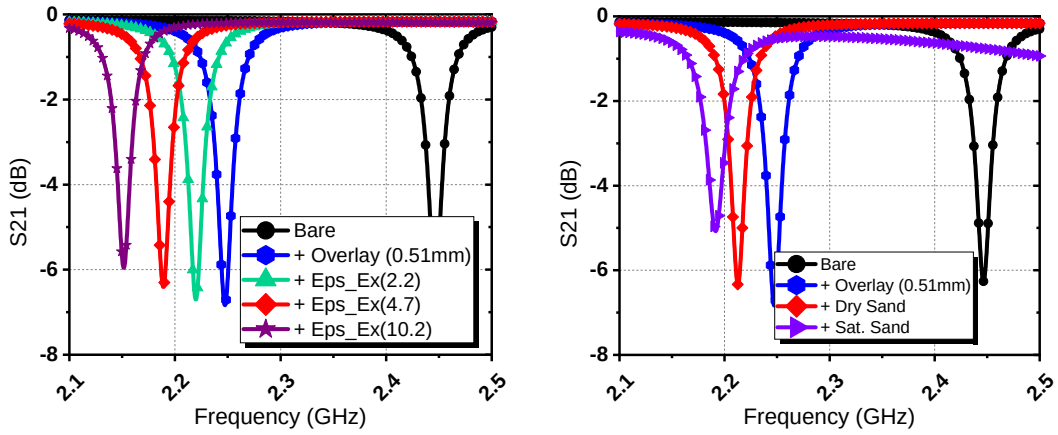

(a) (b)

Figure 6.11: Measured results for the effect of the external environment (legends) with the sensor covered by $h_{Overlay}$= 0.51 mm and $\varepsilon_{rOverlay} = 2.2$

tems [108]. A summary of the measured results for all combinations of the overlay and the $\varepsilon_{rExt.Env.}$ layers are shown in Figure 6.12 to Figure 6.14. As the $h_{Overlay}$ increases, the frequency shift decreases by increasing $\varepsilon_{rOverlay}$. For example, a frequency shift of 27.675 MHz occurred due to $\varepsilon_{rExt.Env.} = 2.2$ with overlay $\varepsilon_{rOverlay} = 2.2$ and $h_{Overlay}$= 0.51 mm, while it shifts 6.525 MHz when $h_{Overlay}$= 1.02 mm were used for the same $\varepsilon_{rExt.Env.}$. Likewise, a frequency shifts of 2.925 and 2.025 MHz occurred for $h_{Overlay}$= 1.53 and 2.04 mm, respectively.

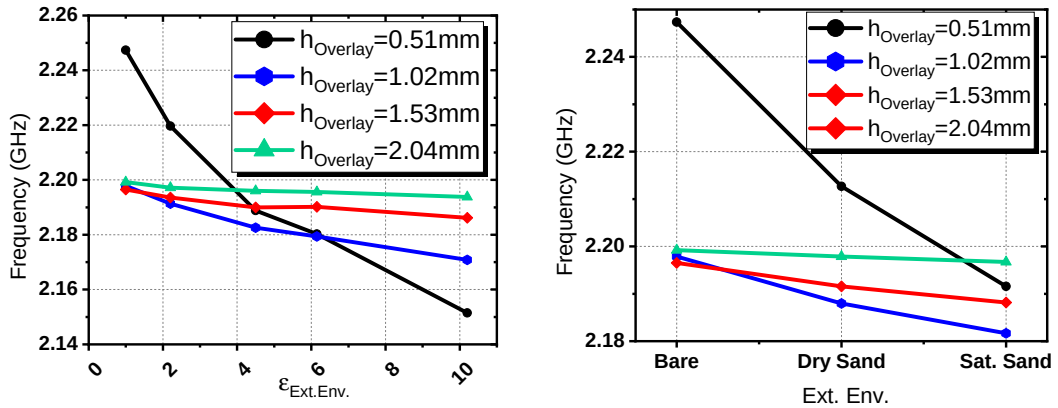

(a) (b)

Figure 6.12: Measured results for the effect of the overlay thickness ($\varepsilon_{rOverlay} = 2.2$) with the change of the external environment.

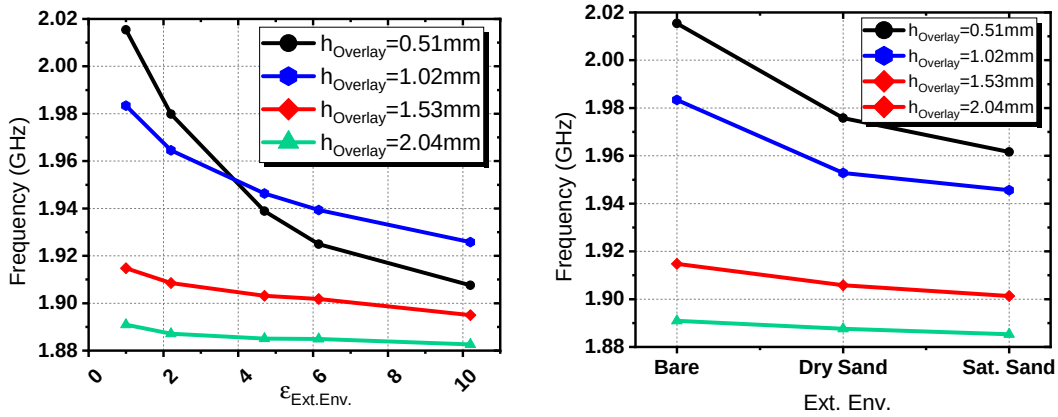

(a) (b)

Figure 6.13: Measured results for the effect of the overlay thickness ($\varepsilon_{rOverlay} = 4.5$) with the change of the external environment.

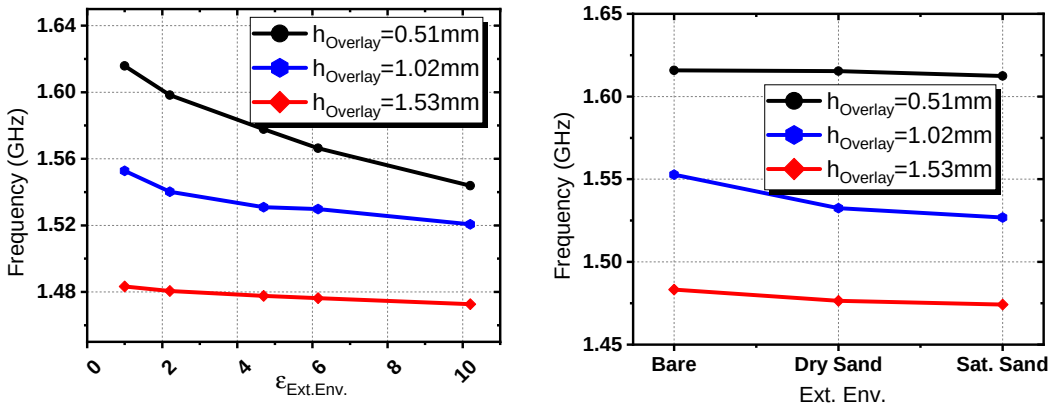

(a) (b)

Figure 6.14: Measured results for the effect of the overlay thickness ($\varepsilon_{rOverlay} = 10.2$) with the change of the external environment.

On the other hand, if $\varepsilon_{rOverlay}$ of MAT3 which has a higher dielectric permittivity, a frequency shifts of 95.85, 27, 10.35, and 5.4 MHz occurred for $h_{Overlay}$= 0.51, 1.01, 1.53 and 2.04 mm of MAT1, respectively. This concludes that the sensor with $h_{Overlay}$= 2.04 mm becomes less sensitive for $\varepsilon_{rExt.Env.}$ of MAT3 18 times (95.85/5.4) than $h_{Overlay}$= 0.51 mm.

For the sand test results, the same observation applies where dry sand produces 34.65, 9.9, 4.95, and 1.35 MHz of frequency shifts for $h_{Overlay}$= 0.51, 1.01, 1.53 and 2.04 mm of MAT1, respectively. Sensitivity reduction up to 26 times (34.65/1.35) was achieved for the dry sand. Similarly, the wet sand created shifts of 55.8, 16.2, 8.325, and 2.475 MHz for the same setup with a sensitivity reduction of around 23 times (55.8/2.475). As can be seen, compared to $h_{Overlay}$= 0.51 mm, a $h_{Overlay}$= 2.04 mm indicates a much lower frequency change and hence, little impact by the external environment.

6.4 Summary

A study of the overlay effect on sensor performance was conducted in this chapter. The thickness and the dielectric constant of the overlay material were used as the degrees-of-freedom to optimize such layer for better sensor performance as well as a cost-effective solution for mass production. The study suggested the reasonable characteristics for the overlay and how to minimize the environmental impact on the sensor implementation without degrading its sensitivity. The study outcome can be used as a reference for overlay design for embedded sensors, specifically, coating monitoring systems.

Chapter 7

Conclusion

7.1 Summary

The main goal of this thesis was to present a new platform for real-time coating monitoring using Chipless RFID technology. To fulfill this goal, two proposals for building sensor arrays were introduced, and their uses in a variety of structural monitoring scenarios such as pipelines and crude-oil storage tanks were explored.

First, in Chapter 3, an initial study was proposed as a proof-of-concept experiment using a battery-free LC-based sensor for pipeline integrity monitoring in a real-time fashion. The sensor monitors the coating lift-off from the pipeline, which is the initial step in the external corrosion of a metal pipe. However, only a localized coating problem could be detected.

The fully integrated wireless Chipless RFID system using a combination of an expandable resonator-based sensor array and patch-based tag antennas was presented in Chapter 4 for out-of-sight pipeline monitoring. Early signs of corrosion-prone areas can be detected by altering the root causes of the mechanism, such as water ingress or coating delamination. The system structure was a single-layer for easy integration within the coating layer using printing or stamping technologies such as ink-jet for economic mass-production.

To overcome the limitations on the array size presented by the higher harmonics in Chapter 4, we introduced a sensing concept in Chapter 5 to cover large surfaces and

long distances. The chapter introduced an expandable array of identical resonators for real-time coating defect detection on metallic structures. A 120 cm long array was constructed and experimented; however, backed with theory, the array is expandable, and the detection technique is straightforward and reliable.

Finally, and due to the need to protect the conductive sensor layer against the surrounding environment, the impact of an overlay was studied in Chapter 6. An optimization process for different overlay materials and thicknesses against various external effects was presented and discussed.

7.2 Contributions

The list of original accomplishments described in this thesis can be summarized as the following:

- The design, simulation, and experimentation of a chipless RFID LC-based sensor as the SHM technique for pipeline integrity monitoring is presented. The sensor resonance frequency exhibits a strong relation to coating delamination (gap) and water ingress as corrosion stimuli. The designed sensor is suitable for harsh environments in addition to being simple, battery-free, and conformal for easy installation and integration. The high-quality factor (115) and the maximum frequency shift (11.7%) make the sensor an accurate and reliable method to achieve a defect-free coated structure for applications such as pipelines.

- A wide-band inset-fed slotted patch-based antenna is presented to be integrated with a chipless RFID monitoring system. The antenna is designed to operate in proximity of metallic structures such as the steel structure of a pipeline. Besides, the antenna performance is validated for different pipe diameters to investigate the curvature effect on the antenna radiation as well as the impedance bandwidth. It showed that curvature of the pipe had minimal effect on the antenna performance.

- A fully integrated chipless RFID RSR-based sensor array for out-of-sight wireless pipeline monitoring is demonstrated. Each resonator in the array creates its frequency signature that responds reliably and repeatedly to coating defects such as water ingress. Two cross-polarized slotted patch antennas and two LP-DAs are used for tag and reader, respectively. The tag structure utilizes the pipe's steel structure for its ground (GND) plane. The designed sensor system is a planar and conductive single-layer intended to be stamped on top of the coating layer, providing a non-invasive, real-time, and easy-to-integrate SHM technique.

- An extendable resonator-based microwave sensor array for coating defect detection on large surfaces is presented. Relying on a single resonator to build the array provides the opportunity to massively enlarge the design length while keeping the detection mechanism simple and reliable. A prototype composed of a 55-element sensor array measured 120 cm length is designed, fabricated, and tested. Water ingress below coating, as well as air-gap (delamination), are reliably and repeatedly detected during the measurements. The array is a single layer; taking advantage of the metallic structure as a ground plane makes it easy-to-print/stamp on existing and new structures.

- A thorough investigation of the effect of a protection layer (overlay) for the designed chipless RFID SHM systems is presented. Different materials and thicknesses for the overlay are simulated and experimented. The study shows a trade-off between cost as a function of the material thickness and the sensor immunity to the effects of the surrounding external environment.

In conclusion, the study of this thesis has unveiled the practicability of having a proactive approach in SHM to predict defects instead of detecting them after the incident. The design and implementation of chipless RFID for real-time monitoring for coated-metallic structures have been developed, and its applications for pipelines and

terminals have been explored, achieving a prediction technique for defects compared to a detection approach as presently reported in the literature.

A potential future expansion of this work persists in a high degree for a more extended detection and communication range with broader bandwidth capabilities. The outcome of this thesis has provided a foundation of an SHM technique applicable in a stream of applications to achieve accident-free and zero false-alarm monitoring technology.

7.3 Future Considerations

The results detailed in this thesis have shown the enormous potential of the offered Chipless RFID-based monitoring system as a SHM technique for vital systems' integrity such as pipelines. Still, several key design elements and challenges remain for its successful field-implementation and manufacturing integration. Therefore, a list of potential future considerations is provided below.

- The resonator's higher harmonics constrains the array size of the non-identical resonators presented in Chapter 4. By introducing a spurious-free resonator, as shown in Figure 7.1, the array can be expandable to cover larger surfaces and provide higher resolution.

- Research into the identification of the communication range limitations considering humidity, soil wetness, and type of soil/sand for buried pipelines should be investigated. In addition, utilizing ultra-wideband time-coded chipless RFID technique could improve the range dramatically [109, 110]. However, this could lead to a challenge in the tag antenna design, specifically in the metallic structure proximity. So, a trade-off has to be made to optimized the complexity and the read range needed.

- The high coupling between resonators and the transmission line plus the reasonable distance between consecutive resonators diminishes the mutual coupling

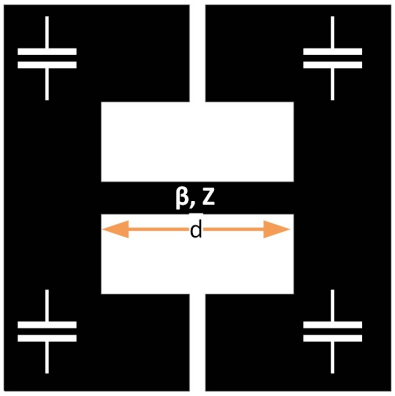

(a) SWR shows the loaded capacitances.

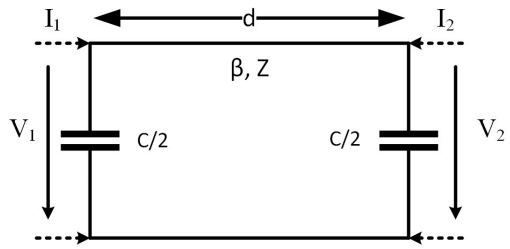

(b) Lumped circuit equivalent for SWR.

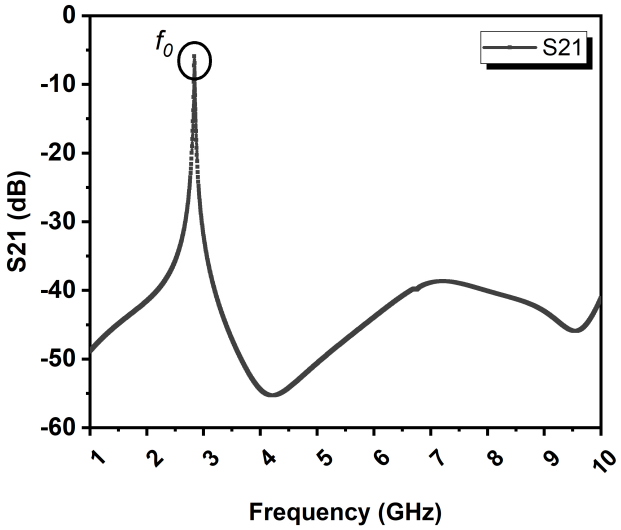

(c) Frequency response of the slow-wave resonator with wide non-spurious range.

Figure 7.1: SWR is a capacitively-loaded resonator to generate slow-wave behavior.

between them. In some applications, the resonators can be brought close to each other, maximizing the monitored area or the resolution. In this case, the study of inter-element coupling will be needed for full surface coverage.

- The concept presented in Chapter 5 for the expandable identical sensors' array is theoretically unlimited. However, it takes extensive resources (massive memory and CPU usage) to prove simulation and experimental trials for the long array. Relying on a lumped element or scattering parameters building blocks

in simulation won't reflect the real response. Innovative simulation and lab techniques to test longer arrays are needed.

- On the one hand, it is required to protect the sensors' conductive layer using the overlay. On the other hand, this layer should be invisible to the antennas for the best performance. The overlay optimization for sensors and antennas to work in proximity will be of much importance.

Thesis Publication List (as of April 2020)

This section lists the academic contributions made during the course of this doctoral thesis, including journal papers, conference papers, and patents.

Thesis-Related Publications

This section lists the refereed journals, patents, and conference papers published during the course of this thesis work which are directly related to the thesis objectives.

Journals

1. S. Deif and M. Daneshmand, "Long Array of Microwave Sensors for Real-Time Coating Defect Detection," *IEEE Trans. Microw. Theory Tech.*, 2020, doi: 10.1109/tmtt.2020.2973385.

2. S. Deif, S. Olokede, M. Nosrati, and M. Daneshmand, "Printed Concave-Like Slot for Bandwidth Enhancement of Inset-Fed Patch Antenna on Metallic Surfaces," *Microwave and Optical Technology Letters*, April 2020, doi:10.1002/mop.32438.

3. S. Olokede, S. Deif, , M. Nosrati, and M. Daneshmand, "Printed Concave-Like Slot for Bandwidth Enhancement of Inset-Fed Patch Antenna on Metallic Surfaces," *Microwave Journal* , **Under Review**.

4. S. Deif and M. Daneshmand, "Multi-Resonant Chipless RFID Array System for Coating Defect Detection and Corrosion Prediction," *IEEE Trans. Ind.*

Electron., 2019, doi: 10.1109/tie.2019.2949520.

5. M. H. Zarifi, S. Deif, et al., "A microwave ring resonator sensor for early detection of breaches in pipeline coatings," *IEEE Trans. Ind. Electron.*, vol. 65, no. 2, pp. 1626–1635, Feb. 2017.

6. M. H. Zarifi, S. Deif, and M. Daneshmand, "Wireless passive RFID sensor for pipeline integrity monitoring," *Sensors Actuators, A Phys.*, vol. 261, pp. 24–29, 2017.

Patents

1. M. Daneshmand, S. Deif, M. H. Zarifi, and N. Vahabisani; "Sensor system for pipeline integrity monitoring,", *20190293547*:A1 26-Sep-2019.

Conferences

1. S. Deif, B. Leier, M. Snow and M. Daneshmand; "Microwave Sensor Array for Corrosion Prediction in Steel Tank Bottoms," in *2018 12th International Pipeline Conference*, Calgary, Alberta, Canada, September 2018.

2. S. Deif, L. Harron, and M. Daneshmand; "Out-of-Sight Salt-Water Concentration Sensing Using Chipless- RFID for Pipeline Coating Integrity," in *2018 IEEE/MTT-S International Microwave Symposium - IMS*, Philadelphia, PA, USA, in June 2018.

3. S. Deif, M. H. Zarifi, and M. Daneshmand, "Substrate choice impact on microwave sensor," in 2016 *17th International Symposium on Antenna Technology and Applied Electromagnetics (ANTEM)*, Jul. 2016, pp. 1–2.

Miscellaneous Publication List

This section lists the refereed academic papers published during the PhD program but not directly related to the thesis topic.

Journals

1. M. Benlamri, S. Deif, et al., "Planar microwave resonator with electrodeposited ZnO thin film for ultraviolet detection," *Semicond. Sci. Technol.*, vol. 35, no. 2, p. 025003, Feb. 2020.

2. S. Khan, T. R. Jones, S. Deif, and M. Daneshmand, "Developing microfluidically controlled SPDT waveguide switch using 3D printing," *Electron. Lett.*, vol. 53, no. 7, pp. 480–482, Mar. 2017.

Bibliography

[1] S. Timashev and A. Bushinskaya, *Diagnostics and Reliability of Pipeline Systems:* ser. Topics in Safety, Risk, Reliability and Quality. Springer International Publishing, 2016, vol. 30.

[2] Mandke, J. S. s. R. Inst, S. Antonio, and T. X. (US)), "Corrosion causes most pipeline failures in Gulf of Mexico," en, *Oil Gas J.*, vol. 88:44, Oct. 1990.

[3] A. Groysman, "Corrosion Monitoring," en, in *Corrosion for Everybody*, Springer, Dordrecht, 2010, pp. 189–230.

[4] "Corrosion Engineering, Science and Technology: The International Journal of Corrosion Processes and Corrosion Control,"

[5] M. Orazem, *Underground Pipeline Corrosion*, en. Elsevier, Feb. 2014.

[6] J. W. K. Smith and B. R. Hay, "Magnetic flux leakage inspection tool for pipelines," pat. 6 023 986, Feb. 2000.

[7] R. L. Pawson, "Close interval potential surveys: Planning, execution, results," en, NACE International, Houston, TX (United States), Tech. Rep. CONF-970332–, Dec. 1997.

[8] J. M. Pearson, "Electrical examination of coatings on buried pipe lines," *The Petroleum Engineer*, p. 82, 1941.

[9] A. Sabata and S. Brossia, "Remote monitoring of pipelines using wireless sensor network," pat. 7 526 944, May 2009.

[10] Z. Sun, P. Wang, M. C. Vuran, M. A. Al-Rodhaan, A. M. Al-Dhelaan, and I. F. Akyildiz, "MISE-PIPE: Magnetic induction-based wireless sensor networks for underground pipeline monitoring," *Ad Hoc Networks*, vol. 9, no. 3, pp. 218–227, May 2011.

[11] X. Tan and Z. Sun, "An Optimal Leakage Detection Strategy for Underground Pipelines Using Magnetic Induction-Based Sensor Networks," en, in *Wireless Algorithms, Systems, and Applications*, ser. Lecture Notes in Computer Science 7992, Springer Berlin Heidelberg, Aug. 2013, pp. 414–425.

[12] N Gopalsami, D. B. Kanareykin, V Asanov, S Bakhtiari, A. C. Raptis, D. O. Thompson, D. E. Chimenti, C. Nessa, S. Kallsen, and L. Poore, "Microwave Radar Detection of Gas Pipeline Leaks," *AIP Conf. Proc.*, vol. 657, no. 1, pp. 478–484, Mar. 2003.

[13] R. E. Jones, F. Simonetti, M. J. S. Lowe, and I. P. Bradley, "Use of Microwaves for the Detection of Water as a Cause of Corrosion Under Insulation," en, *J. Nondestr. Eval.*, vol. 31, no. 1, pp. 65–76, Mar. 2012.

[14] A. M. Albishi and O. M. Ramahi, "Surface crack detection in metallic materials using sensitive microwave-based sensors," in *2016 IEEE 17th Annual Wireless and Microwave Technology Conference (WAMICON)*, Apr. 2016, pp. 1–3.

[15] C. M. Mann and J. P. DUNNE, "Detection system and method of detecting corrosion under an outer protective layer," pat. US9518918 B2, Dec. 2016.

[16] A Ali, M. E. Badawe, and O. M. Ramahi, "Microwave Imaging of Subsurface Flaws in Coated Metallic Structures Using Complementary Split-Ring Resonators," *IEEE Sens. J.*, vol. 16, no. 18, pp. 6890–6898, 2016.

[17] L. Lawand, O. Shiryayev, K. Al Handawi, N. Vahdati, and P. Rostron, "Corrosivity Sensor for Exposed Pipelines Based on Wireless Energy Transfer," *Sensors (Basel, Switzerland)*, vol. 17, no. 6, May 2017.

[18] M Alamin, G. Y. Tian, A Andrews, and P Jackson, "Corrosion detection using low-frequency RFID technology," *Insight: Non-Destructive Testing & Condition Monitoring*, vol. 54, no. 2, pp. 72–75, Feb. 2012.

[19] Y Hong, P Kannan, B. Z. Harding, H Chen, and others, "Development of a Passive Radio Frequency Identification-Based Sensor for External Crossoion Detection," *Aquat. Microb. Ecol.*, 2016.

[20] C. J. Ziolkowski, "Networked RFID Technology for Monitoring Pipelines," Gas Technology Institute, Tech. Rep. 20915, 2011.

[21] Y. L. He, S McLaughlin, J. S. H. Lo, C Shi, J Lenos, and A Vincelli, "Radio frequency identification (RFID) based corrosion monitoring sensors Part 1 – Component selection and testing," *Corros. Eng. Sci. Technol.*, vol. 50, no. 1, pp. 63–71, Feb. 2015.

[22] N. F. Materer and A. W. Apblett, "Passive wireless corrosion sensor," pat. US7675295 B2, Mar. 2010.

[23] M. Alamin, "Passive low frequencey RFID for detection and monitoring of corrosion under paint and insulation," PhD, Newcastle University, 2014.

[24] D. Patron, W. Mongan, T. P. Kurzweg, A. Fontecchio, G. Dion, E. K. Anday, and K. R. Dandekar, "On the use of knitted antennas and inductively coupled RFID tags for wearable applications," *IEEE transactions on biomedical circuits and systems*, vol. 10, no. 6, pp. 1047–1057, 2016.

[25] R Khalifeh, B Lescop, F Gallée, and S Rioual, "Development of a radio frequency resonator for monitoring water diffusion in organic coatings," *Sens. Actuators A Phys.*, vol. 247, pp. 30–36, Aug. 2016.

[26] L. Dong, L.-F. Wang, and Q.-A. Huang, "An LC passive wireless multifunctional sensor using a relay switch," *IEEE Sensors Journal*, vol. 16, no. 12, pp. 4968–4973, 2016.

[27] R Khalifeh, M. S. Yasri, B Lescop, F Gallée, E Diler, D Thierry, and S Rioual, "Development of Wireless and Passive Corrosion Sensors for Material Degradation Monitoring in Coastal Zones and Immersed Environment," *IEEE J. Oceanic Eng.*, vol. PP, no. 99, pp. 1–7, 2016.

[28] S. Manzari, A. Catini, G. Pomarico, C. Di Natale, and G. Marrocco, "Development of an UHF RFID chemical sensor array for battery-less ambient sensing," *IEEE Sensors Journal*, vol. 14, no. 10, pp. 3616–3623, 2014.

[29] R. W. Revie, *Oil and Gas Pipelines: Integrity and Safety Handbook*, en. John Wiley & Sons, Apr. 2015, Google-Books-ID: DiDPBwAAQBAJ.

[30] M. Betz, C. Bosch, P.-J. Gronsfeld, M. Bagaviev, U. Smit, and R. Grabowski, "Cathodic Disbondment Test: What Are We Testing?," NACE International, Jan. 2012.

[31] O. Griffin, *Pipecoating Part 2: APPLICATION of COATING*.

[32] E. Behdad, "Fusion-Bonded Epoxy's Effects On Cathodic Disbondment," *Pipeline & Gas Journal*, vol. 241, no. 3, Mar. 2014.

[33] A. Jernelöv, "The Threats from Oil Spills: Now, Then, and in the Future," *AMBIO: A Journal of the Human Environment*, vol. 39, no. 5-6, pp. 353–366, Aug. 2010.

[34] H. A. Kishawy and H. A. Gabbar, "Review of pipeline integrity management practices," *Int. J. Pressure Vessels Piping*, vol. 87, no. 7, pp. 373–380, 2010.

[35] F. Varela, M. Y. Tan, and M. Forsyth, "An overview of major methods for inspecting and monitoring external corrosion of on-shore transportation pipelines," *Corros. Eng. Sci. Technol.*, vol. 50, no. 3, pp. 226–235, 2015.

[36] H. R. Vanaei, A. Eslami, and A. Egbewande, "A review on pipeline corrosion, in-line inspection (ILI), and corrosion growth rate models," *International Journal of Pressure Vessels and Piping*, vol. 149, no. Supplement C, pp. 43–54, Jan. 2017.

[37] E Tapanes, "Fibre optic sensing solutions for real-time pipeline integrity monitoring," in *Australian Pipeline Industry Association National Convention*, vol. 3, 2001, pp. 27–30.

[38] L. Wang, Y. H. Wang, X. L. Xiao, H. Yan, G. S. Shi, and Q. R. Wang, "A Fiber-sensor-based Long-distance Safety Monitoring System for buried Oil Pipeline," in *2008 IEEE International Conference on Networking, Sensing and Control*, Apr. 2008, pp. 451–456.

[39] Q. Fu, H. Wan, and F. Qiu, "Pipeline leak detection based on fiber optic early-warning system," *Procedia Engineering*, 2010 Symposium on Security Detection and Information Processing, vol. 7, no. Supplement C, pp. 88–93, Jan. 2010.

[40] R. F. Muscat and A. R. Wilson, "Corrosion Onset Detection Sensor," *IEEE Sensors Journal*, vol. 17, no. 24, pp. 8424–8430, Dec. 2017.

[41] X. P. Qing, S. Beard, S. B. Shen, S. Banerjee, I. Bradley, M. M. Salama, and F.-K. Chang, "Development of a real-time active pipeline integrity detection system," en, *Smart Materials and Structures*, vol. 18, no. 11, p. 115 010, 2009.

[42] R. E. Jones, F Simonetti, M. Lowe, I. Bradley, D. O. Thompson, and D. E. Chimenti, "Use of Microwaves for the Detection of Corrosion Under Insulation," PhD thesis, Imperial College London, 2012.

[43] S Dey, J. K. Saha, and N. C. Karmakar, "Smart Sensing: Chipless RFID Solutions for the Internet of Everything," *IEEE Microwave Mag.*, vol. 16, no. 10, pp. 26–39, Nov. 2015.

[44] R. Singh, E. Singh, and H. Singh Nalwa, "Inkjet printed nanomaterial based flexible radio frequency identification (RFID) tag sensors for the internet of nano things," en, *RSC Advances*, vol. 7, no. 77, pp. 48 597–48 630, 2017.

[45] B. Shao, Q. Chen, Y. Amin, R. Liu, and L.-R. Zheng, "Chipless RFID tags fabricated by fully printing of metallic inks," en, *Ann. Telecommun.*, vol. 68, no. 7-8, pp. 401–413, Jun. 2013.

[46] A. Vena, E. Perret, S. Tedjini, G. E. P. Tourtollet, A. Delattre, F. Garet, and Y. Boutant, "Design of Chipless RFID Tags Printed on Paper by Flexography," *IEEE Transactions on Antennas and Propagation*, vol. 61, no. 12, pp. 5868–5877, Dec. 2013.

[47] R. Nayak, A. Singh, R. Padhye, and L. Wang, "RFID in textile and clothing manufacturing: Technology and challenges," en, *Fashion and Textiles*, vol. 2, no. 1, p. 9, Dec. 2015.

[48] N. C. Karmakar, E. M. Amin, and J. K. Saha, *Chipless RFID Sensors*, en. John Wiley & Sons, Feb. 2016.

[49] B. Shao, Y. Amin, Q. Chen, R. Liu, and L. R. Zheng, "Directly Printed Packaging-Paper-Based Chipless RFID Tag With Coplanar LC Resonator," *IEEE Antennas and Wireless Propagation Letters*, vol. 12, pp. 325–328, 2013.

[50] E. M. Amin, N. C. Karmakar, and B. W. Jensen, "Fully printable chipless RFID multi-parameter sensor," *Sens. Actuators A Phys.*, vol. 248, pp. 223–232, Sep. 2016.

[51] B. Shao, Q. Chen, R. Liu, and L.-R. Zheng, "Design of fully printable and configurable chipless RFID tag on flexible substrate," *Microw. Opt. Technol. Lett.*, vol. 54, no. 1, pp. 226–230, Jan. 2012.

[52] E. M. Amin and N Karmakar, "Development of a chipless RFID temperature sensor using cascaded spiral resonators," in *2011 IEEE SENSORS Proceedings*, ieeexplore.ieee.org, Oct. 2011, pp. 554–557.

[53] A. Vena, L. Sydänheimo, M. Tentzeris, and L. Ukkonen, "A Fully Inkjet-Printed Wireless and Chipless Sensor for CO2 and Temperature Detection," *IEEE Sensors Journal*, vol. 15, no. 1, pp. 89–99, Jan. 2015.

[54] T. Noor, A. Habib, Y. Amin, J. Loo, and H. Tenhunen, "High-density chipless RFID tag for temperature sensing," *Electronics Letters*, vol. 52, no. 8, pp. 620–622, Mar. 2016.

[55] Y. Feng, L. Xie, Q. Chen, and L. R. Zheng, "Low-Cost Printed Chipless RFID Humidity Sensor Tag for Intelligent Packaging," *IEEE Sensors Journal*, vol. 15, no. 6, pp. 3201–3208, Jun. 2015.

[56] A. Habib, R. Asif, M. Fawwad, Y. Amin, J. Loo, and H. Tenhunen, "Directly printable compact chipless RFID tag for humidity sensing," *IEICE Electronics Express*, vol. 14, no. 10, pp. 20 170 169–20 170 169, 2017.

[57] M. Oliveros, M. Carminati, A. Zanutta, T. Mattila, S. Jussila, K. Nummila, A. Bianco, G. Lanzani, and M. Caironi, "Photosensitive chipless radio-frequency tag for low-cost monitoring of light-sensitive goods," *Sensors and Actuators B: Chemical*, vol. 223, no. Supplement C, pp. 839–845, Feb. 2016.

[58] S. Preradovic, I. Balbin, N. C. Karmakar, and G. F. Swiegers, "Multiresonator-based chipless RFID system for low-cost item tracking," *Microwave Theory and Techniques, IEEE Transactions on*, vol. 57, no. 5, pp. 1411–1419, 2009.

[59] B. Shao, "Fully Printed Chipless RFID Tags towards Item-Level Tracking Applications," eng, PhD thesis, 2014.

[60] D. Betancourt, R. Nair, K. Haase, G. Schmidt, M. Bellmann, D. Höft, A. Hübler, and F. Ellinger, "Square-shape fully printed chipless RFID tag and its applications in evacuation procedures," in *2015 9th European Conference on Antennas and Propagation (EuCAP)*, May 2015, pp. 1–5.

[61] L. Yang, R. Zhang, D. Staiculescu, C. P. Wong, and M. M. Tentzeris, "A Novel Conformal RFID-Enabled Module Utilizing Inkjet-Printed Antennas and Carbon Nanotubes for Gas-Detection Applications," *IEEE Antennas and Wireless Propagation Letters*, vol. 8, pp. 653–656, 2009.

[62] J. Liu and B. Li, "A palladium decorated signal walled carbon nanotube enabled chipless sensor for detecting methane at room temperature based on UWB-RFID system," in *2015 IEEE MTT-S International Microwave Workshop Series on Advanced Materials and Processes for RF and THz Applications (IMWS-AMP)*, Jul. 2015, pp. 1–3.

[63] J. Liu and P. B. Li, "Palladium Decorated SWCNTs Sensor for Detecting Methane at Room Temperature Based on UWB-RFID.," *Applied Computational Electromagnetics Society Journal*, vol. 31, no. 8, 2016.

[64] V. Sanchez-Romaguera, M. A. Ziai, D. Oyeka, S. Barbosa, J. S. R. Wheeler, J. C. Batchelor, E. A. Parker, and S. G. Yeates, "Towards inkjet-printed low cost passive UHF RFID skin mounted tattoo paper tags based on silver nanoparticle inks," en, *Journal of Materials Chemistry C*, vol. 1, no. 39, pp. 6395–6402, Sep. 2013.

[65] J. Kim, Z. Wang, and W. S. Kim, "Stretchable RFID for Wireless Strain Sensing With Silver Nano Ink," *IEEE Sensors Journal*, vol. 14, no. 12, pp. 4395–4401, Dec. 2014.

[66] A. Vena, E. Perret, D. Kaddour, and T. Baron, "Toward a Reliable Chipless RFID Humidity Sensor Tag Based on Silicon Nanowires," *IEEE Transactions on Microwave Theory and Techniques*, vol. 64, no. 9, pp. 2977–2985, Sep. 2016.

[67] R. A. R. Antayhua, C. R. Rambo, and F. R. d. Sousa, "Miniaturized Chipless Sensor With Magnetically Coupled Transducer for Improved RCS," *IEEE Microwave and Wireless Components Letters*, vol. 27, no. 8, pp. 718–720, Aug. 2017.

[68] P. A. S. P.E, *Fundamentals of Corrosion: Mechanisms, Causes, and Preventative Methods*, en. CRC Press, Sep. 2009.

[69] F. De Vogelaere, "Corrosion under insulation," en, *Process Safety Progress*, vol. 28, no. 1, pp. 30–35, Mar. 2009.

[70] T. H. Erickson, L. C. Dash, J. J. Murali, and R. Ayers, "Predicting The Progression Of Wetness And Corrosion Under Insulation Damage In Aboveground Pipelines," NACE International, Jan. 2010.

[71] ANSYS. (). ANSYS HFSS: High frequency electromagnetic field simulation software, [Online]. Available: https://www.ansys.com/products/electronics/ansys-hfss (visited on 02/27/2020).

[72] K. G. Ong, J. Wang, R. S. Singh, L. G. Bachas, and C. A. Grimes, "Monitoring of bacteria growth using a wireless, remote query resonant-circuit sensor: Application to environmental sensing," *Biosensors and Bioelectronics*, vol. 16, no. 4–5, pp. 305–312, Jun. 2001.

[73] S. Preradovic and N. C. Karmakar, "Design of fully printable planar chipless RFID transponder with 35-bit data capacity," in *Microwave Conference, 2009. EuMC 2009. European*, IEEE, 2009, pp. 013–016.

[74] Y.-T. Lee, J.-S. Lim, C.-S. Kim, D. Ahn, and S. Nam, "A compact-size microstrip spiral resonator and its application to microwave oscillator," *IEEE Microwave Compon. Lett.*, vol. 12, no. 10, pp. 375–377, Oct. 2002.

[75] J.-S. Hong and M. J. Lancaster, "Couplings of microstrip square open-loop resonators for cross-coupled planar microwave filters," *IEEE Transactions on Microwave Theory and Techniques*, vol. 44, no. 11, pp. 2099–2109, Nov. 1996.

[76] J.-S. G. Hong and M. J. Lancaster, *Microstrip Filters for RF / Microwave Applications*, en. John Wiley & Sons, Apr. 2004.

[77] S. Preradovic and N. C. Karmakar, "Spiral Resonators," en, in *Multiresonator-Based Chipless RFID*, Springer, New York, NY, 2012, pp. 25–51.

[78] D. Psychogiou, R. Gómez-García, and D. Peroulis, "Fully Adaptive Multiband Bandstop Filtering Sections and Their Application to Multifunctional Components," *IEEE Transactions on Microwave Theory and Techniques*, vol. 64, no. 12, pp. 4405–4418, Dec. 2016.

[79] A. Bahadori, *Essentials of Coating, Painting, and Lining for the Oil, Gas and Petrochemical Industries*, en. Gulf Professional Publishing, Jan. 2015.

[80] P. B. Samal, P. J. Soh, and G. A. E. Vandenbosch, "A Systematic Design Procedure for Micro- strip-Based Unidirectional UWB Antennas," *Progress In Electromagnetics Research, Vol.*, vol. 143, pp. 105–130, 2013.

[81] M Goudah and M. Y. M. Yousef, "Bandwidth enhancement techniques comparison for ultra wideband microstrip antennas for wireless application," *Journal of Theoretical and Applied Information Technology*, vol. 35(2), no. 184-193, Jan. 2012.

[82] S. Maci, G. B. Gentili, P. Piazzesi, and C. Salvador, "Dual-band slot-loaded patch antenna," *Antennas and Propagation IEE Proceedings - Microwaves*, vol. 142, no. 3, pp. 225–232, Jun. 1995.

[83] G. Rafi and L. Shafai, "Broadband microstrip patch antenna with V-slot," *Antennas and Propagation IEE Proceedings - Microwaves*, vol. 151, no. 5, pp. 435–440, Oct. 2004.

[84] K. F. Lee, K. M. Luk, K. F. Tong, S. M. Shum, T Huynh, and R. Q. Lee, "Experimental and simulation studies of the coaxially fed U-slot rectangular patch antenna," *IEE Proceedings - Microwaves, Antennas and Propagation*, vol. 144, no. 5, pp. 354–358, Oct. 1997.

[85] W.-S. Yoon, S.-M. Han, S. Pyo, J. W. Baik, and Y. S. Kim, "A polarization switchable microstrip patch antenna with a circular slot," in *2008 Asia-Pacific Microwave Conference*, Dec. 2008, pp. 1–4.

[86] N. B. Toğçuoğlu, Y. Albayrak, M. N. Saylik, M. A. Daye, M. Bal, M. İmecı, and T. İmecı, "Circular patch antenna with circular and rectangular slots," in *2017 25th Signal Processing and Communications Applications Conference (SIU)*, May 2017, pp. 1–4.

[87] S. Deif, S. S. Olokede, M. Nosrati, and M. Daneshmand, "Stepped-impedance slotted microstrip-fed patch antenna for on-metal radio frequency identification applications," en, *Microwave and Optical Technology Letters*, _eprint: https://onlinelibrary.wiley.com/doi/pdf/10.1002/mop.32438.

[88] N. Dimension, *How can RFID tags cost 1 cent?* en-us.

[89] N. Ce and S. Paul, "Thermally Sprayed Aluminum Coatings for the Protection of Subsea Risers and Pipelines Carrying Hot Fluids," en, *Coatings*, vol. 6, no. 4, p. 58, Dec. 2016.

[90] P. Kalansuriya, N. C. Karmakar, and E. Viterbo, "On the Detection of Frequency-Spectra-Based Chipless RFID Using UWB Impulsed Interrogation," *IEEE Transactions on Microwave Theory and Techniques*, vol. 60, no. 12, pp. 4187–4197, Dec. 2012.

[91] S. Preradovic, N. Karmakar, and M. Zenere, "UWB chipless tag RFID reader design," in *2010 IEEE International Conference on RFID-Technology and Applications*, Jun. 2010, pp. 257–262.

[92] A. I. Sunny, G. Y. Tian, J. Zhang, and M. Pal, "Low frequency (LF) RFID sensors and selective transient feature extraction for corrosion characterisation," *Sens. Actuators A Phys.*, vol. 241, pp. 34–43, Apr. 2016.

[93] H. Zhang, R. Yang, Y. He, G. Y. Tian, L. Xu, and R. Wu, "Identification and characterisation of steel corrosion using passive high frequency RFID sensors," *Measurement*, vol. 92, pp. 421–427, Oct. 2016.

[94] J Zhang and G. Y. Tian, "UHF RFID Tag Antenna-Based Sensing for Corrosion Detection #x0026; Characterization Using Principal Component Analysis," *IEEE Trans. Antennas Propag.*, vol. 64, no. 10, pp. 4405–4414, Oct. 2016.

[95] J. Helszajn and D. S. James, "Planar Triangular Resonators with Magnetic Walls," *IEEE Transactions on Microwave Theory and Techniques*, vol. 26, no. 2, pp. 95–100, Feb. 1978.

[96] M. H. Zarifi, S Deif, M Abdolrazzaghi, B Chen, D Ramsawak, M Amyotte, N. V. Sani, Z Hashisho, W Chen, and M Daneshmand, "A Microwave Ring Resonator Sensor for Early Detection of Breaches in Pipeline Coatings," *IEEE Trans. Ind. Electron.*, vol. PP, no. 99, pp. 1–1, 2017.

[97] J Joubert, "Spiral microstrip resonators for narrow-stopband filters," *IEE Proceedings - Microwaves, Antennas and Propagation*, vol. 150, no. 6, pp. 493–496, Dec. 2003.

[98] C. P. Yue and S. S. Wong, "Physical modeling of spiral inductors on silicon," *IEEE Trans. Electron Devices*, vol. 47, no. 3, pp. 560–568, Mar. 2000.

[99] M. Nosrati and M. Daneshmand, "Substrate Integrated Waveguide L-Shaped Iris for Realization of Transmission Zero and Evanescent-Mode Pole," *IEEE Transactions on Microwave Theory and Techniques*, vol. 65, no. 7, pp. 2310–2320, Jul. 2017.

[100] S. S. Bedair, "Characteristics of Some Asymmetrical Coupled Transmission Lines (Short Paper)," *IEEE Transactions on Microwave Theory and Techniques*, vol. 32, no. 1, pp. 108–110, Jan. 1984.

[101] J. D. Baena, R. Marqués, F. Medina, and J. Martel, "Artificial magnetic metamaterial design by using spiral resonators," *Physical Review B*, vol. 69, no. 1, p. 014 402, Jan. 2004.

[102] S Preradovic, N Kamakar, and E. M. Amin, "Chipless RFID tag with integrated resistive and capacitive sensors," in *Asia-Pacific Microw. Conf. 2011*, ieeexplore.ieee.org, Dec. 2011, pp. 1354–1357.

[103] D. G. Archer and P. Wang, "The Dielectric Constant of Water and Debye-Hückel Limiting Law Slopes," *Journal of Physical and Chemical Reference Data*, vol. 19, no. 2, pp. 371–411, Mar. 1990.

[104] Y. J. Yoo, S. Ju, S. Y. Park, Y. J. Kim, J. Bong, T. Lim, K. W. Kim, J. Y. Rhee, and Y. Lee, "Metamaterial Absorber for Electromagnetic Waves in Periodic Water Droplets," en, *Scientific Reports*, vol. 5, p. 14 018, Sep. 2015.

[105] R. Afzalzadeh and R. N. Karekar, "X-band directive single microstrip patch antenna using dielectric parasite," *Electronics Letters*, vol. 28, no. 1, pp. 17–19, Jan. 1992.

[106] S. M. V. Iyer and R. N. Karekar, "Resonance frequency behaviour of microstrip resonators for thin film overlays," *Electronics Letters*, vol. 28, no. 9, pp. 873–875, Apr. 1992.

[107] R. A Yogi, S. A Gangal, R. C Aiyer, and R. N Karekar, "Microwave ring resonator as a novel bio-material moisture sensor," *Sensors and Actuators B: Chemical*, vol. 50, no. 1, pp. 38–44, Jul. 1998.

[108] S. Deif and M. Daneshmand, "Multi-Resonant Chipless RFID Array System for Coating Defect Detection and Corrosion Prediction," *IEEE Transactions on Industrial Electronics*, pp. 1–1, 2019.

[109] A. Ramos, D. Girbau, A. Lazaro, and S. Rima, "IR-UWB radar system and tag design for time-coded chipless RFID," in *2012 6th European Conference on Antennas and Propagation (EUCAP)*, ISSN: 2164-3342, Mar. 2012, pp. 2491–2494.

[110] A. Ramos, D. Girbau, and A. Lazaro, "Influence of materials in time-coded chipless RFID tags characterized using a low-cost UWB reader," in *2012 42nd European Microwave Conference*, Oct. 2012, pp. 526–529.